

AD-A065 923

MECHANICAL TECHNOLOGY INC LATHAM NY RESEARCH AND DEV--ETC F/6 13/9
INVESTIGATION OF MAGNETIC FIELDS AND FORCES ARISING IN CLOSED- --ETC(U)
FEB 79 H S NAGARAJ, J A MCCORMICK
MTI-79TR35

N00014-78-C-0098

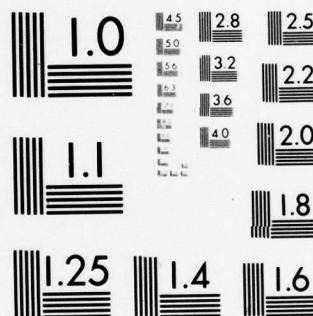
NL

UNCLASSIFIED

1 OF 2

AD
A065923





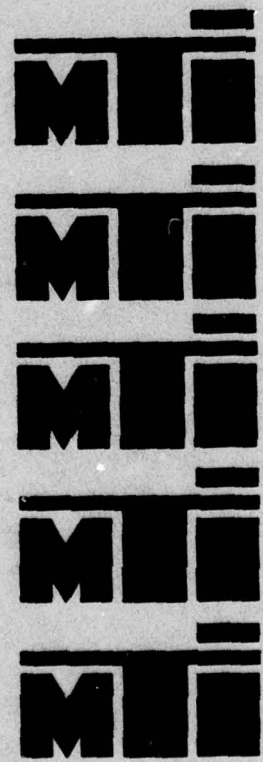
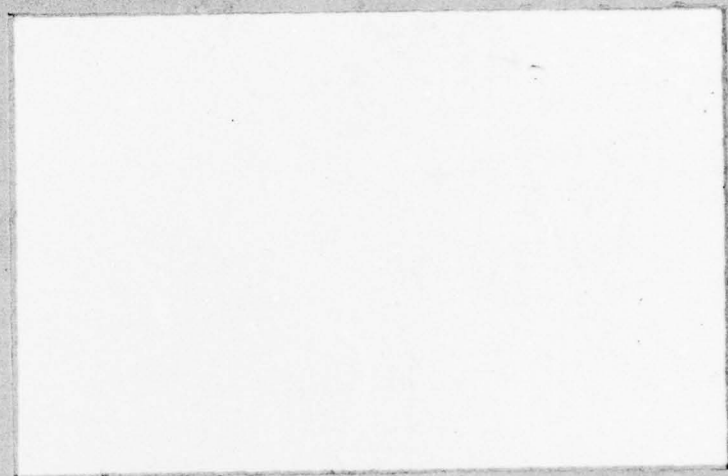
MICROCOPY RESOLUTION TEST CHART
NATIONAL BUREAU OF STANDARDS-1963-A

LEVEL

12

AD A0 65923

DDC FILE COPY

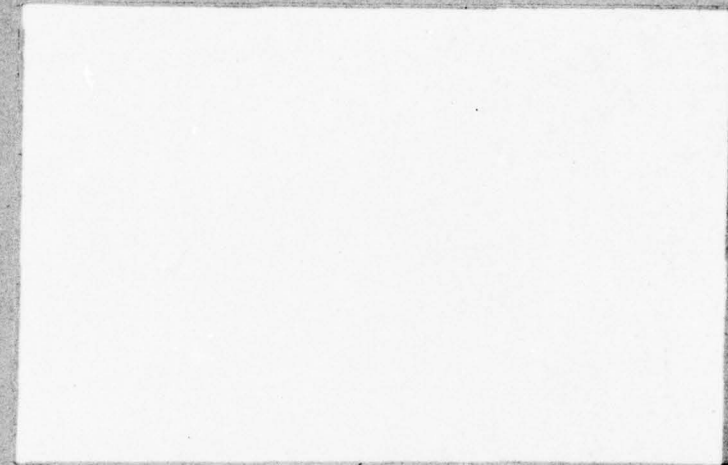


This document has been approved
for public release and sale; its
distribution is unlimited.

Mechanical Technology Incorporated

Research and Development Division

79 03 16 075



Mechanical Technology Incorporated
Research and Development Division
968 Albany-Shaker Road
Latham, New York 12110
(518) 785-2211

DDC FILE COPY

AD A0 65923

LEVEL II

(12)

MTI 79TR35

INVESTIGATION OF MAGNETIC FIELDS AND
FORCES ARISING IN CLOSED- AND OPEN-CIRCUIT-
TYPE MAGNETIC SUSPENSION SYSTEMS

Prepared by:
H.S. Nagaraj
J.A. McCormick
J.A. Walowit

Prepared for:
Office of Naval Research
Arlington, Virginia

February 1979



This document has been approved
for public release and sales in
distribution is unlimited.

MECHANICAL TECHNOLOGY INCORPORATED
968 Albany-Shaker Road
Latham, New York 12110

79 03 16 075

Unclassified

SECURITY CLASSIFICATION OF THIS PAGE (When Data Entered)

REPORT DOCUMENTATION PAGE		READ INSTRUCTIONS BEFORE COMPLETING FORM
1. REPORT NUMBER	2. GOVT ACCESSION NO.	3. RECIPIENT'S CATALOG NUMBER
4. TITLE (and Subtitle) INVESTIGATION OF MAGNETIC FIELDS AND FORCES ARISING IN CLOSED- AND OPEN-CIRCUIT-TYPE MAGNETIC SUSPENSION SYSTEMS.		5. TYPE OF REPORT & PERIOD COVERED Final Technical Report.
7. AUTHOR(s) H.S./Nagaraj J.A./McCormick J.A./Walowit		6. PERFORMING ORG. REPORT NUMBER 79TR35
9. PERFORMING ORGANIZATION NAME AND ADDRESS MECHANICAL TECHNOLOGY INCORPORATED 968 Albany-Shaker Road Latham, New York 12110		8. CONTRACT OR GRANT NUMBER(s) NO 14-78-C-0098
11. CONTROLLING OFFICE NAME AND ADDRESS Office of Naval Research Arlington, Virginia		10. PROGRAM ELEMENT, PROJECT, TASK AREA & WORK UNIT NUMBERS
14. MONITORING AGENCY NAME & ADDRESS (if different from Controlling Office) MTI-79TR35		12. REPORT DATE February 1979
		13. NUMBER OF PAGES 147
		15. SECURITY CLASS. (of this Report) Unclassified
		15a. DECLASSIFICATION/DOWNGRADING SCHEDULE
16. DISTRIBUTION STATEMENT (of this Report) This document has been approved for public release: its distribution is unlimited.		
17. DISTRIBUTION STATEMENT (of the abstract entered in Block 20, if different from Report)		
18. SUPPLEMENTARY NOTES		
19. KEY WORDS (Continue on reverse side if necessary and identify by block number) Magnetic Bearing Open and Closed Magnetic Circuits Electromagnetic Field Theory High-Permeability Material Permanent Magnet		
20. ABSTRACT (Continue on reverse side if necessary and identify by block number) Magnetic bearings can employ either closed- or open-type magnetic circuits. A theory that was developed, under sponsorship of the Office of Naval Research (ONR), for predicting forces and fluxes in closed-circuit-type magnetic systems employing high-permeability material was reported earlier. This theory had only been validated through measurements under static conditions. In this work, several aspects of both closed- and open-circuit-type magnetic systems have been studied. → next page		

DD FORM 1 JAN 73 1473

EDITION OF 1 NOV 65 IS OBSOLETE

Unclassified

SECURITY CLASSIFICATION OF THIS PAGE (When Data Entered)

411 037

JOB

NO. MTI 79TR35
DATE: February 1979

TECHNICAL REPORT

INVESTIGATION OF MAGNETIC FIELDS AND FORCES
ARISING IN CLOSED- AND OPEN-CIRCUIT-TYPE
MAGNETIC SUSPENSION SYSTEMS

H.S. Nagaraj, J.A. McCormick, J.A. Walowit
Author (s) H.S. Nagaraj, J.A. McCormick, J.A. Walowit
W. Shapiro
Approved W. Shapiro, Manager, Advanced Technology Dept.

Prepared for
Office of Naval Research
Arlington, Virginia

Prepared under
Contract N00014-78-C-0098



MECHANICAL TECHNOLOGY INCORPORATED

968 ALBANY - SHAKER ROAD -- LATHAM, NEW YORK -- PHONE 785-0922

TABLE OF CONTENTS

<u>Section</u>		<u>Page</u>
	LIST OF FIGURES	iv
	NOMENCLATURE.	vii
	ACKNOWLEDGMENTS	xi
1.0	INTRODUCTION.	1-1
2.0	ANALYTICAL RESULTS FOR CLOSED MAGNETIC CIRCUIT WITH HIGH-PERMEABILITY MATERIAL.	2-1
	2.1 Description of Magnetic Quantities	2-1
	2.2 Results for Straight-Tooth Configuration and Discussion	2-4
	2.3 Results for Circular-Tooth Configuration and Discussion	2-7
3.0	DYNAMIC MEASUREMENTS FOR CLOSED MAGNETIC CIRCUIT WITH HIGH-PERMEABILITY MATERIAL.	3-1
	3.1 Experimental Apparatus	3-1
	3.1.1 Magnetic Circuit.	3-1
	3.1.2 Test Rig.	3-4
	3.1.3 Measuring System.	3-10
	3.2 Static Measurements.	3-13
	3.3 Flux and Transverse Force Measurements Under Dynamic Conditions	3-13
	3.3.1 Instrumentation for Wave-Form Analysis.	3-14
	3.3.2 Dynamic Rig Checkout.	3-16
	3.3.3 Experimental Procedure.	3-17
	3.3.4 Experimental Results and Discussion	3-18
4.0	ANALYSIS OF PERMANENT MAGNETS IN REPULSION.	4-1
	4.1 Analysis Procedure	4-3
	4.2 Analysis for Rectangular Parallelopiped-Shaped Magnets.	4-4
	4.3 Analysis for Cylinder-Shaped Magnets	4-10
	4.4 Results and Discussion for Rectangular Parallelopiped-Shaped Magnets.	4-13
	4.5 Results and Discussion for Cylinder-Shaped Magnets	4-34

TABLE OF CONTENTS (continued)

<u>Section</u>		<u>Page</u>
5.0	EXPERIMENTS WITH PERMANENT MAGNETS IN REPULSION	5-1
5.1	Experimental Apparatus	5-1
5.1.1	Magnet Material	5-1
5.1.2	Test Rig.	5-1
5.1.3	Force Measurement	5-6
5.2	Results and Discussion	5-6
5.2.1	Z-Force Versus Gap.	5-6
5.2.2	X-Force Versus Displacement	5-10
5.2.3	Z-Force Versus Displacement	5-10
5.2.4	Comparison with Theoretical Predictions . . .	5-10
6.0	PERMANENT MAGNETS IN CLOSED MAGNETIC CIRCUIT.	6-1
6.1	Magnetic Circuit	6-1
6.2	Experimental Apparatus and Procedure	6-3
6.2.1	Materials	6-3
6.2.2	Test Rig.	6-3
6.2.3	Force Measurement	6-6
6.2.4	Flux Measurement.	6-6
6.2.5	Experimental Procedure.	6-8
6.3	Results and Discussion	6-8
6.3.1	One Magnet in the Circuit	6-8
6.3.2	Two Magnets in the Circuit.	6-11
6.3.3	Comparison with Theoretical Predictions . . .	6-17
7.0	CONCLUSIONS	7-1
8.0	REFERENCES.	8-1

LIST OF FIGURES

<u>Number</u>		<u>Page</u>
2-1	Schematic of Tooth Geometry Used in Analysis.	2-2
2-2	Semi-Infinite Tooth Width Approximation for Misaligned Teeth	2-3
2-3	Air-Gap Permeance Variation with Gap Thickness ($\bar{e} = 0.$, $t/h > 1$)	2-5
2-4	Normal Force Variation with Gap Thickness ($\bar{e} = 0.$, $t/h > 1$)	2-6
2-5	Decrease in Air-Gap Permeance (from Misaligned Position) with Transverse Displacement - Straight Teeth	2-8
2-6	Decrease in Normal Force (from Aligned Position) with Transverse Displacement - Straight Teeth.	2-9
2-7	Transverse Force Versus Transverse Displacement - Straight Teeth.	2-10
2-8	Decrease in Air-Gap Permeance (from Aligned Position) with Transverse Displacement - Circular Teeth	2-12
2-9	Decrease in Normal Force (from Aligned Position) with Transverse Displacement - Circular Teeth.	2-13
2-10	Transverse Force Versus Transverse Displacement - Circular Teeth.	2-14
3-1	Magnetic Test Assembly.	3-2
3-2	Wiring Diagram for Magnetizing Coils.	3-3
3-3	Photograph of Core and Tooth Geometry	3-5
3-4	Schematic of Test Apparatus	3-6
3-5	Front View of Apparatus	3-7
3-6	Photograph of Magnetic Cores in Test Apparatus.	3-8
3-7	Lower Core Piece Drive and Position Sensing Arrangement .	3-9
3-8	Ling Model B335 Electrodynamic Shaker Facility at MTI-Latham.	3-11
3-9	Schematic of Tracking Analyzer Setup for Dynamic Force Measurement	3-15
3-10	Measured Tangential Force Amplitudes at 90-Kilolines Flux; .005-, .015-, .020-Inch Gaps.	3-19
3-11	Measured Tangential Force Amplitudes at 135-Kilolines Flux; .010-, .015-, .020-Inch Gaps.	3-20
3-12	Sample Tangential Force Wave Forms at 135-Kilolines Flux, .010-in. Gap, 30-Hz Frequency	3-21
4-1	Two Rectangular Parallelopiped-Shaped Magnets in Repulsive Mode.	4-5

LIST OF FIGURES (continued)

<u>Number</u>		<u>Page</u>
4-2	Two Cylinder-Shaped Magnets in Repulsive Mode	4-11
4-3	Z-Force Versus E (T = 1.0, L = 0.2)	4-15
4-4	Z-Force Versus E (T = 1.0, L = 0.5)	4-16
4-5	Z-Force Versus E (T = 1.0, L = 1.0)	4-17
4-6	Z-Force Versus E (T = 5.0, L = 0.2)	4-18
4-7	Z-Force Versus E (T = 5.0, L = 0.5)	4-19
4-8	Z-Force Versus E (T = 5.0, L = 1.0)	4-20
4-9	X-Force Versus E (T = 1.0, L = 0.2)	4-22
4-10	X-Force Versus E (T = 1.0, L = 0.5)	4-23
4-11	X-Force Versus E (T = 1.0, L = 1.0)	4-24
4-12	X-Force Versus E (T = 5.0, L = 0.2)	4-25
4-13	X-Force Versus E (T = 5.0, L = 0.5)	4-26
4-14	X-Force Versus E (T = 5.0, L = 1.0)	4-27
4-15	Z-Force Versus EG (T = 1.0, L = 0.2).	4-28
4-16	Z-Force Versus EG (T = 1.0, L = 0.5).	4-29
4-17	Z-Force Versus EG (T = 1.0, L = 1.0).	4-30
4-18	Z-Force Versus EG (T = 5.0, L = 0.2).	4-31
4-19	Z-Force Versus EG (T = 5.0, L = 0.5).	4-32
4-20	Z-Force Versus EG (T = 5.0, L = 1.0).	4-33
4-21	X-Force Versus EG (T = 1.0, L = 0.2).	4-35
4-22	X-Force Versus EG (T = 1.0, L = 0.5).	4-36
4-23	X-Force Versus EG (T = 1.0, L = 1.0).	4-37
4-24	X-Force Versus EG (T = 5.0, L = 0.2).	4-38
4-25	X-Force Versus EG (T = 5.0, L = 0.5).	4-39
4-26	X-Force Versus EG (T = 5.0, L = 1.0).	4-40
4-27	Z-Force Versus E (L = 0.2).	4-41
4-28	Z-Force Versus E (L = 0.5).	4-42
4-29	Z-Force Versus E (L = 1.0).	4-43
4-30	X-Force Versus E (L = 0.2).	4-44
4-31	X-Force Versus E (L = 0.5).	4-46
4-32	X-Force Versus E (L = 1.0).	4-47
4-33	Z-Force Versus EG (L = 0.2)	4-48
4-34	Z-Force Versus EG (L = 0.5)	4-49

LIST OF FIGURES (continued)

<u>Number</u>		<u>Page</u>
4-35	Z-Force Versus EG (L = 1.0)	4-50
4-36	X-Force Versus EG (L = 0.2)	4-51
4-37	X-Force Versus EG (L = 0.5)	4-52
4-38	X-Force Versus EG (L = 1.0)	4-53
5-1	Test Apparatus.	5-3
5-2	Permanent Magnet in the Aluminum Holder	5-4
5-3	Arrangement of Magnets Used in Experiments.	5-5
5-4	Test Setup.	5-7
5-5	Z-Force Versus Gap (e = 0).	5-8
5-6	Z-Force Versus Gap.	5-9
5-7	X-Force Versus Displacement	5-11
5-8	Z-Force Versus Displacement	5-12
5-9	Z-Force Versus Gap (T = 1.0625, L = 0.2469)	5-13
5-10	X-Force Versus Displacement (T = 1.0625, L = 0.2469). . .	5-14
5-11	Z-Force Versus Displacement (T = 1.0625, L = 0.2469). . .	5-15
6-1	Magnetic Circuit with Permanent Magnets and High- Permeability Pole Pieces.	6-2
6-2	Core Piece with Permanent Magnet Installed.	6-4
6-3	Magnetic Cores Used with Permanent Magnets in Closed- Circuit Suspension Experiments.	6-5
6-4	Test Rig with Core Pieces Installed	6-7
6-5	Flux Versus Gap - One Magnet.	6-9
6-6	Z-Force Versus Gap - One Magnet	6-10
6-7	Flux Versus Displacement.	6-12
6-8	X-Force Versus Displacement - One Magnet.	6-13
6-9	Flux Versus Gap - Two Magnets	6-14
6-10	Z-Force Versus Gap - Two Magnets.	6-15
6-11	X-Force Versus Displacement - Two Magnets	6-16
6-12	X-Force Versus Displacement - Comparison with Theory (Gap = .005 Inch)	6-19
6-13	X-Force Versus Displacement - Comparison with Theory (Gap = .010 Inch)	6-20
6-14	X-Force Versus Displacement - Comparison with Theory (Gap = .015 Inch)	6-21
6-15	X-Force Versus Displacement - Comparison with Theory (Gap = .020 Inch)	6-22

NOMENCLATURE

A	= Appears in the expression for f
\bar{A}	= Vector magnetic potential ($\nabla \times \bar{A} = \bar{B}$)
\bar{A}_M	= Vector magnetic potential for \bar{M}
B	= Flux density, Wb/m ²
\bar{B}	= Flux density vector
D	= Diameter of circular tooth, m (in.)
e	= Transverse displacement, m (in.)
\bar{e}	= $\frac{e}{h}$
E	= $\frac{e}{W}, \frac{e}{R}$
EG	= $\frac{g}{W}, \frac{g}{R}$
E_D	= Energy dissipated per cycle, J
\bar{F}	= Force vector, N
\hat{F}	= $\frac{2h F_{in}}{\mu_o (\Delta F)^2 \ell}$
$\Delta \hat{F}$	= Decrease in the nondimensional force from aligned position for straight tooth
f	= Integrand in force integrals
ΔF	= Magnetomotive force, AT
F_{in}	= Normal force per tooth, N
F_{it}	= Transverse force per tooth, N
F_o	= Amplitude of the first harmonic of the force wave form, N
\hat{F}_t	= $\frac{2h F_{it}}{\mu_o (\Delta F)^2 \ell}$

NOMENCLATURE (CONT'D)

$$\hat{F}_{tR} = \frac{2h F_{it}}{\mu_0 (\Delta F)^2 \pi D}$$

$\Delta \hat{F}_R$ = Decrease in the nondimensional force from aligned position for circular tooth

F_x, F_y, F_z = Force components, N

g = Gap thickness between permanent magnets, m

h = Gap thickness, m (in.)

H = Field strength, AT/m

\bar{i} = Current density vector

I, I' = Currents in the circuits, A

$$I_x = \frac{F_x}{\frac{\mu_0}{4\pi} KK' W^2} \text{ or } \frac{F_x}{\frac{\mu_0}{4\pi} KK' R^2}$$

$$I_z = \frac{F_z}{\frac{\mu_0}{4\pi} KK' W^2} \text{ or } \frac{F_z}{\frac{\mu_0}{4\pi} KK' R^2}$$

\bar{J} = Volume current density vector, A/m²

\bar{K} = Surface current density vector, A/m

K, K' = Surface current densities of two magnets, A/m

ℓ = Tooth length, m (in.)

ℓ^* = Magnet length, m

$$L = \frac{\ell}{W} \frac{\ell}{R}$$

M = Magnetic moment or magnetization, Wb/m²

\bar{M} = Magnetization vector

\bar{n} = Unit vector normal to S

P, P^* = Appears in the expression for f

NOMENCLATURE (CONT'D)

p_i	$= \frac{\phi_i}{\Delta F}$, Air-gap permeance per tooth, $\frac{Wb}{AT}$
Q	= Appears in the expression for f
r	= Magnitude of the radius vector, m
\bar{r}	= Radius vector
R	= Magnet radius, m
s	= Gap between teeth, m (in.)
S	= Surface
t	= Tooth width, m (in.)
t^*	= Magnet thickness, m
T	$= \frac{t}{W}$
V	= Volume
W	= Magnet width, m
x, y, z x', y', z'	$\left. \begin{array}{l} \\ \end{array} \right\} = \text{Coordinates used in permanent magnet analysis}$
\hat{x}	$= \frac{\phi + \phi'}{4}$
\hat{y}	$= \frac{\phi - \phi'}{4}$
α	= Phase angle between the sinusoidal displacement and the first harmonic of the force wave form
δ	= Amplitude of oscillation of the lower core piece, m
ξ	$= z' - z$
η	$= z' + z$
μ	= permeability, $\frac{(Wb/m^2)}{(AT/m)}$
μ_o	= Permeability of free space $= 4\pi \cdot 10^{-7} \frac{(Wb/m^2)}{(A/m)}$

NOMENCLATURE (CONT'D)

μ_V	= Permeability inside V, $\frac{(\text{Wb/m}^2)}{(\text{A/m})}$
ϕ, ϕ'	= Angular positions of current elements
ϕ_i	= Flux per tooth, Wb
$\hat{\phi}$	= $\frac{\phi_i}{2\mu_0(\Delta F)\ell}$
$\Delta\hat{\phi}$	= Decrease in the nondimensional flux from aligned position for straight tooth
$\Delta\hat{\phi}_R$	= Decrease in the nondimensional flux from aligned position for circular tooth
∇	= Gradient operator

Subscripts

i	= ith tooth
n	= normal or axial
t	= transverse
R	= round or circular
r	= remnant values
x, y, z z', y', z' }	= coordinate axes on the two magnets
1, 2, 3, 4 1', 2', 3', 4' }	= represent different faces of the two magnets

ACKNOWLEDGMENTS

The authors are very grateful to Mr. M. Keith Ellingsworth, project manager, Office of Naval Research, for his continued support and encouragement.

The authors wish to acknowledge Mr. Dave Ladue and Mr. John Esek for assistance in running the experiments, and Miss Tenley James for running the computer programs.

1.0 INTRODUCTION

The concept of magnetic bearings basically consists of using magnetic forces to maintain controlled separation between bearing surfaces. The magnetic bearings offer a number of advantages over conventional bearings:

- They require no lubricants and, therefore, can operate in vacuum and be free from contamination;
- They have low mechanical friction and therefore energy can be saved;
- The start-stop rub is absent;
- The bearing stiffness can be controlled by electrical means, thus helping to step through critical speeds.

The magnetic bearings can employ either closed- or open-type magnetic circuits. An example of the latter case is two magnets in repulsion. In this case, the repelling force increases as the two magnets are brought closer, indicating stability. However, at the same time, it is difficult to keep the magnets aligned because any small transverse displacement creates a transverse force which tends to push the magnets further apart. The system is thus unstable in the transverse direction. The stable and unstable directions are also referred to as passive and active directions, respectively. The closed-circuit system, exemplified by two attracting magnets, is active in the normal direction and passive in the transverse direction.

Magnetic bearings are thus not inherently stable in all the three directions, and this has been shown to be true mathematically (Earnshaw's Theorem, [1]*). For successful operation, therefore, the active directions have to be servoed. Using the method of electrical servoing, many active magnetic suspensions have been built [2, 3]. However, maintaining passive forces as much as possible decreases the need to depend on electrical servoing and thereby reduces the electrical power requirements and propensity for instability.

Techniques to predict magnetic forces in both open- and closed-circuit systems have not yet been fully developed. However, over the past several years

*Numbers in brackets indicate references in Section 8.0 of this report.

a considerable amount of research on magnetic suspensions has been performed at Mechanical Technology Incorporated (MTI). The continued sponsorship by the Office of Naval Research (ONR) has resulted in the development of a validated theory for predicting forces and fluxes in a closed-circuit system employing high-permeability ferromagnetic materials. This work has been described in an earlier report [4]. The present report contains a description of all the research performed for ONR on magnetic bearings subsequent to that reported in Reference 4.

The research described in this report contains the results of studies performed on both closed- and open-circuit magnetic suspensions. The closed-circuit system was the same as that investigated earlier [4]. The studies performed on closed-circuit suspension consisted of the production of analytical curves for the prediction of forces and fluxes and further experimental verification of the theory when permanent magnets are used to energize the magnetic circuit. The work on open-circuit suspensions consisted of the development of a theory together with experimental verification for predicting forces in a quasi-static environment. These are described in more detail below.

The theory for predicting forces in closed-circuit systems [4] was used to produce curves for nondimensional values of normal and transverse forces. The variables were gap thickness and eccentricity, and the parameter considered was related to tooth geometry. Results have been reported for both straight- and circular-tooth configurations.

Dynamic measurements were performed on the same closed magnetic circuit used previously in order to determine any possible effects of transverse vibration. Although the measurements indicated some degradation of the transverse forces at moderately high frequencies of vibration, the phase-angle measurement between force and displacement indicated an extremely small value of damping in the system.

Towards the study of open-circuit suspensions, a theory was developed to predict both normal and transverse forces between two repelling permanent magnets, together with its experimental verification. For purposes of analysis, the magnets were mathematically modeled by current densities, and forces were

calculated using the Ampere's Law. A modified version of the test apparatus used for dynamic measurements was utilized for experimental measurements.

Also, the theory that was developed for closed-circuit systems employing high-permeability materials was verified for the case when permanent magnets are used as a battery to energize the magnetic circuit. The rare-earth-cobalt permanent magnets were used in the experimental measurements.

2.0 ANALYTICAL RESULTS FOR CLOSED MAGNETIC CIRCUIT WITH HIGH-PERMEABILITY MATERIAL

A validated theory for predicting fluxes and forces in a suspension system based on closed magnetic circuits employing high-permeability materials was reported in Reference 4. The emphasis in Reference 4 was the experimental validation of the theory and a subsequent optimization of the bearing surface geometry (tooth geometry) to obtain a maximum stabilizing transverse force.

The purpose here is to present some analytical results that were obtained using the above theory for two different tooth configurations: straight tooth and circular tooth. The results for these two cases will be presented in two separate sections after a brief description of the magnetic quantities used. The results include plots of nondimensional values of flux and normal and transverse forces as functions of either gap or displacement, with tooth geometry (gap \div tooth spacing) as the parameter.

2.1 Description of Magnetic Quantities

A schematic of the geometry of the teeth on the two bearing surfaces used in the analysis is shown in Figure 2-1. It has been shown previously [4] that, for most practical situations, the semi-infinite tooth-width approximation shown in Figure 2-2 is adequate for the calculation of the fringing magnetic field around the edge of the teeth and the normal and transverse forces.

The limitation of the above analysis, however, is that the transverse displacement in relation to the tooth width and the air-gap thickness cannot exceed a certain value ($\frac{t-e}{h} > 5$) for validity. This, however, was found not to restrict too severely the applicability of the theory for practical bearing calculations.

The actual theory and the necessary analytical treatment for the computation of fluxes and forces has been described in detail in Reference 4. Only the different parameters and variables used in the presentation of the results are described here.

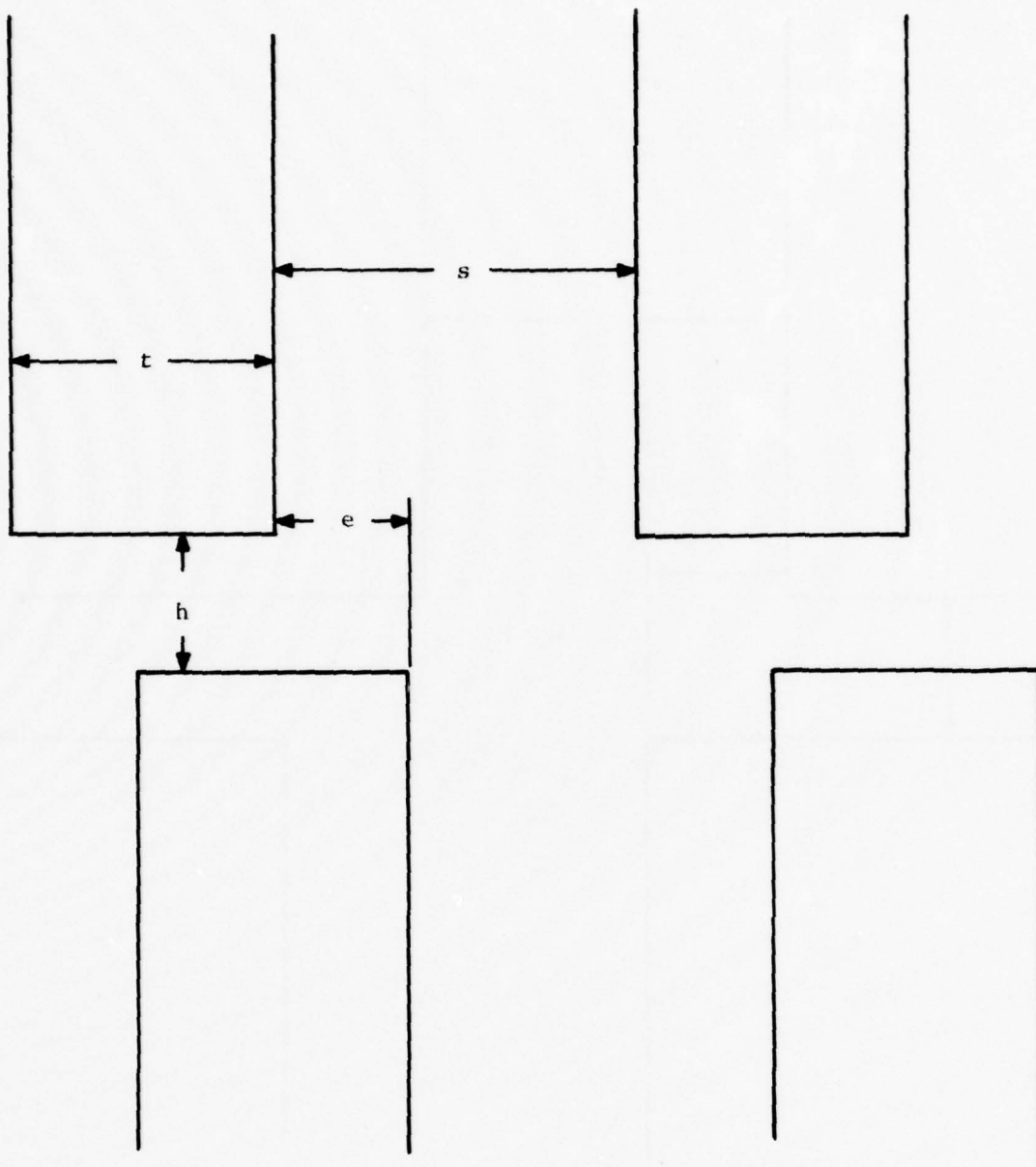


Fig. 2-1 Schematic of Tooth Geometry Used in Analysis

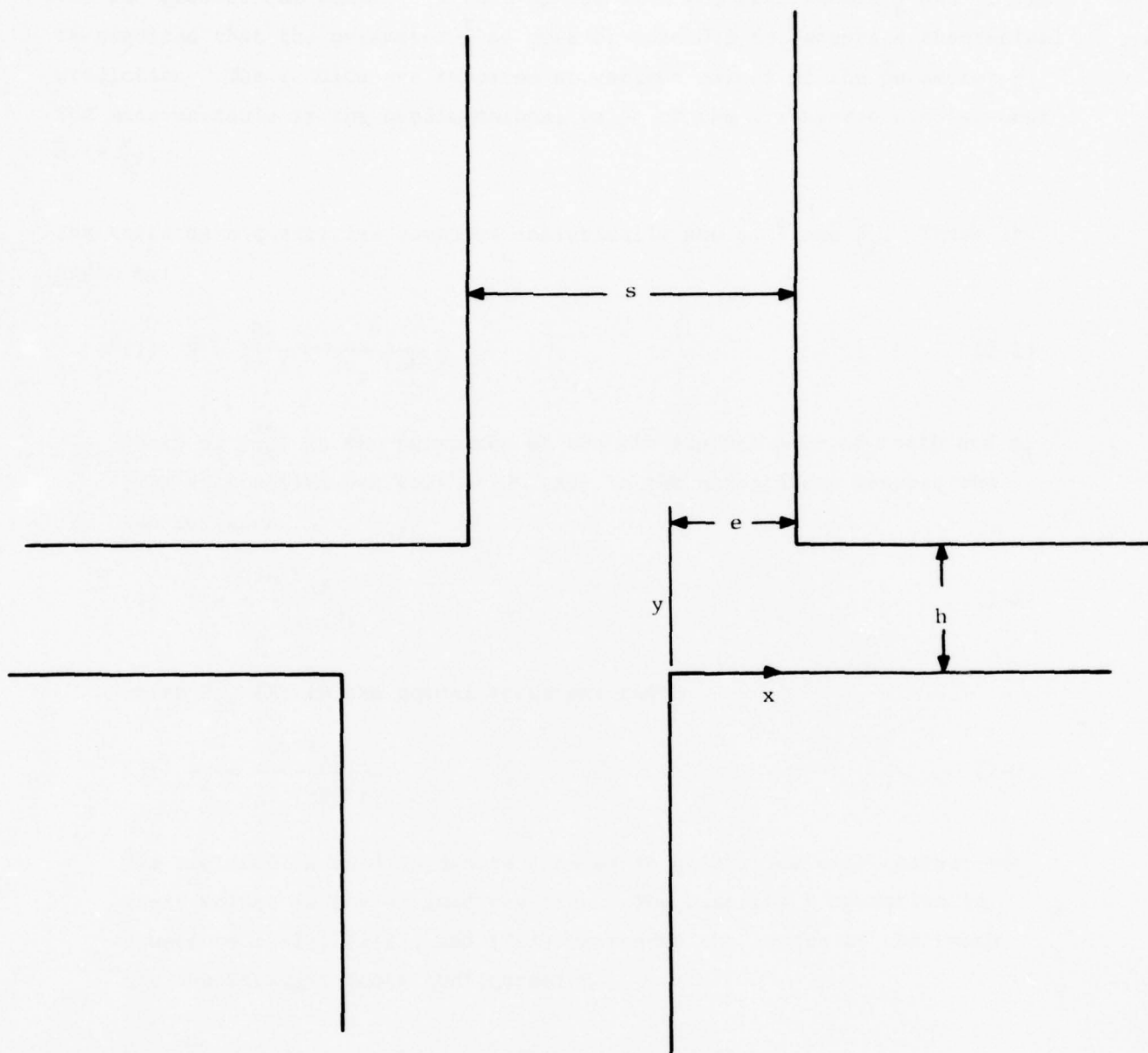


Fig. 2-2 Semi-Infinite Tooth Width Approximation for Misaligned Teeth

The two geometrical parameters that appear with the results are $\frac{t}{h}$ and $\frac{h}{s}$. It is required that the parameter $\frac{t}{h}$ be greater than 0.5 for accurate theoretical prediction. The results are reported at various values of the parameter $\frac{h}{s}$. The main variable is the nondimensional value of the transverse displacement \bar{e} ($= \frac{e}{h}$).

The three main quantities computed analytically are $\hat{\phi}$, \hat{F} and \hat{F}_t . These are given by:

$$(1) \quad \hat{\phi} = \frac{p_i}{2\mu_o \ell} = \frac{\phi_i}{2\mu_o (\Delta F) \ell} \quad (2-1)$$

where $p_i \left(\frac{Wb}{AT} \right)$ is the permeance of the air-gap per pair of teeth and ϕ_i (Wb) is the flux per tooth. ΔF (AT) is the mmf present between the two surfaces.

$$(2) \quad \hat{F} = \frac{2h F_{if}}{\mu_o (\Delta F)^2 \ell} \quad (2-2)$$

where F_{if} (N) is the normal force per tooth.

$$(3) \quad \hat{F}_t = \frac{2h F_{it}}{\mu_o (\Delta F)^2 \ell} \quad (2-3)$$

The prefix Δ is used to denote changes in quantities with respect to their values in the aligned position. The quantity ℓ appearing in Equations (2-1), (2-2), and (2-3) represent the length of the teeth for the straight-tooth configuration.

2.2 Results for Straight-Tooth Configuration and Discussion

Figure 2-3 represents the variation of air-gap permeance with gap thickness for the aligned position of the teeth. If the flux for a given case is known, the above curve can be used to determine the corresponding mmf acting across the air gap. The variation of normal force with gap is represented in Figure 2-4 for the aligned-tooth configuration. It is to be noted that the shape of the curve in the above figure is as shown because the ordinate contains the parameter $\frac{t}{h}$.

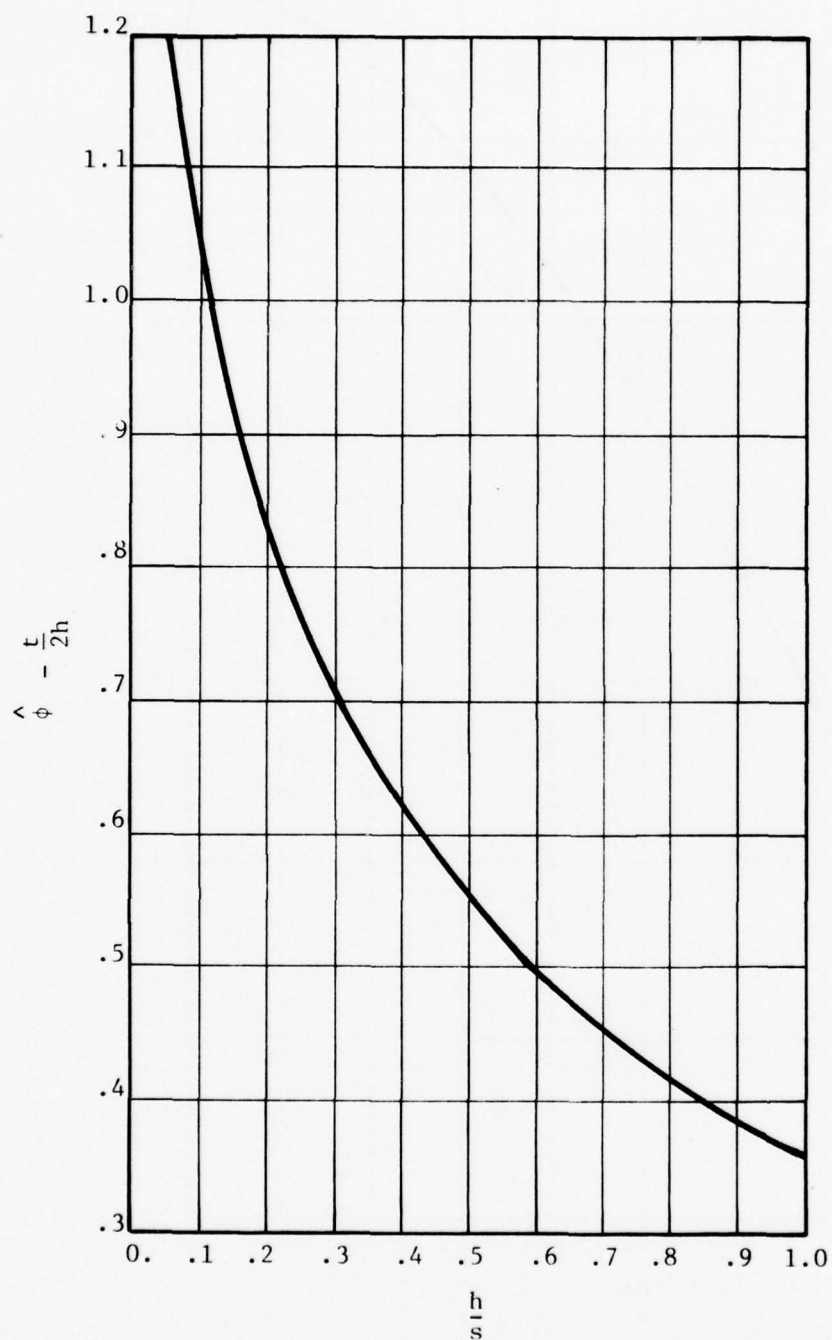


Fig. 2-3 Air-Gap Permeance Variation
with Gap Thickness
($\bar{e} = 0., \frac{t}{h} > 1$)

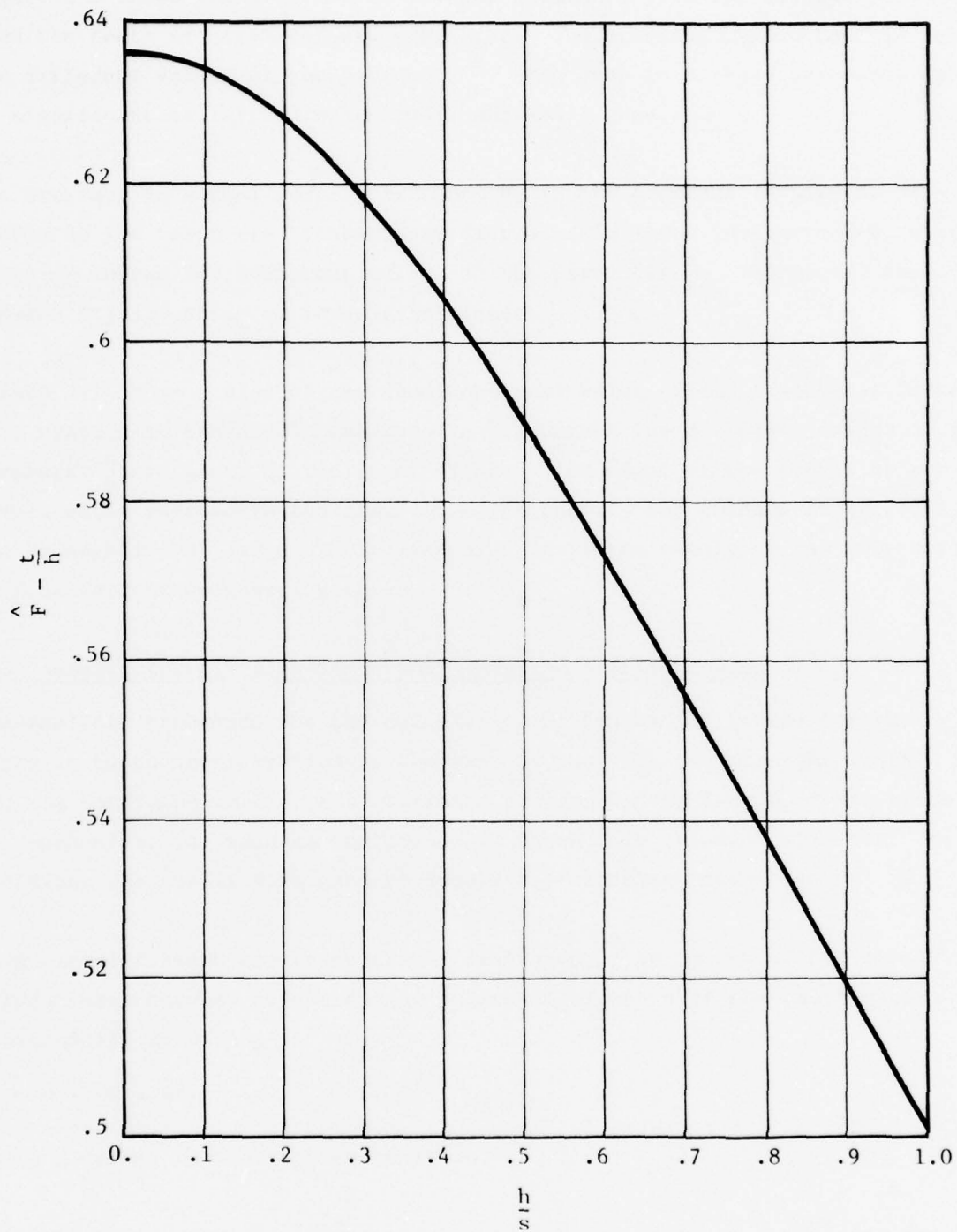


Fig. 2-4 Normal Force Variation With Gap Thickness
 $(\bar{e} = 0., \frac{t}{h} > 1)$

Figure 2-5 shows the decrease in air-gap permeance from the aligned position when the teeth are transversely displaced. The previous figures contain curves for different values of the parameter $\frac{h}{s}$. The drop in air-gap permeance can be significant at large displacements and small gaps.

The decrease in normal force corresponding to the decrease in air-gap permeance as the teeth are transversely displaced is shown in Figure 2-6, which contains curves for different values of the parameter $\frac{h}{s}$. The normal force reduces significantly at large displacement.

Figure 2-7 shows a plot of the nondimensional value of the transverse force with respect to the displacement ratio $\frac{e}{h}$. Curves for different values of the parameter $\frac{h}{s}$ are given in the above figure. The slope of the curves at any displacement represents the transverse stiffness. The transverse stiffness can be negative at large displacements; this is the result of the interaction of flux for the neighboring teeth.

2.3 Results for Circular-Tooth Configuration and Discussion

The analysis procedure for the calculation of fluxes and forces for the circular-tooth configuration is the same as that for the straight tooth. In all the nondimensional groups mentioned previously the length of the teeth ℓ is replaced by the mean circumference πD where D is the mean diameter. In addition, the suffix R is used to denote the circular-tooth case.

When circular teeth are transversely displaced by an amount e , the actual displacement between corresponding segmental elements of the teeth varies sinusoidally according to

$$e' = e \sin\theta,$$

where θ refers to the angular position.

In order to compute the fluxes and forces for the circular teeth, the results for misaligned, segmental elements (approximated by straight configuration) are integrated around the mean circumference. The results presented in this section are the integrated values. For the circular tooth, the decrease in

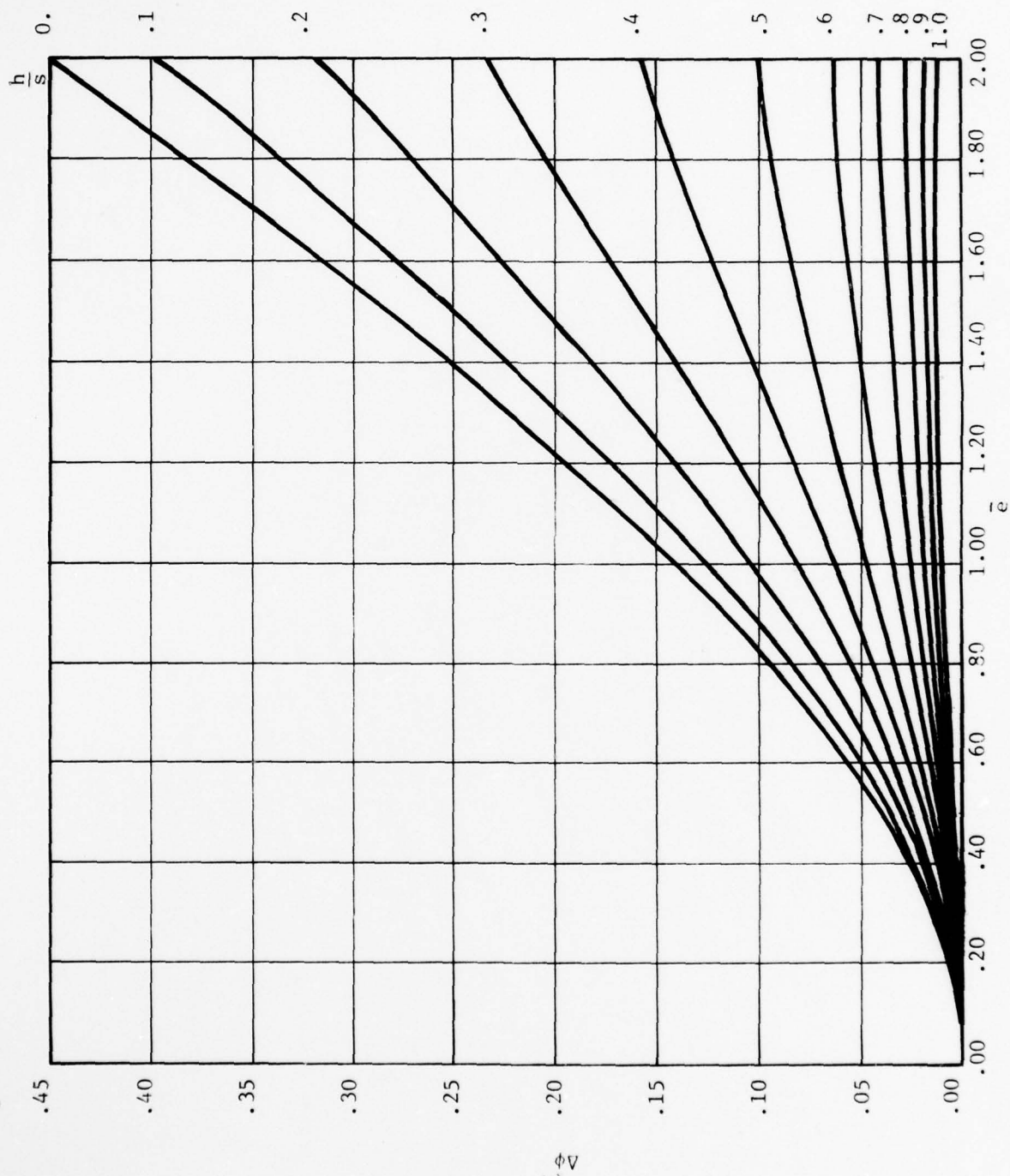


Fig. 2-5 Decrease in Air-Gap Permeance (from aligned position) with Transverse Displacement - Straight Teeth

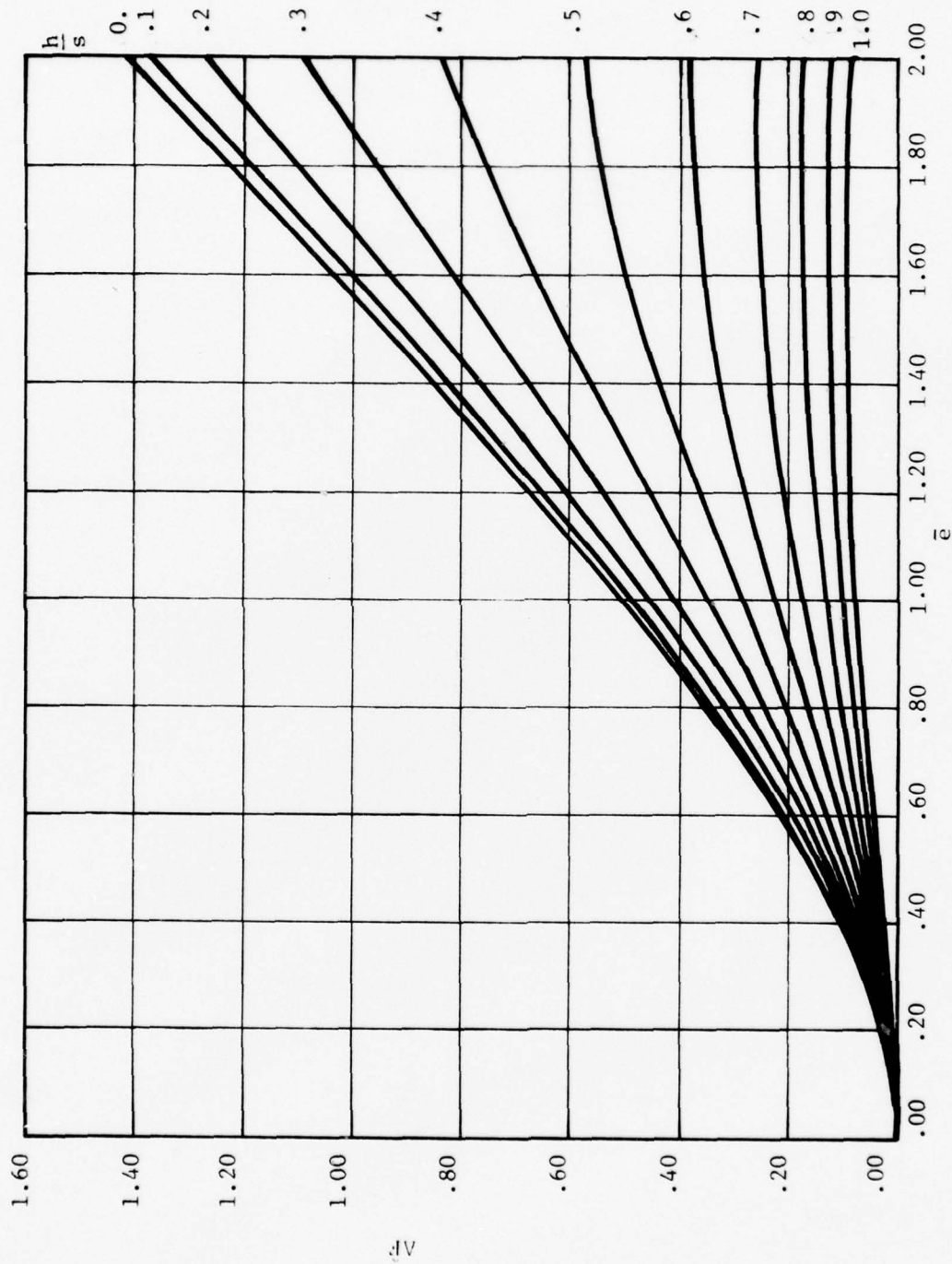


Fig. 2-6 Decrease in Normal Force (from Aligned Position) with Transverse Displacement - Straight Teeth

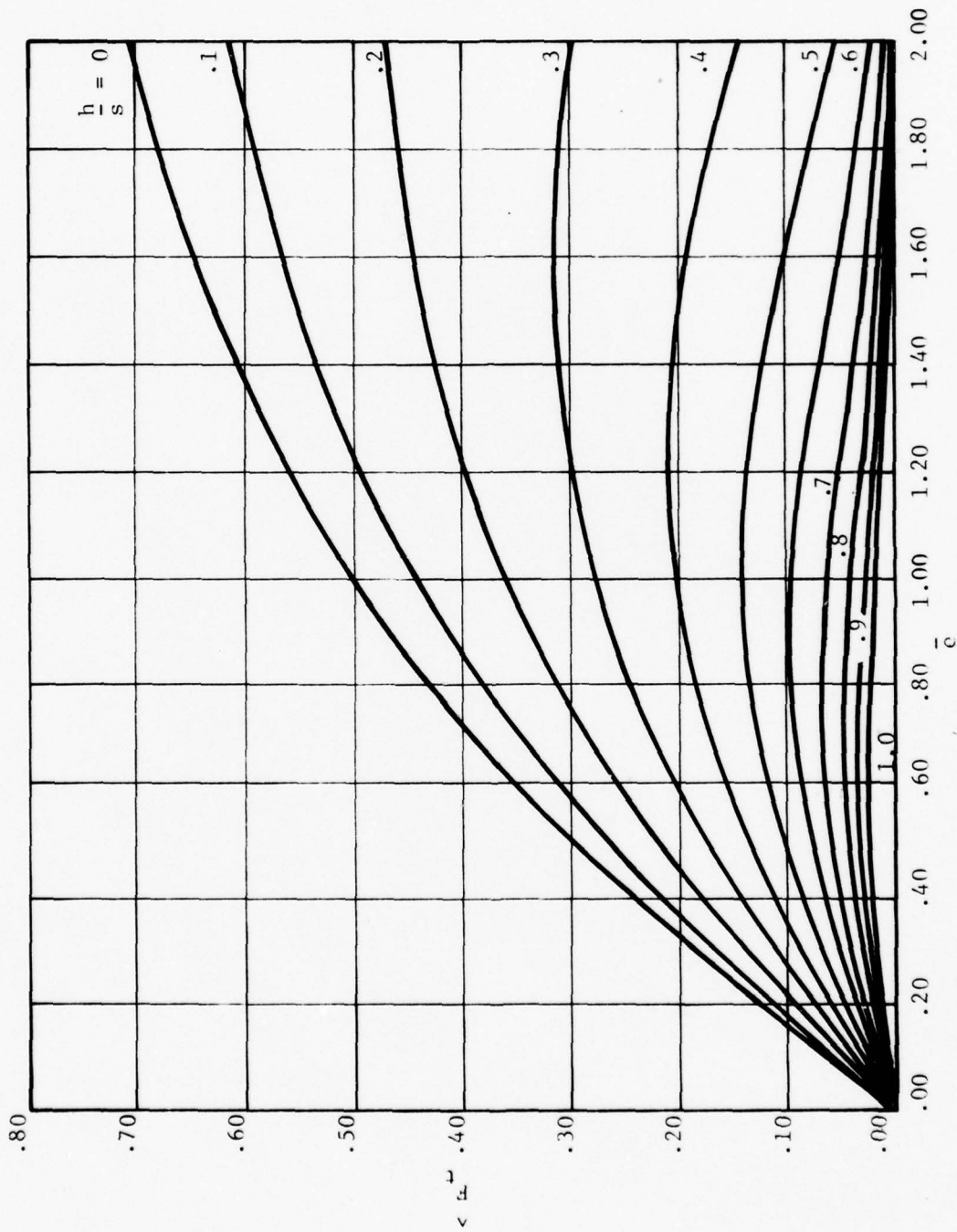


Fig. 2-7 Transverse Force Versus Transverse Displacement - Straight Teeth

air-gap permeance, the decrease in normal force, and the transverse force variation with respect to transverse displacement are shown in Figures 2-8, 2-9, and 2-10, respectively. These correspond to Figures 2-5, 2-6, and 2-7 for the straight tooth, respectively. Each of the above figures contains curves for different values of the parameter $\frac{h}{s}$. When l is replaced by πD the Figures 2-3 and 2-4 can be used to predict flux and normal force (at $\bar{e} = 0$) for the circular-tooth configuration.

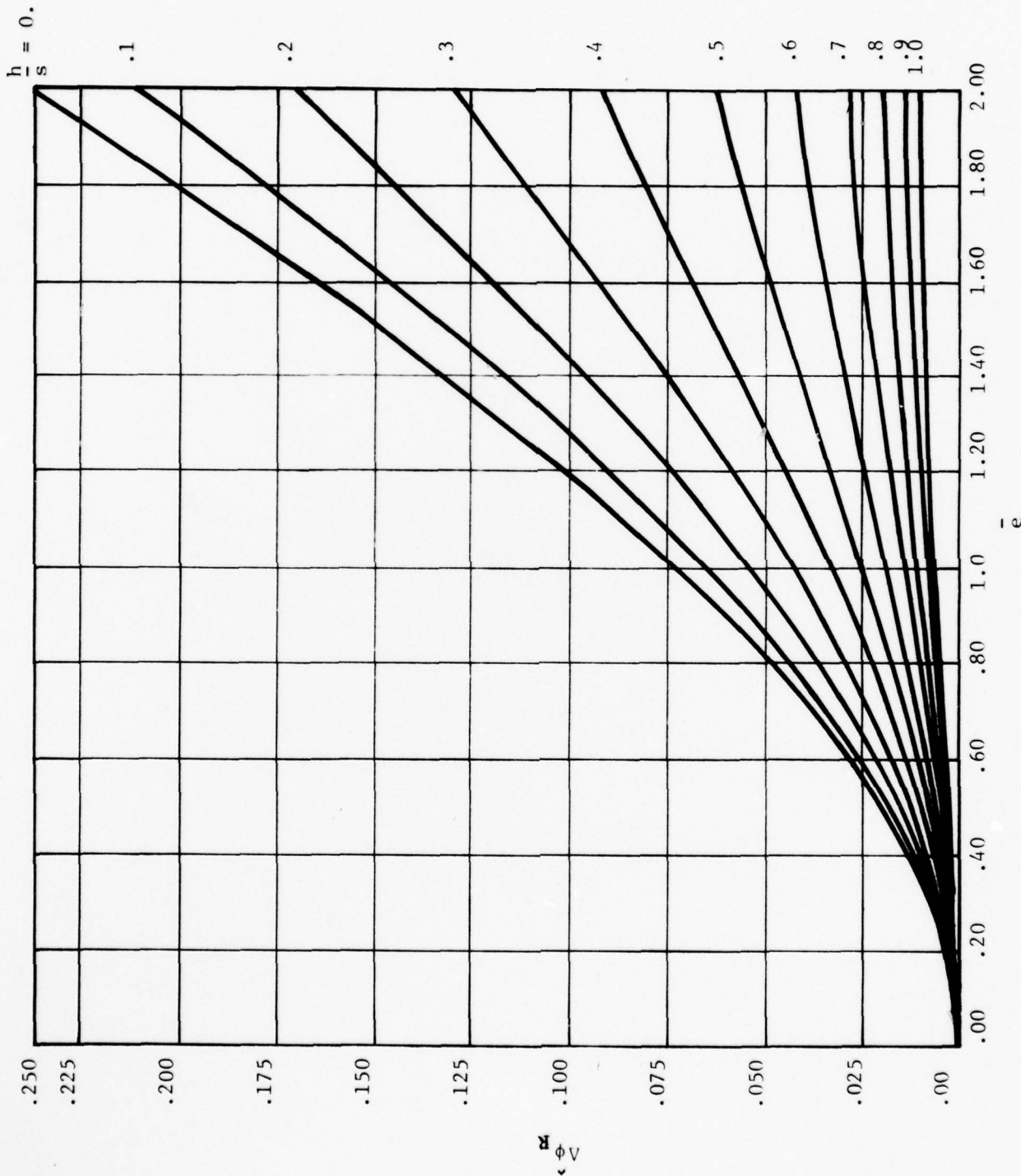


Fig. 2-8 Decrease in Air-Gap Permeance (from Aligned Position) with Transverse Displacement - Circular Teeth

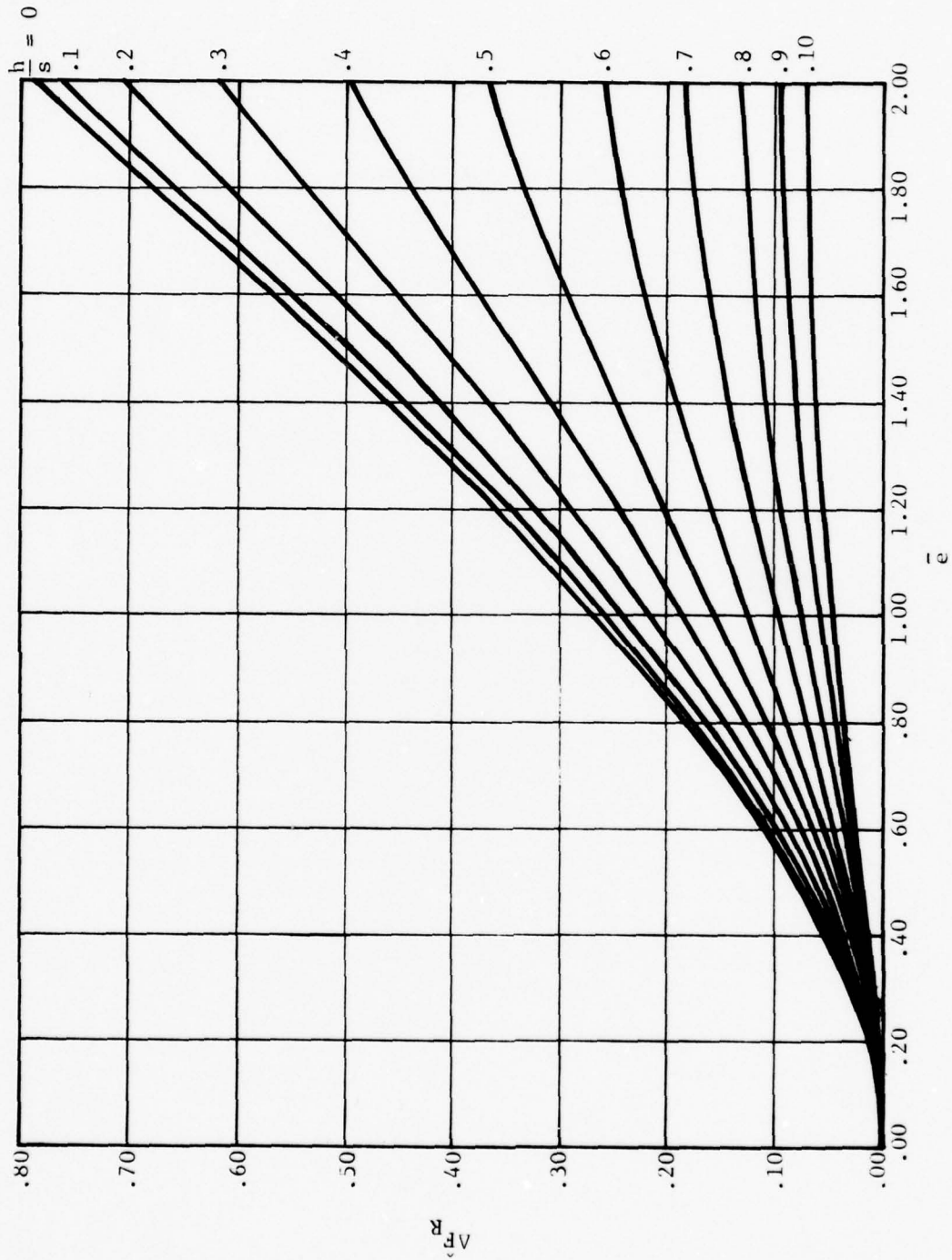


Fig. 2-9 Decrease in Normal Force (From Aligned Position) with Transverse Displacement - Circular Teeth

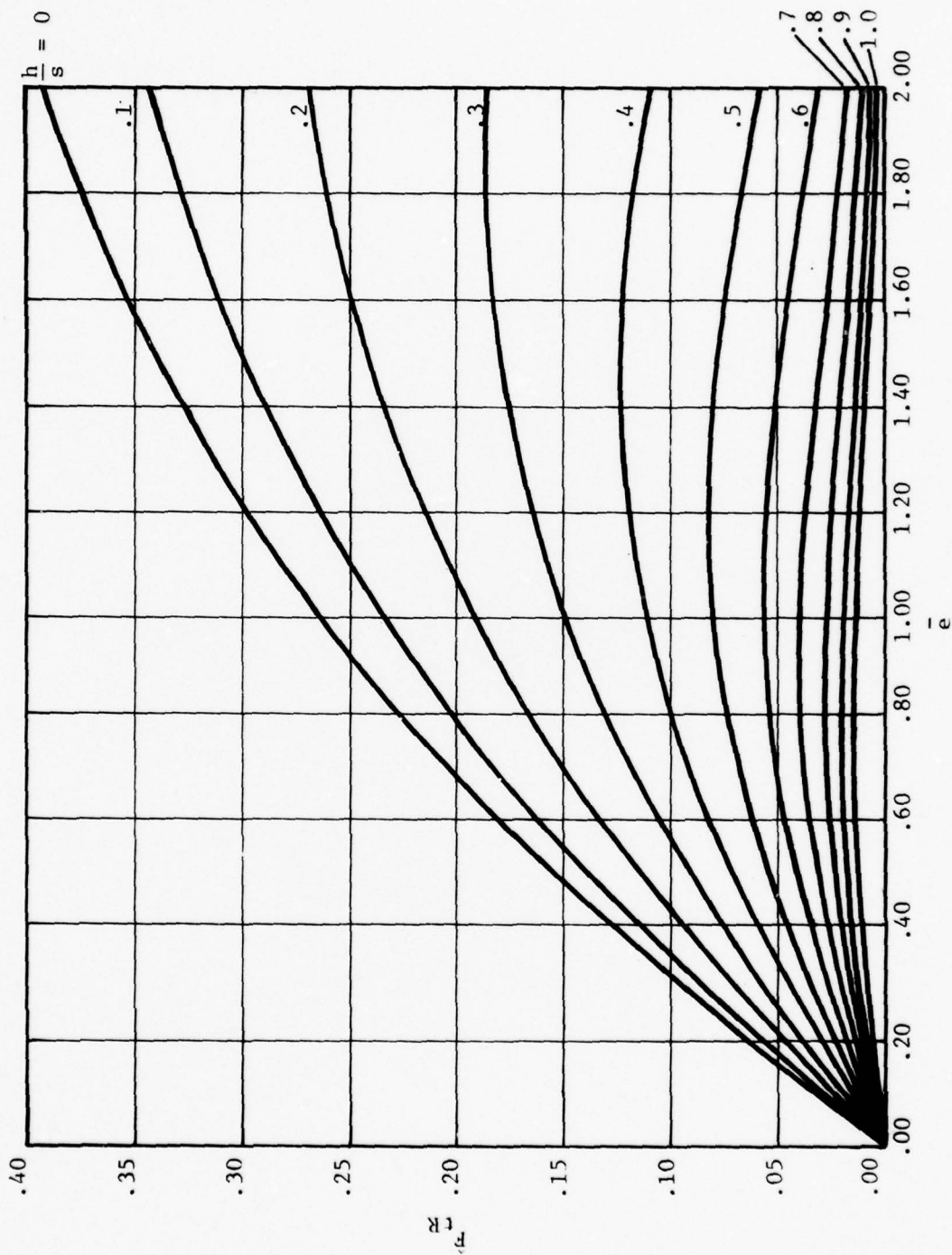


Fig. 2-10 Transverse Force Versus Transverse Displacement - Circular Teeth

3.0 DYNAMIC MEASUREMENTS FOR CLOSED MAGNETIC CIRCUIT WITH HIGH-PERMEABILITY MATERIAL

A validated theory for predicting fluxes and forces in a closed magnetic circuit was reported earlier [4]; the analytical results obtained using this theory were presented in Section 2.0 in the form of curves of nondimensional values of fluxes and forces versus gap thickness or transverse displacement at various values of tooth-geometry parameter. However, the validation was performed through measurements under static conditions.

The purpose of the research described in this section was to detect any possible effects of transverse vibration and to determine any damping that may be present in the system.

Dynamic measurement of forces was therefore performed on the same magnetic circuit used earlier [4]. Comparisons could thus be readily made. Transverse oscillations were introduced to the lower core piece (constituting one-half the magnetic circuit) using an electronic vibration system. A separate test rig was built for this study; this section describes the test rig, the associated instrumentation, and the results of the dynamic measurements performed.

3.1 Experimental Apparatus

3.1.1 Magnetic Circuit

The magnetic circuit is the same as studied previously [4] and is shown in Figure 3-1. A new test rig was constructed to permit the lower core piece to be transversely displaced in the Y-direction. A sinusoidal transverse displacement was introduced, using an electrodynamic shaker table. The upper core piece, shown in the figure, is fixed to the support housing through two three-directional force transducers. The test rig facilitates raising and lowering of the upper core piece for varying the gap thickness between the two core pieces.

The magnetizing coil consists of four separate 750-turn coils connected as shown in Figure 3-2. This arrangement was implemented in order to allow visualization and adjustment of the gap with the coils in place. A total current of 1 amp produces 1,500 ampere-turns of magnetomotive force.

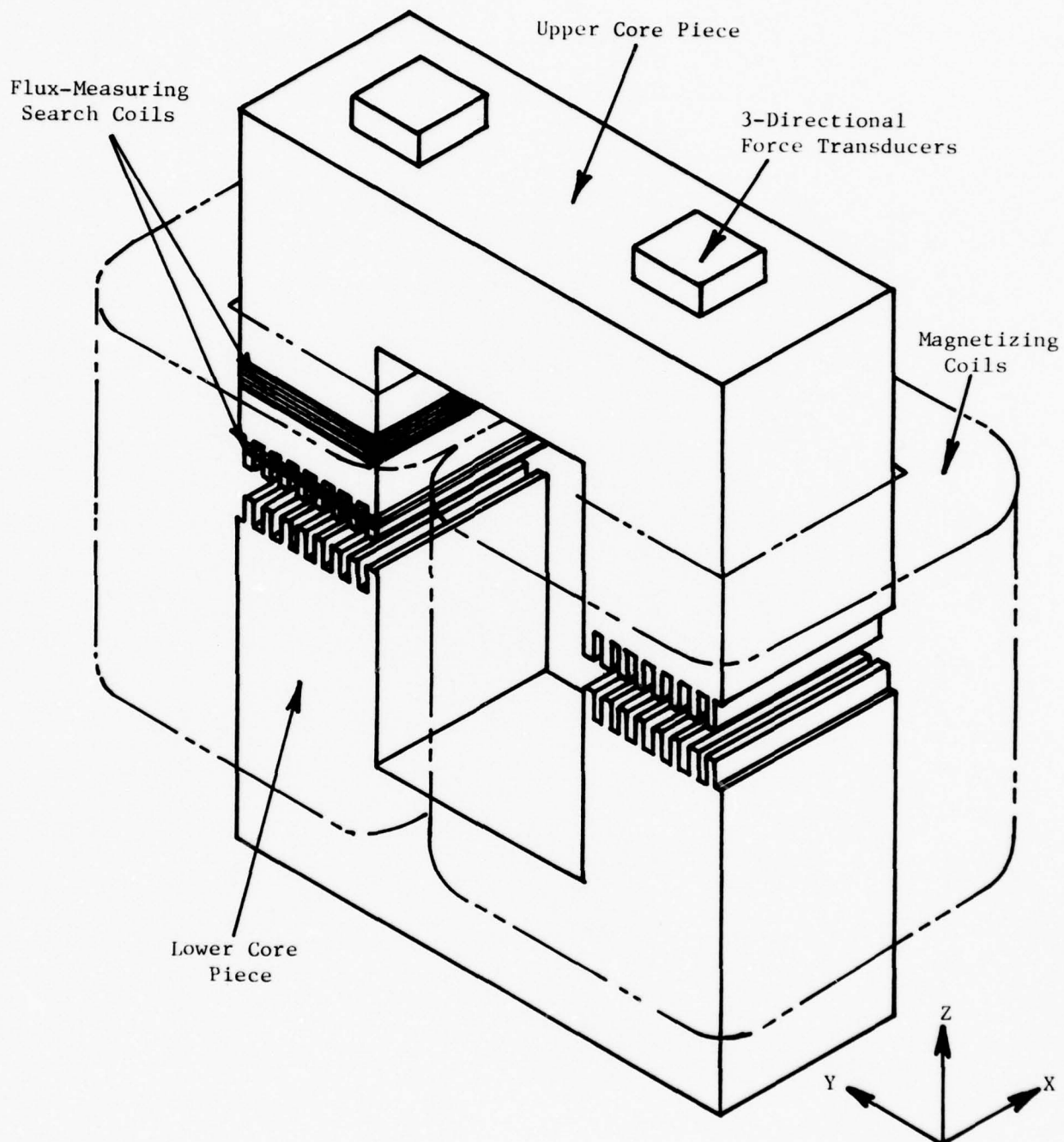


Fig. 3-1 Magnetic Test Assembly

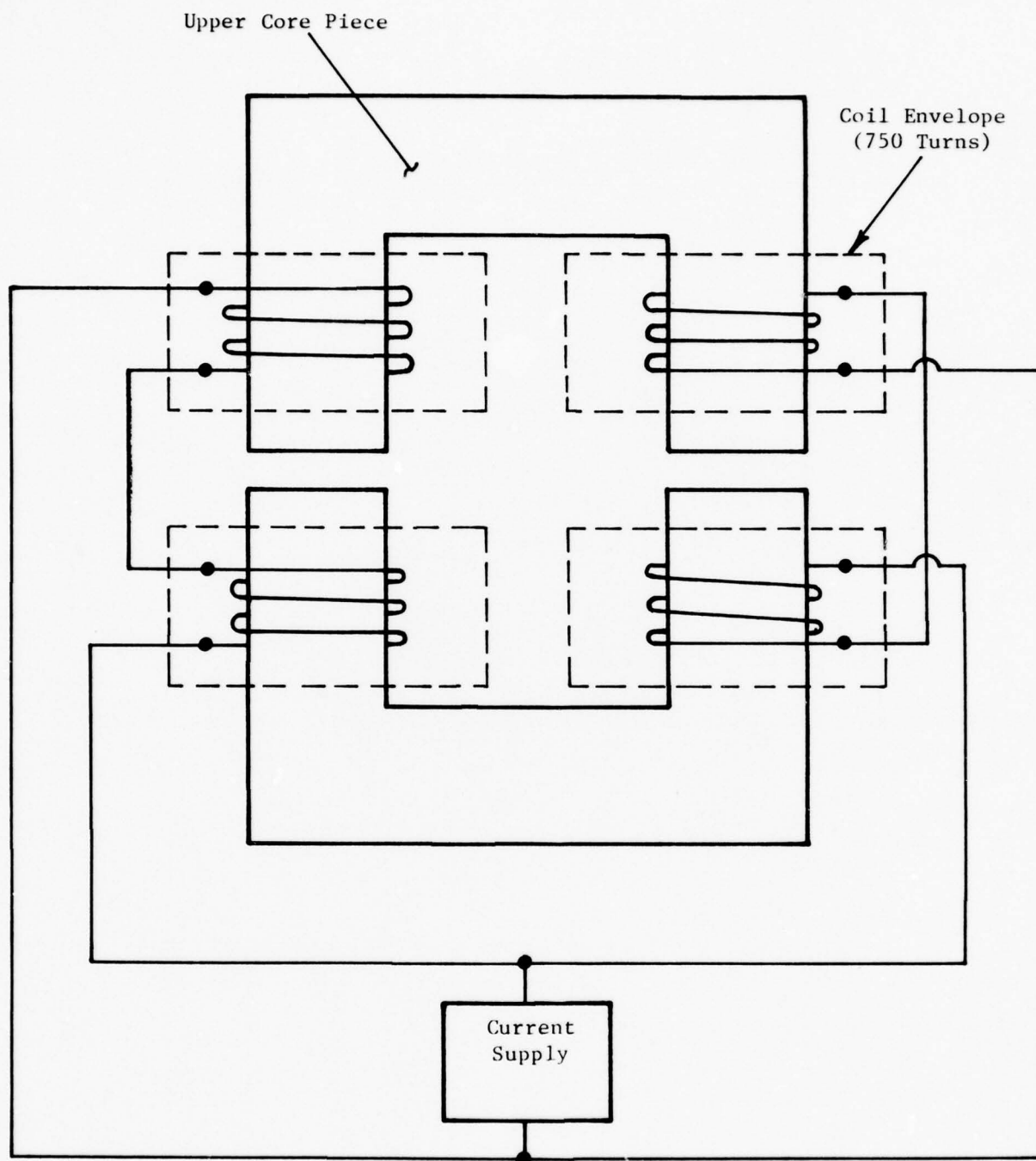


Fig. 3-2 Wiring Diagram for Magnetizing Coils

791256

The core pieces are the same as those used in the previous program. A photograph of one of the core pieces is shown in Figure 3-3. The teeth are 2.5 inches long, 0.1 inch deep with a center-to-center spacing of 0.060 inch. Each pole face contains 28 teeth, and all measurements were performed with .020-inch-wide teeth.

3.1.2 Test Rig

The test rig is shown schematically in Figure 3-4, and photographs of the rig are shown in Figures 3-5 and 3-6. The complete assembly is mounted on a machine tool bedplate (partially visible in Figure 3-5), which acts as a seismic mass. Bearing support for the driven lower core piece is provided by four Thomson ball bushing, and pillow blocks which run on two parallel shafts attached to the bottom support plate. A schematic of the arrangement is shown in Figure 3-7. The pillow-block housings act as clamps which can be adjusted to radially preload the bushings.

The upper core piece is attached to the top mounting plate through two force transducers, and this subassembly is supported by four ball-screw/ball-nut assemblies which are used to facilitate precise adjustment of the gap height between pole faces. Self-aligning pillow-block bearings attach the ball screws to the top and bottom support plates. The upper core piece can be positioned by simultaneously rotating the four ball screws through the timing belt-pulley arrangement shown. The ball screws and the ball bushings are rated for 1,000 lbf in the Z-direction and, therefore, were adequate for present testing.

Extreme care was taken to obtain precise parallelism of the magnetic faces under both static and dynamic conditions. The top of the bottom mounting plate was used as a reference surface for leveling the lower core piece. Parallelism between the ball-bushing axes and the reference surface was achieved by using shims at the pillow block and shaft mounts. Parallel motion of the reference surface along the ball-bushing shafts was verified with dial indicators. Following this, the upper core piece and ball-screw assemblies were installed with precision gage blocks separating the pole faces throughout the assembly operation to assure parallelism. The key step

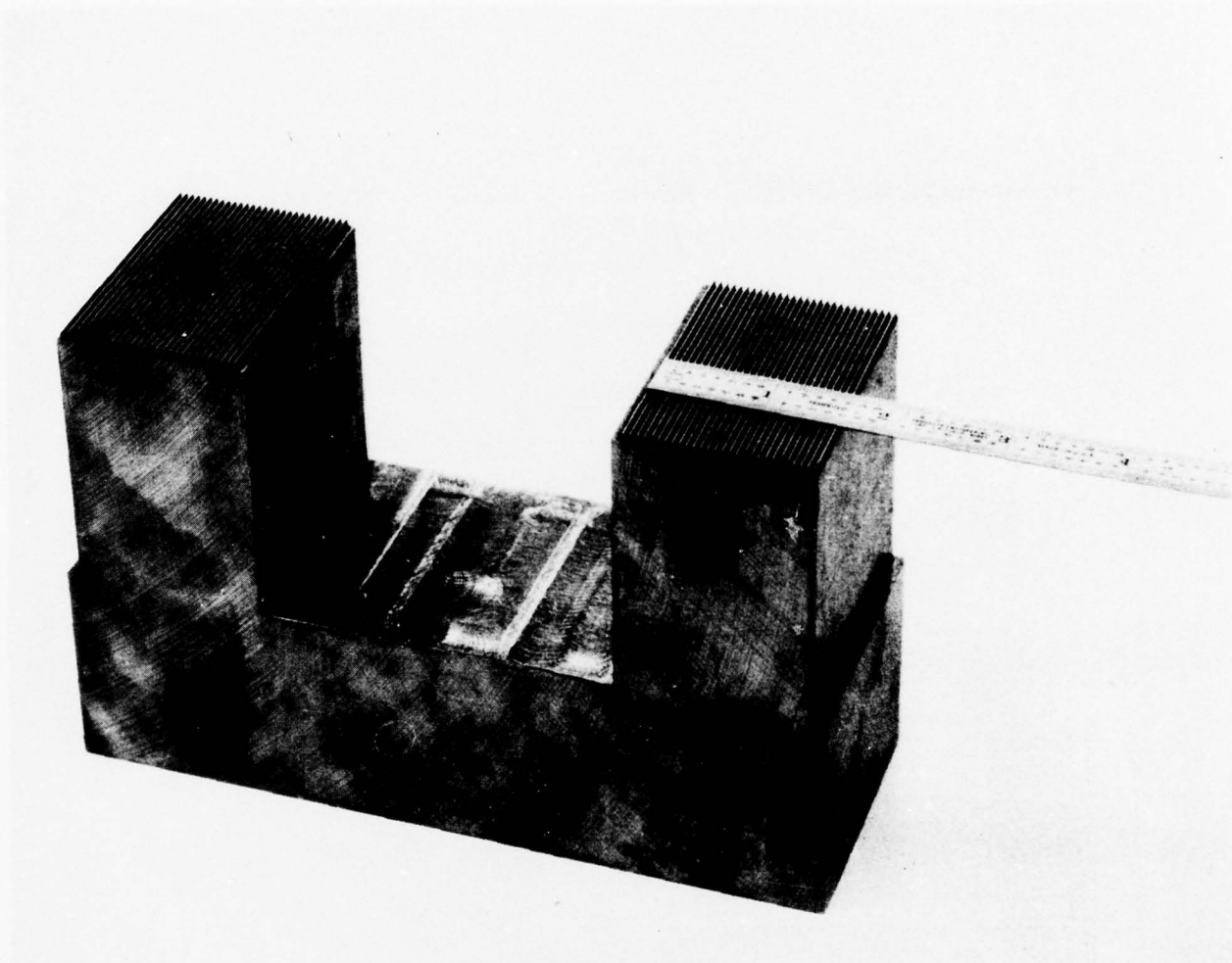


Fig. 3-3 Photograph of Core and Tooth Geometry

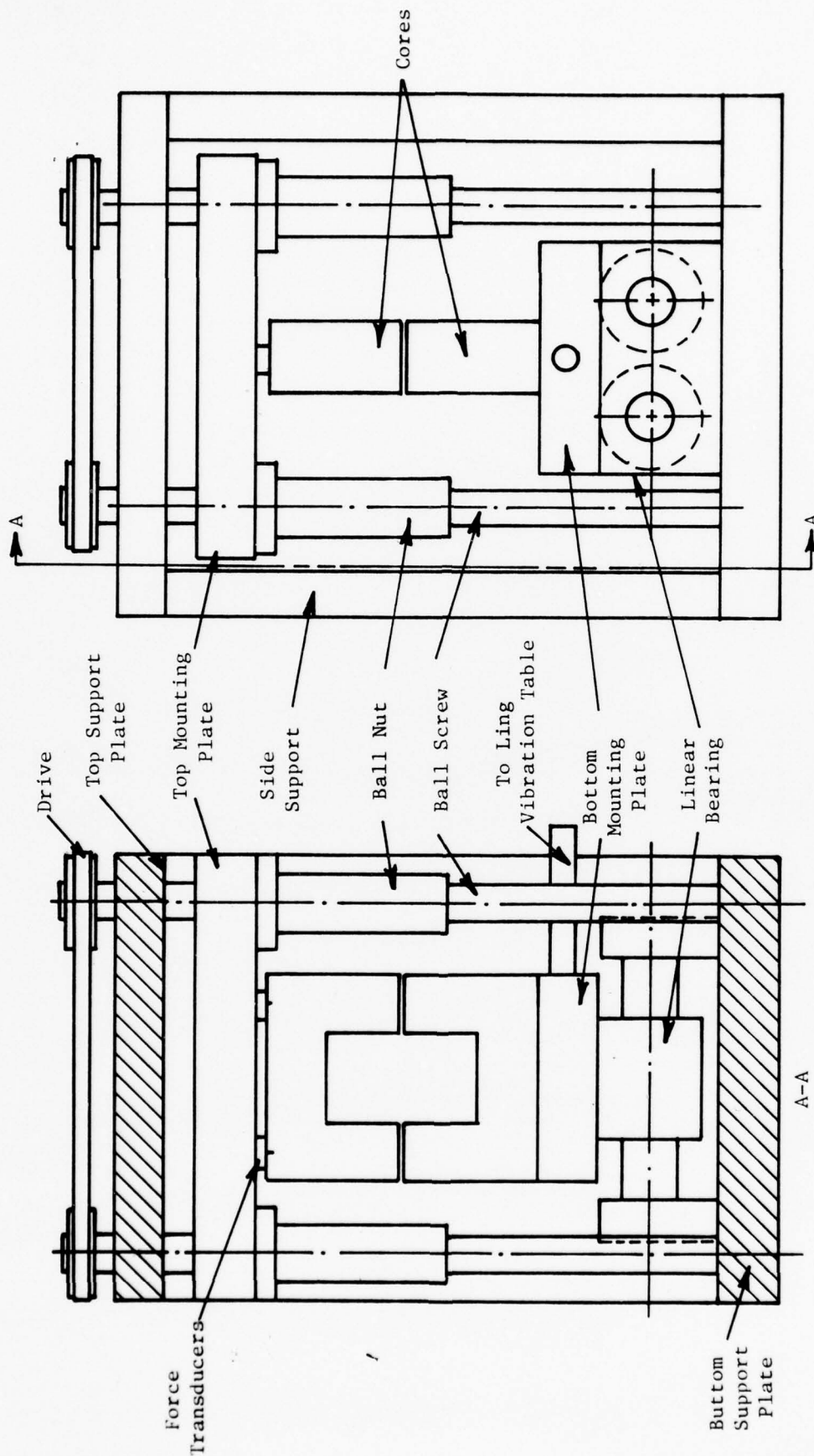


Fig. 3-4 Schematic of Test Apparatus

791257

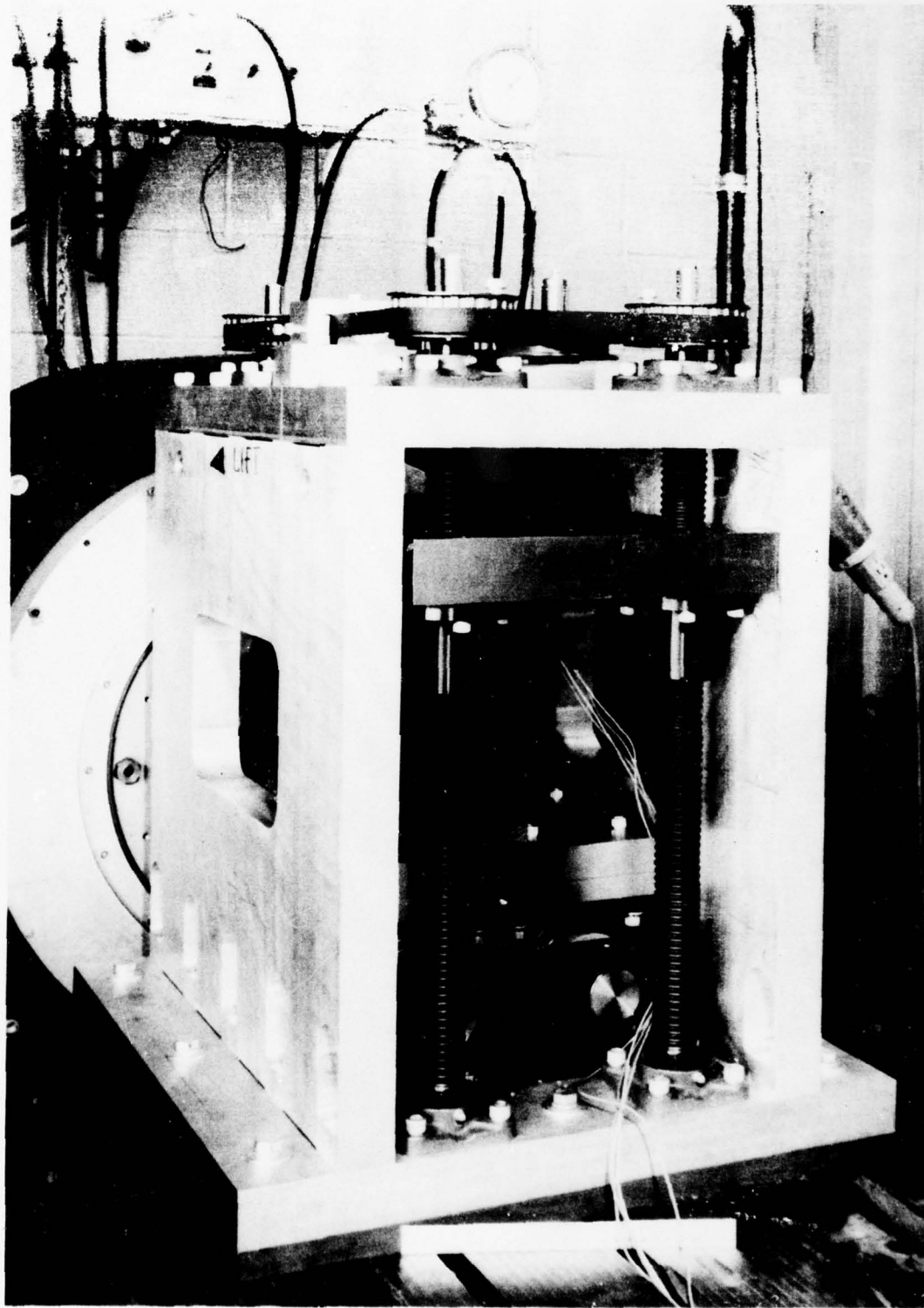


Fig. 3-5 Front View of Apparatus

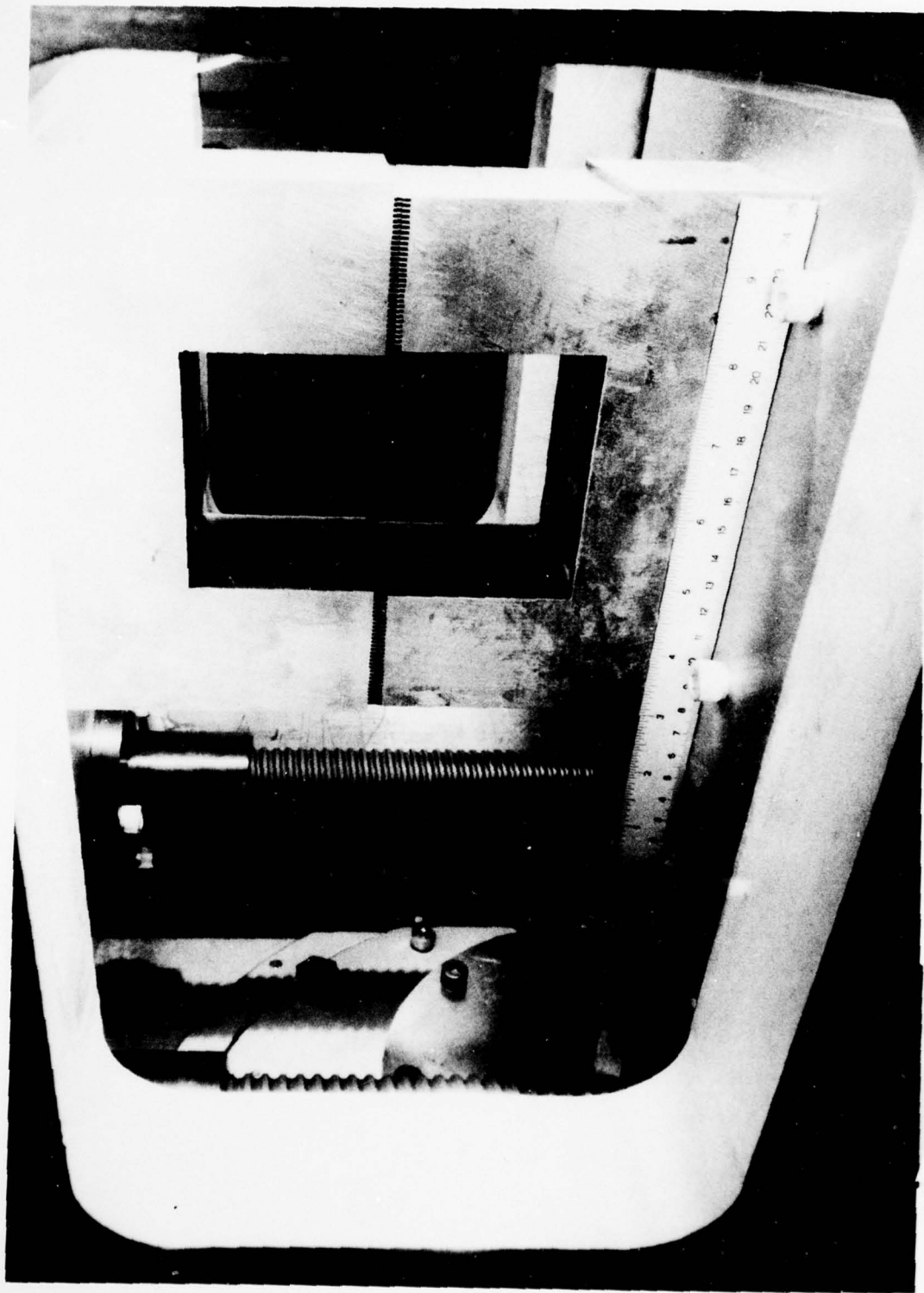


Fig. 3-6 Photograph of Magnetic Cores in Test Apparatus

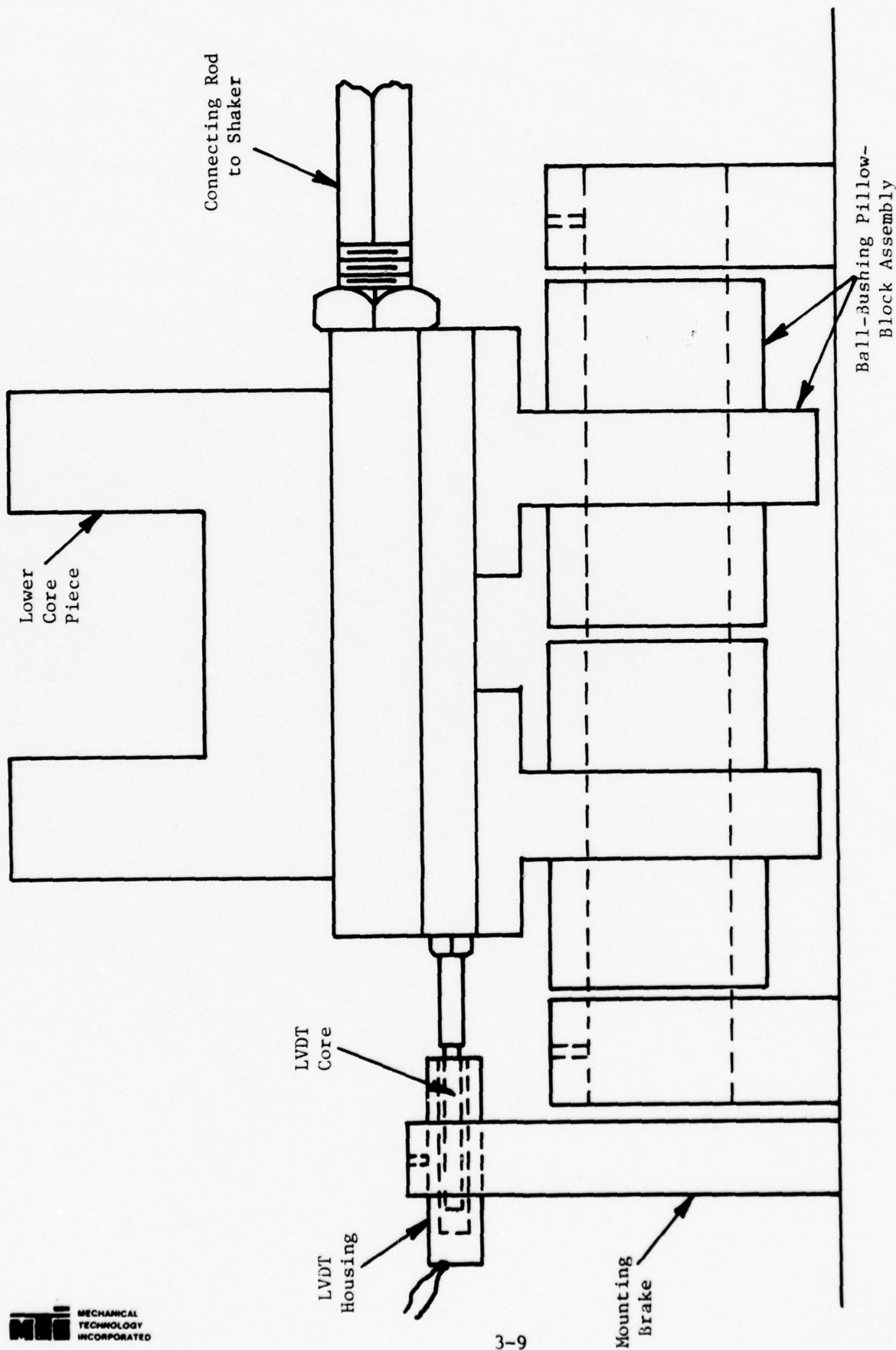


Fig. 3-7 Lower Core Piece Drive and Position Sensing Arrangement

in the assembly for assuring pole-face parallelism was to locate and drill the bolt holes for attaching the four ball nuts to the top mounting plate, with the gage blocks separating the pole faces. This nullified the potential errors in face parallelism due to tolerance stackup of the various machined parts.

To minimize the effects of any external magnetic fields, the top and bottom mounting plates were made of nonmagnetic (300 series) stainless steel, and the four support plates were made of aluminum.

The bottom mounting plate was connected to the shaker table by a hexagonal steel rod with opposite hand threads at the two ends. This was done so that the lower core piece could be displaced horizontally for static measurements by simply rotating the rod. Ling Electronics Vibration System was used to oscillate the lower core piece. The system and its test cell are shown in Figure 3-8. The system could be programmed to provide any arbitrary, periodic wave form - including random vibration. For this application, it was used to provide a purely sinusoidal excitation at a specified frequency and amplitude.

3.1.3 Measuring System

The instruments used for the static measurements and their calibration procedures are essentially the same as those used in the previous program, for which detailed descriptions can be found in Reference 4. However, this section briefly describes the instrumentation used for the static measurements. Special wave-form analysis instruments used for the dynamic measurements are described in Section 4.2.

Force was measured using two Kistler Type 9251 piezoelectric force transducers with a Kistler Model 503 charge amplifier. This system was used also for the dynamic force measurements.

Magnetic flux was measured with an LDJ Electronics Model 701 voltage integrating flux meter. The relevant static flux measurements were taken from the search coil wrapped around the teeth (10 turns), as shown in Figure 3-1. The search coil wrapped around the body of the upper core piece was used for

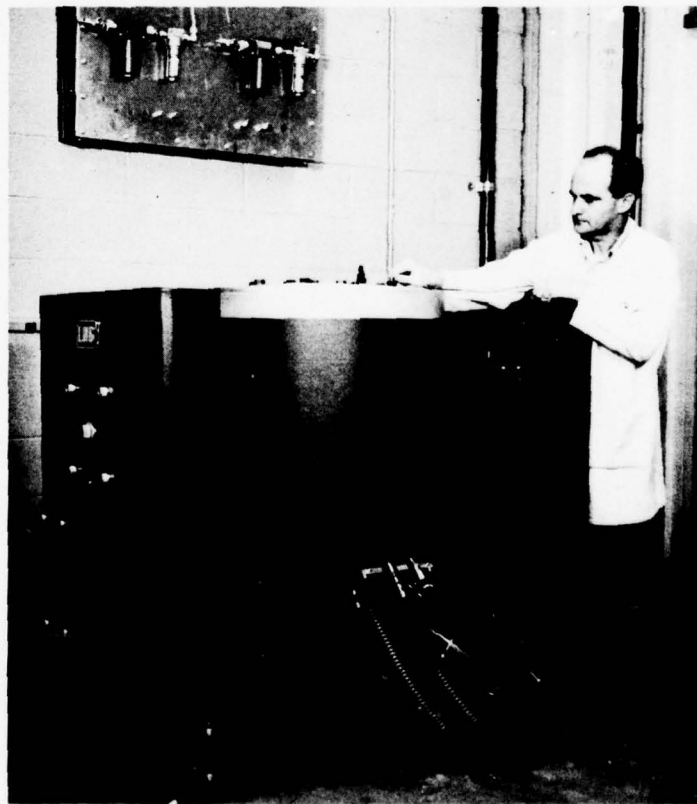
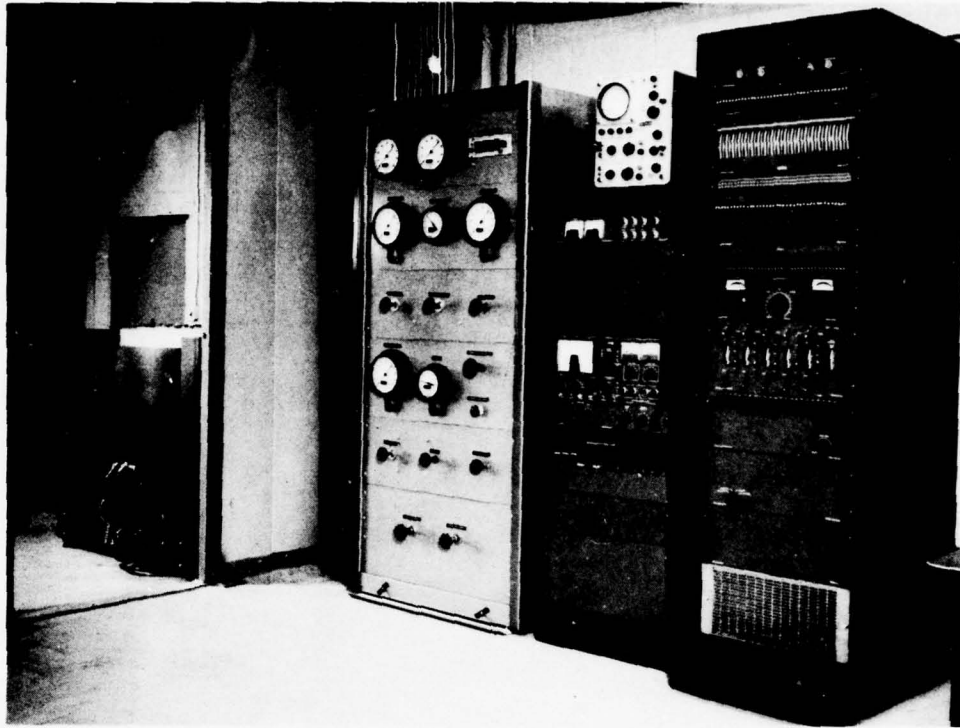


Fig. 3-8 Ling Model B335 Electrodynamic Shaker Facility at MTI-Latham

residual flux measurements while degaussing the core. The procedure used for degaussing the core is the same as that described in Reference 4.

The current source used to energize the magnetizing coils was a Lambda Model LL902-0V regulated power supply. During all measurements, the coil current was monitored on a digital ammeter, and the power supply regulation was such that current could be held constant to within 0.005 amp. When X-Y plots of force and flux versus current were generated, the plotter input representing current consisted of the voltage drop across a 0.1-ohm precision resistor connected in series with the power supply.

A Schaevitz Model 100 DCD LVDT (Linear Variable Differential Transformer) was used to measure the horizontal (tangential) displacement of the lower core piece under both static and dynamic conditions. The LVDT is linear over a wider range than the capacitance probe system used previously. Figure 3-7 shows the setup for the LVDT. Its output sensitivity is 101.562 volts per inch with a range of ± 0.1 inches. Linearity is 0.064 percent of full range. The LVDT operates on a ± 15 -volt DC power supply.

For all measurements, the pole-face gap was set initially using shim stock and then monitored during the test using a .050-inch-range capacitance probe with a Wayne-Kerr Model DM100 distance meter. Resolution of this system was better than 0.5 percent of full scale, or 250 microinches. The probe was attached to an aluminum bracket on the bottom mounting plate, and in this manner, any changes in gap due to deflections of the ball screws or ball bushings under high magnetic forces were detectable.

The LVDT and capacitance probe outputs were monitored during all measurements using two Data Precision Model 2440 multimeters.

The data were plotted directly using a Houston Omnigraphic Series 2000 X-Y plotter. Dynamic wave forms were monitored on Tektronix Type 504 dual-trace oscilloscopes and photographed at relevant data points.

3.2 Static Measurements

In the previous research program [4], excellent agreement was obtained between experimental measurements and theoretical predictions of magnetic forces and flux. These measurements were highly repeatable, giving a high level of confidence in the instrumentation and experimental procedures utilized.

Following the assembly of the new test rig for the present program, these static measurements were carefully repeated as a check on the integrity of the new rig. Results were highly affirmative, with the new test rig either reproducing the previously measured data or, in some cases, giving improved agreement with theory over the previous data.

However, two sources of error which had to be accounted for were present in the measurement of transverse forces. The radial compliance in the ball-bushing pillow blocks and axial compliance in the ball nuts caused the gap to decrease as the current, and thus axial force was increased. At the same time, radial compliance in the ball nuts permitted the onset of tangential force to slightly shift the horizontal position of the upper core piece. Only under conditions when the normal forces were very high (≈ 300 lbf), the data were not perfectly reproducible. At other conditions, the horizontal deflection of the upper core assembly was negligible, and the decrease in gap could be compensated for by making the gap setting equal to the desired gap plus the expected vertical deflections of the ball nuts and ball bushings.

3.3 Flux and Transverse Force Measurements Under Dynamic Conditions

One of the primary goals in performing dynamic measurements of the tangential force was to quantitatively determine the degree of damping present in a magnetic suspension under a given set of conditions. It is hypothesized that the tangential or passive transmission of force across the pole-face gap takes place through an effective spring and dashpot acting in parallel so that the restorative and dissipative force components are directly additive. The restorative or spring force is due to the tendency of the field to force the teeth into alignment, and the dissipative or damping force is due to eddy current and magnetic hysteresis losses which arise from a time varying flux.

For an arbitrary, nonlinear force wave form measured at the upper core piece load cells in response to a purely sinusoidal oscillation of the lower core piece, the energy dissipated per cycle is given exactly by the expression (because of the orthogonality relations for the Fourier eigenfunctions):

$$E_D = \pi \delta F_0 \sin \alpha, \quad (3-1)$$

where δ is the amplitude of oscillation of the lower core piece, F_0 is the amplitude of the first harmonic of the force wave form, and α is the phase angle by which the first harmonic of the force wave form leads the purely sinusoidal displacement wave form. α is a good indicator of the degree of damping in the system. In fact, for a linear system

$$\frac{D}{D_c} = \frac{1}{2} \tan \alpha$$

where D is the damping coefficient in the system and D_c is the critical damping coefficient.

3.3.1 Instrumentation for Wave-Form Analysis

Measurement of the amplitude of the first harmonic of the tangential force wave form F_0 and its phase angle, with respect to the lower core piece motion wave form α , was accomplished using VIC (Vibration Instruments Co.) Model 235DS Dual-Channel Tracking Analyzer, and a Dranetz Model 305 Phasemeter.

The tracking analyzer is an electronic system which acts as a narrow bandwidth filter, of which the center frequency is precisely and automatically tuned to follow (track) the fundamental frequency of a varying, external reference signal. The dual-channel unit used here consists of two parallel filters tuned to a common reference. The two filter channels are phase matched to within 1 degree so the output signals, which are purely sinusoidal, can be fed into a phasemeter to measure the phase angle between the input signals.

For the tangential force measurement, the lower core piece motion wave form is fed to the reference input and one of the two filter channels (Channel A). The tangential force wave form is fed to the second filter channel (Channel B). This arrangement is shown schematically in Figure 3-9. The voltmeter provides

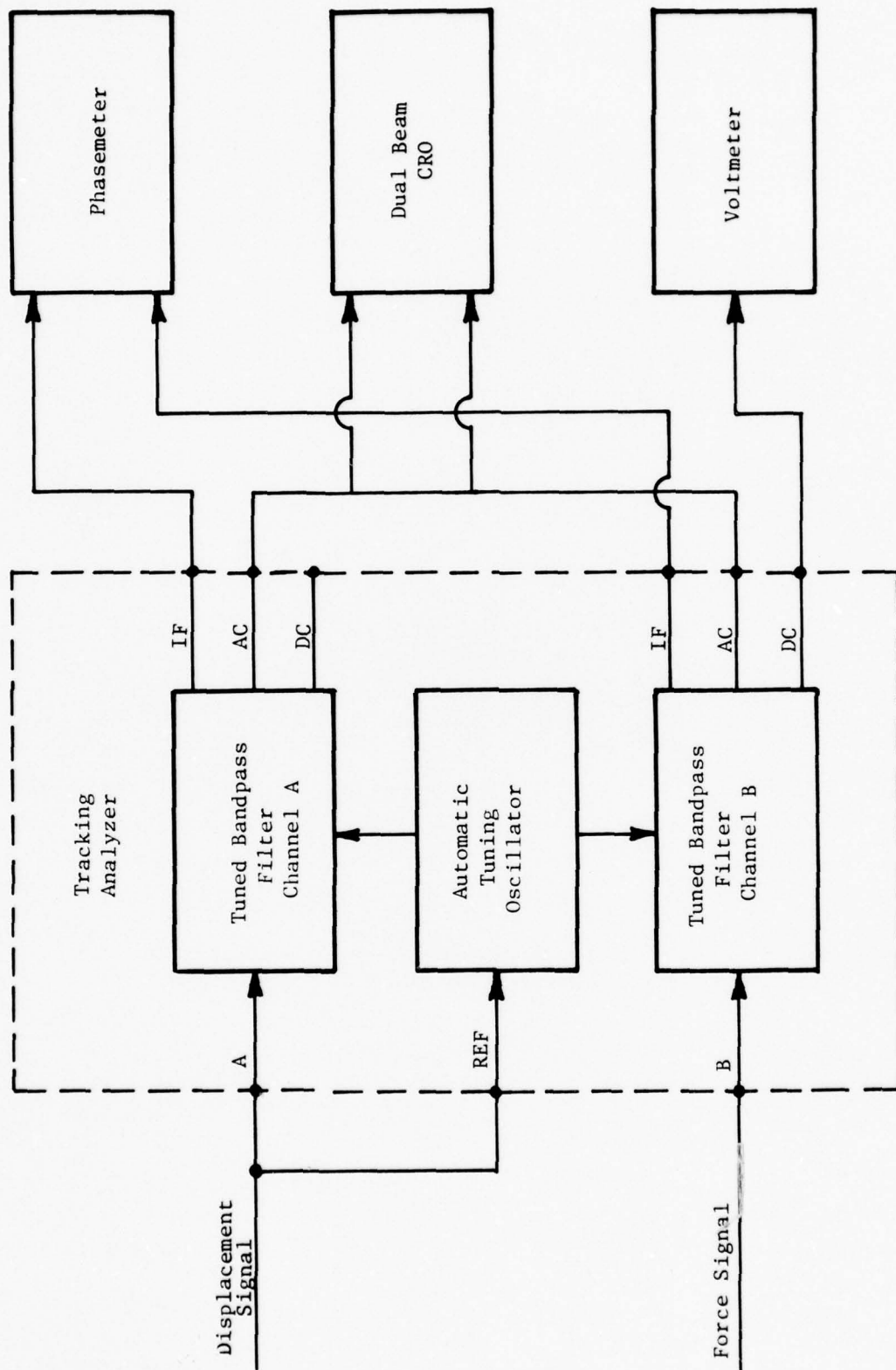


Fig. 3-9 Schematic of Tracking Analyzer Setup for Dynamic Force Measurement

791259

a digital display of the rms value of the first harmonic of the force wave form F_o , and the phasemeter gives a digital display of the phase angle α .

3.3.2 Dynamic Rig Checkout

3.3.2.1 Tracking Analyzer and Phasemeter. Dynamic data were desired over a frequency range of 20 Hz to 100 Hz, so the instrumentation was checked out over a much wider frequency range. In setting up the tracking analyzer and phasemeter, extensive care was taken to ensure that there would be no superfluous indication of phase angle.

It was determined by an independent check-out procedure that both analyzer channels must have the same range setting and that the amplitudes of the inputs to the tracking analyzer have the same magnitude. (A resistive attenuator can be used to accomplish this.) Under these conditions, the phasemeter could be zeroed to ± 0.2 degrees.

3.3.2.2 Complete Rig Checkout. Check-out tests were performed with a 10-mil gap at flux levels of 90 and 135 kilolines. Lower core piece oscillation frequencies ranged from 20 to 80 Hz, with amplitudes ranging from ± 0.004 to ± 0.010 inch.

Initially, structural vibration problems were encountered at frequencies above 50 Hz, due primarily to radial (horizontal) compliance in the ball-screw/ball-nut assemblies. The excitation was through the magnetic force transmission at the pole-face gap and a small dynamic force transmitted radially through the ball bushings due to the slight error in colinearity between the ball-bushing axes and the shaker-drive axis. This structural, vibration-threshold frequency was increased from 50 Hz to 70-80 Hz, giving a range of 20-60 Hz over which dynamic data could be acquired with a high level of confidence by implementing clamping bolts between the side supports and the top mounting plate.

In the initial attempt at measuring the phase angle between tangential force and displacement, the LVDT was used to generate the displacement signal, and the indicated phase angles appeared suspiciously large. However, by measuring

the phase angle between the LVDT signal and the signal given by an accelerometer mounted on the lower core piece, it was established that the major portion of the indicated phase angle between force and displacement was due to differences in the electronic phase shifts introduced by the LVDT and the charge amplifier used with both the accelerometer and the force transducers.

This situation was remedied by basing the phase measurement on a comparison between the force transducer and accelerometer signals by using the LVDT as an indication of motion amplitude only. Kistler Model No. 503 charge amplifiers were used with both the force transducers and the accelerometer. The two charge amps were found to produce zero net phase shift as long as their range and sensitivity settings were identical. This was established by pairing the two identical force transducers with two charge amps and measuring the phase angle between the charge-amp outputs. While the raw transducer signals are naturally in-phase since both transducers are mounted between the same rigid members, it was possible to generate a significant indicated phase angle between the charge-amp outputs by varying the sensitivity of one charge amp relative to the other. With identical sensitivities, the phasemeter indicated zero to within $\pm 1^\circ$ at frequencies up to 70 Hz, giving the complete phase-measuring system a resolution of $\pm 1^\circ$.

3.3.3 Experimental Procedure

The connecting rod between the shaker and the lower core piece support was adjusted so that the oscillation took place about the position of complete tooth alignment. The static LVDT output level corresponding to this position was marked on an oscilloscope, and with the rig operating, the connecting rod was adjusted for each data record until the DC level of the LVDT-output waveform coincided with the marking.

The midpoint of the shaker-table motion showed a tendency to drift somewhat, particularly at lower frequencies and amplitudes. This drift tended to be unpredictable and could not always be compensated for by connecting-rod adjustments, resulting in some inaccuracies in the data. Furthermore, while the frequency of the shaker-table motion showed no tendency whatever to drift from the set value, the motion amplitude did tend to drift somewhat, making it necessary to record the LVDT-output amplitude.

An additional source of error was due to the variation in axial force with tangential position and the resulting gap variation.

3.3.4 Experimental Results and Discussion

3.3.4.1 Phase Angle. Phase angle between the tangential force and the tangential displacement was measured under the following conditions: .005- to .020-inch gap, 0 to 60-Hz frequency, 0 to $\pm .010$ -inch amplitude of transverse oscillation, and at 90- and 135-kilolines flux. In all of the above cases, the phase angle measured was less than or equal to the resolution of the phase angle measuring system (resolution is approximately $\pm 1^\circ$). Under these conditions, even if the system possessed some damping (which is within the limit of resolution of the measuring system), the magnitude is extremely small and inadequate for any practical bearing application.

3.3.4.2 Tangential Force. Plots of the measured, tangential-force amplitudes as a function of the measured motion amplitudes are shown in Figures 3-10 and 3-11. The corresponding measured static forces are shown on each plot for comparison. It is notable that in most of the cases shown there is a marked decrease in the force-amplitude level with increasing frequency at a fixed-motion amplitude with the static case corresponding to zero frequency. Even though there are sources of inaccuracy in the previously described data which are difficult to quantify, the data appear to show with sufficient regularity, particularly the cases of 90 kilolines at .005-inch gap and 135 kilolines at .010-inch gap, that the phenomenon of a decrease in the passive force response with increasing frequency is real.

Figure 3-12 shows the tangential force wave form at a motion amplitude of .005 inch (a normal motion level) and an amplitude of .016 inch (an extreme level in view of the .020-inch tooth width). The apparent, pure sinusoidal character of the .016-inch wave form confirms the predominant linearity of the tangential force-displacement characteristic over a wide range of motion amplitudes.

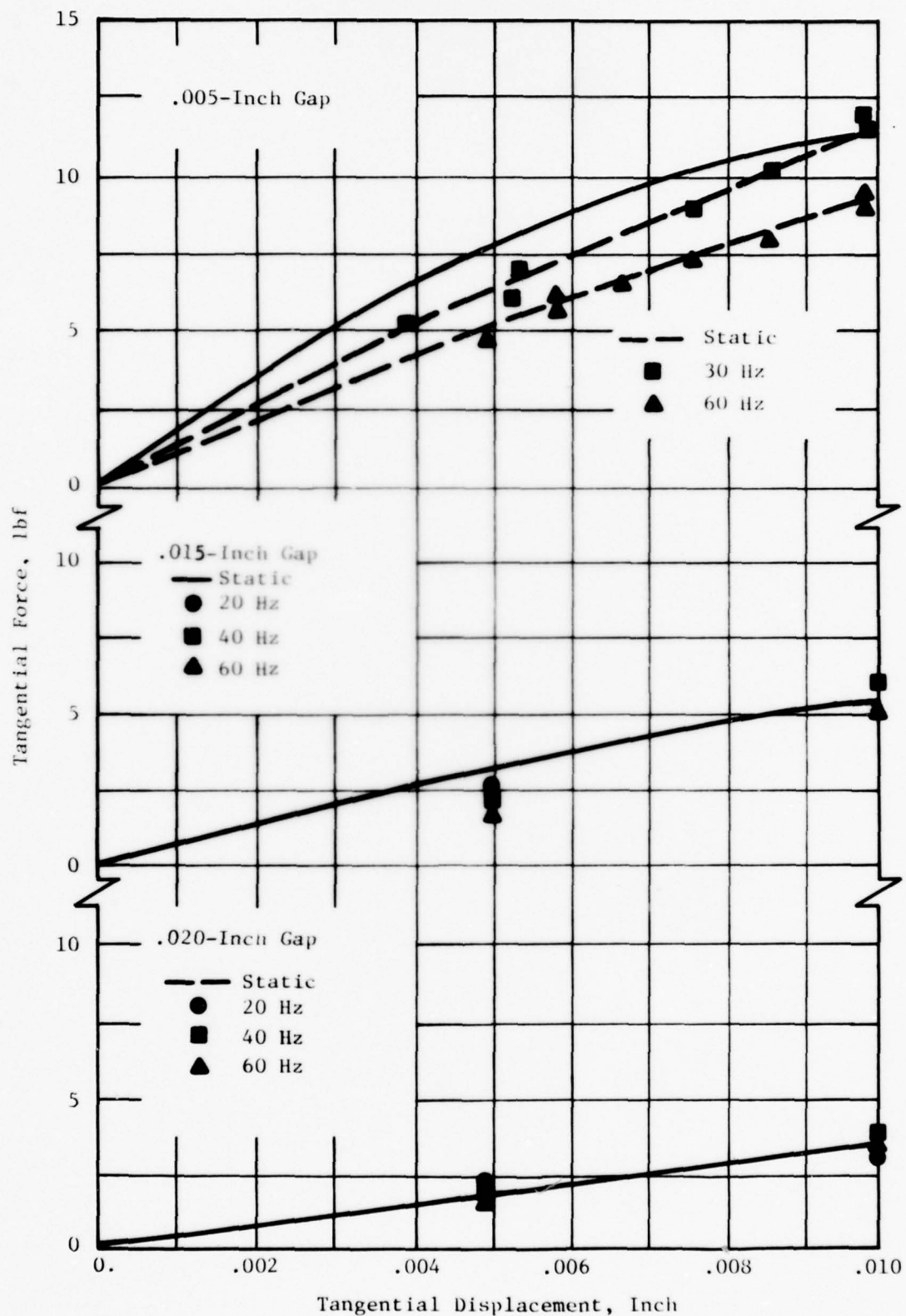


Fig. 3-10 Measured Tangential Force Amplitudes at 90-Kilo-
lines Flux; .005-, .015-, .020-Inch Gaps

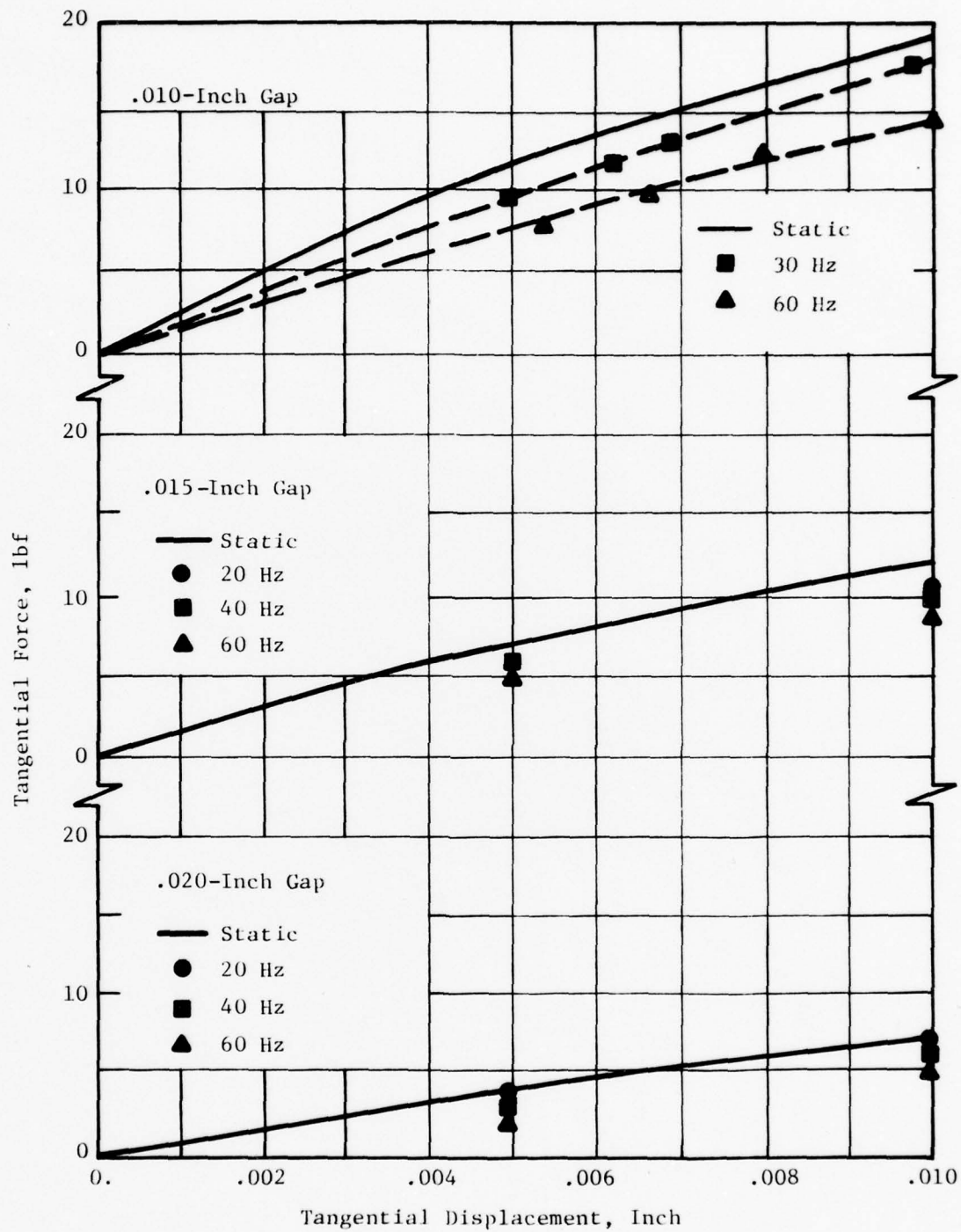
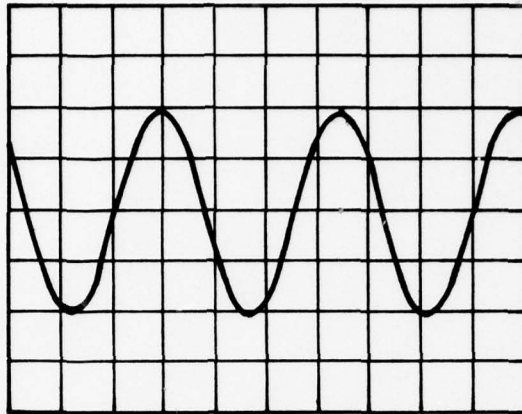
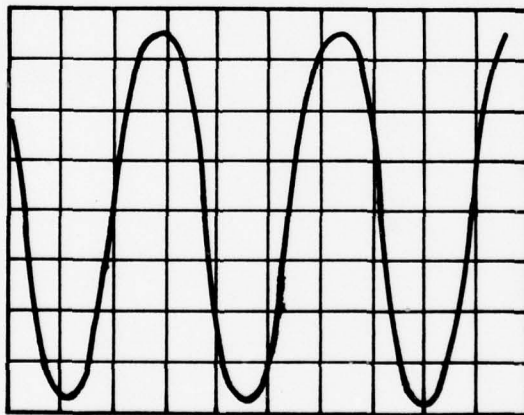


Fig. 3-11 Measured Tangential Force Amplitudes at 135-Kilolines Flux; .010-, .015-, .020-Inch Gaps



(i) $\pm .005$ -Inch Motion

Hor. Axis: .010 Sec/Div., Ver. Axis: 5 lbf/Div.



(ii) $\pm .016$ -Inch Motion

Hor. Axis: .010 sec/Div., Ver. Axis: 5 lbf/Div.

Fig. 3-12 Sample Tangential Force Wave Forms
at 135-Kilolines Flux, .010-in. Gap,
30-Hz Frequency

791262

4.0 ANALYSIS OF PERMANENT MAGNETS IN REPULSION

The previous sections of the report described the study performed on closed-circuit, electrically energized magnetic systems employing high-permeability material.

This and the following sections of the report describe the study of permanent magnets in both open- and closed-circuit systems.

With the progress in the science and technology of magnetic materials, permanent magnets are being utilized in a variety of applications, some of which involve heavy loads [5]. If constant field strength of high values is the virtue of the permanent magnet, electromagnet has the advantage of ease with which its field strength can be varied (simply by varying the current through the coil). In any practical application, the two kinds of magnets can be used in combination to derive the advantages of both.

In this section, a report is made of the analytical study performed on open-circuit magnetic suspensions. The objective here is to calculate both the normal and transverse forces between two repelling permanent magnets. Because of their significantly enhanced properties, high-coercivity rare-earth-cobalt permanent magnets are considered here. Although the approach is fairly general, the analysis procedure discussed is more convenient for the analysis of high-coercivity permanent magnets.

It has been shown by Tsui et al [6] that, for the analysis of high-coercivity permanent magnets (like those of samarium cobalt or praseodymium cobalt) in repulsion, the intrinsic material properties are the relevant ones. In repulsion applications the magnetization or the intrinsic induction M is the important property. For the rare-earth-cobalt alloys, Senno and Tawara [7] have shown that the intrinsic hysteresis loops (M versus H) are very nearly square in shape. This means that the magnetization M is a constant for values of the demagnetizing field, less than the coercive field intensity. The relation between the flux density B and the field intensity H for a rare-earth-cobalt magnet, therefore, takes on the form

$$B = \mu_0 H + M, \quad (4-1)$$

where M is independent of B and H , and μ_0 is the permeability of the surrounding space. The relative permeability for the magnet has been assumed to be unity.

In magnetostatic field problems it is customary to use a vector potential from which the field parameters can be calculated. Thus the vector potential \bar{A} may be defined as [1]

$$\nabla \times \bar{A} = \bar{B} \quad (4-2)$$

where ∇ is the vector differential operator. The requirement that the divergence of vector \bar{B} be zero (one of Maxwell's electromagnetic field equations) is automatically satisfied by Equation (4-2) because of a vector identity.

In a region of uniform permeability if \bar{i} is the current density, it has been shown that [1]

$$\bar{A} = \frac{\mu_v}{4\pi} \int_V \frac{\bar{i} dv}{r} \quad (4-3)$$

where μ_v is the permeability and r is the magnitude of the radius vector \bar{r} .

In permanent magnets, the magnetization \bar{M} can be thought of as the magnetic moment per unit volume of the permanent circulating currents. The vector magnetic potential for \bar{M} is therefore written as [1]:

$$\bar{A}_M = - \frac{1}{4\pi} \int_V \frac{\bar{M} \times \bar{r}}{r^3} dv = - \frac{1}{4\pi} \int_V \bar{M} \times \nabla \left(\frac{1}{r} \right) dv. \quad (4-4)$$

By using vector identities and Gauss's Theorem, Equation (4-4) can be written as [1]

$$\bar{A}_M = \frac{1}{4\pi} \int_V \frac{\nabla \times \bar{M}}{r} dv + \frac{1}{4\pi} \int_S \frac{\bar{M} \times \bar{n}}{r} dS, \quad (4-5)$$

where \bar{n} is the unit vector normal to the surface S bounding the volume V . The first integral on the right-hand side of Equation (4-5) is a volume integral and therefore, by comparing this with the integral in Equation (4-3),

$\nabla \times \bar{M}$ can be thought of as the volume current density. $\nabla \times \bar{M}$ has to be divided by μ_v in order to get the familiar units of (A/m^2) . Therefore, the equivalent volume-current density for a permanent magnet due to \bar{M} is

$$\bar{J} = \frac{\nabla \times \bar{M}}{\mu_v}, \quad (4-6)$$

where \bar{J} is in Amp/(meter)². Advancing a similar treatment, an equivalent surface-current density for a permanent magnet due to \bar{M} is

$$\bar{K} = \frac{\bar{M} \times \bar{n}}{\mu_v}, \quad (4-7)$$

where \bar{K} is in Amp/meter.

The magnetization \bar{M} in a permanent magnet can therefore be represented equivalently by a volume-current density given by Equation (4-6) and a surface-current density or current-sheet density given by Equation (4-7). This kind of representation for \bar{M} is amenable to mathematical analysis.

It has been assumed for purposes of analysis performed here that the magnetization \bar{M} is uniform (i.e., unidirectional) and of constant magnitude throughout the volume of the magnet. This assumption appears very reasonable for the rare-earth-cobalt magnets. The nonuniformity is partly introduced during the process of compacting the powder alloy, and therefore the extent of nonuniformity depends on the size of the magnets. However, this nonuniformity of magnetization throughout the volume of the magnet was quoted by the manufacturers to be less than 5 percent. With the assumption of uniform magnetization, it can be easily seen that the volume-current density becomes zero and the surface-current density assumes a constant magnitude over the entire magnet surface.

4.1 Analysis Procedure

Under the assumption of uniform magnetization, the equivalent surface currents enveloping the nonpolar surfaces of the permanent magnet form a current sheet of constant density. This current sheet can be considered as the summation of a series of electric circuits. Such electric circuits are present on the nonpolar surfaces of every magnet in the system.

With such a representation of the permanent magnet, calculation of forces basically involves the use of Ampere's Force Law [1], which predicts the force between two electric circuits. The force is given by the integral of the double cross product:

$$\vec{F} = \mu_0 I I' \oint \oint \frac{\vec{ds} \times (\vec{ds}' \times \vec{r})}{4\pi r^3}, \quad (4-8)$$

where \vec{ds} and \vec{ds}' are the elemental arcs of the two electric circuits and \vec{r} is the radius vector between ds and ds' . I and I' are the currents flowing in the two circuits. Using a vector identity, Equation (4-8) can be written as:

$$\vec{F} = - \frac{\mu_0 I I'}{4\pi} \oint \oint \frac{\vec{r} (\vec{ds} \cdot \vec{ds}')}{r^3}. \quad (4-9)$$

μ_0 , which is the permeability of the surrounding space, is used in Equations (4-8) and (4-9) because the relative permeability for rare-earth-cobalt magnets, which is very nearly unity, has been assumed to be 1.0. It can be noticed from Equation (4-9) that, when \vec{ds} and \vec{ds}' are perpendicular to each other, no force exists between the two circuit elements.

The analysis procedure, therefore, involves a repeated use of Equation (4-8). The sign of each integral has to be properly considered. This approach to repulsion force calculation has been used earlier by Borcherts [8] and others [6, 9].

4.2 Analysis for Rectangular Parallelopiped-Shaped Magnets

Figure 4-1 shows two rectangular parallelopiped-shaped permanent magnets in a repulsive mode. The two magnets are assumed identical in shape in order to reduce the computational effort. The linear dimensions are nondimensionalized with respect to the width of the magnet. The two magnets are shown misaligned by an amount E in the X-direction. Study of misalignment is of importance in bearing applications because of the associated changes in forces and stiffness coefficients which determine the stability of the suspension system. In order that they produce repulsion, the directions of magnetization \vec{M} of the two magnets are taken to be in $+Z$ and $-Z$ directions.

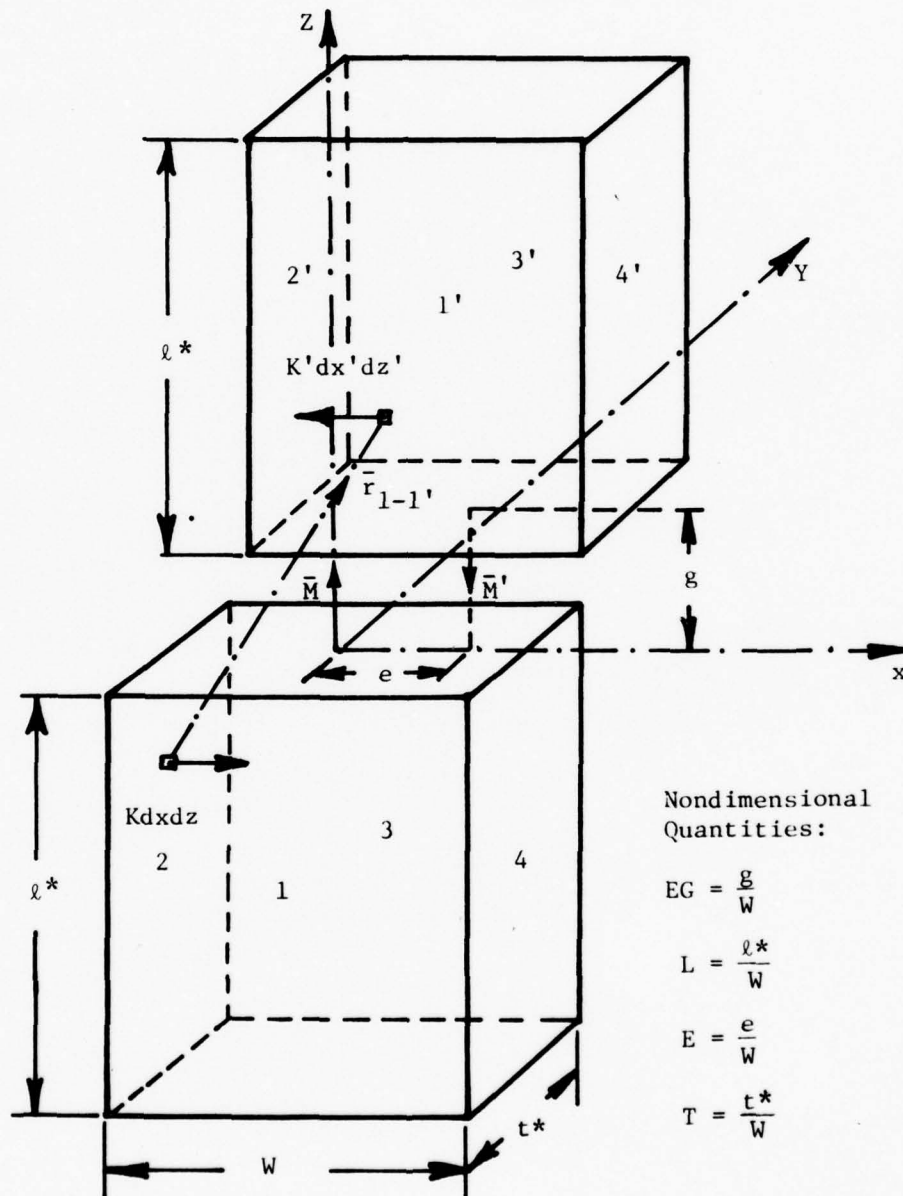


Fig. 4-1 Two Rectangular Parallelpiped-Shaped Magnets in Repulsive Mode

791263

The equivalent surface currents due to magnetization \bar{M}' of the upper magnet are shown as K' per unit surface area of the magnet. The direction of these currents is as shown in Figure 4-1. Similarly, the equivalent surface currents K per unit surface area of the lower magnet are as shown in the figure. The points on the upper magnet are denoted by (X', Y', Z') , while (X, Y, Z) represents points on the lower magnet.

If we now consider elements on the surfaces of each of the two magnets, the repulsive or attractive forces between any two elements can be calculated by using Ampere's Inverse Square Law, Equation (4-9).

Summing all the elemental forces over the faces 1 and 1', the repulsive force $\bar{F}_{1-1'}$ is obtained as:

$$\bar{F}_{1-1'} = \frac{\mu_0}{4\pi} KK'W^2 \int_{-L}^0 \int_{EG}^{L+EG} \int_{-\frac{1}{2}}^{\frac{1}{2}} \int_{-\frac{1}{2}+E}^{\frac{1}{2}+E} \frac{\bar{r}_{1-1'}}{r_{1-1'}^3} dx' dz' dy' dz \quad (4-10)$$

where $\bar{r}_{1-1'}$ is the position vector between the points (X, Y, Z) and (X', Y', Z') . Therefore, $\bar{r}_{1-1'}$ is given by:

$$\bar{r}_{1-1'} = (X'-X)\bar{U}_x + 0 \cdot \bar{U}_y + (Z'-Z)\bar{U}_z, \quad (4-11)$$

where \bar{U}_x , \bar{U}_y , and \bar{U}_z are the unit vectors in X-, Y-, and Z-directions, respectively. The magnitude of the vector $\bar{r}_{1-1'}$ is $r_{1-1'}$. In Equation (4-10), W^2 appears outside the integral sign because of nondimensionalization.

By symmetry, the repulsion force between faces 3 and 3' $\bar{F}_{3-3'}$ is equal to $\bar{F}_{1-1'}$. Similarly,

$$\bar{F}_{2-2'} = \frac{\mu_0}{4\pi} KK'W^2 \int_{-L}^0 \int_{EG}^{L+EG} \int_{-\frac{T}{2}}^{\frac{T}{2}} \int_{-\frac{T}{2}}^{\frac{T}{2}} \frac{\bar{r}_{2-2'}}{r_{2-2'}^3} dy' dz' dx' dz \quad (4-12)$$

and

$$\bar{r}_{2-2'} = E \bar{U}_x + (Y'-Y) \bar{U}_y + (Z'-Z) \bar{U}_z. \quad (4-13)$$

Again by symmetry, $\bar{F}_{2-2'} = \bar{F}_{4-4'}$. The attraction force $\bar{F}_{1-3'}$ is given by:

$$\bar{F}_{1-3'} = \frac{\mu_0}{4\pi} KK'W^2 \int_{-L}^0 \int_{EG}^{L+EG} \int_{-\frac{1}{2}}^{\frac{1}{2}} \int_{-\frac{1}{2}+E}^{\frac{1}{2}+E} \frac{\bar{r}_{1-3'}}{r_{1-3'}^3} dx' dx dz' dz, \quad (4-14)$$

and

$$\bar{r}_{1-3'} = (X'-X) \bar{U}_x + T \bar{U}_y + (Z'-Z) \bar{U}_z; \quad (4-15)$$

$\bar{F}_{1-3'}$ is equal to $\bar{F}_{1'-3}$ by symmetry.

The attraction force $\bar{F}_{2-4'}$ is given by

$$\bar{F}_{2-4'} = \frac{\mu_0}{4\pi} KK'W^2 \int_{-L}^0 \int_{EG}^{L+EG} \int_{-\frac{T}{2}}^{\frac{T}{2}} \int_{-\frac{T}{2}}^{\frac{T}{2}} \frac{\bar{r}_{2-4'}}{r_{2-4'}^3} dy' dy dz' dz \quad (4-16)$$

and

$$\bar{r}_{2-4'} = (1+E) \bar{U}_x + (Y'-Y) \bar{U}_y + (Z'-Z) \bar{U}_z. \quad (4-17)$$

The attraction force

$$\bar{F}_{2'-4} = \frac{\mu_0}{4\pi} KK'W^2 \int_{-L}^0 \int_{EG}^{L+EG} \int_{-\frac{T}{2}}^{\frac{T}{2}} \int_{-\frac{T}{2}}^{\frac{T}{2}} \frac{\bar{r}_{2'-4}}{r_{2'-4}^3} dy' dy dz' dz \quad (4-18)$$

where

$$\bar{r}_{2'-4} = (-1+E) \bar{U}_x + (Y'-Y) \bar{U}_y + (Z'-Z) \bar{U}_z. \quad (4-19)$$

A vector sum of Z-components of the above forces yields the normal component of the net repulsive force. The transverse component of the net repulsive force is obtained by summing vectorially the X-components of the above forces.

All the above quadruple integrals can be integrated analytically twice to reduce them to double integrals in Z and Z' . The normal component of the total repulsive force F_z can be written as

$$F_z = \frac{\mu_0}{4\pi} KK'W^2 \int_{-L}^0 \int_{EG}^{L+EG} f_z(E, T, Z'-Z) dZ' dZ \quad (4-20)$$

The variables Z and Z' in Equation (4-20) can be transformed to ξ and η by

$$\xi = Z' - Z$$

$$\eta = Z' + Z.$$

Since the integrand in Equation (4-20) is only a function of $(Z'-Z)$, integration with respect to η after transformation becomes trivial and, therefore, the double integral of Equation (4-20) can be reduced to a single integral given by

$$F_z = \frac{\mu_0}{4\pi} KK'W^2 \left\{ \int_{EG}^{L+EG} (\xi - EG) \cdot f_z(E, T, \xi) d\xi + \int_{L+EG}^{2L+EG} (2L+EG-\xi) f_z(E, T, \xi) d\xi \right\}. \quad (4-21)$$

Similarly, the transverse component of the total repulsive force F_x is given by

$$F_x = \frac{\mu_0}{4\pi} KK'W^2 \left\{ \int_{EG}^{L+EG} (\xi - EG) f_x(E, T, \xi) d\xi + \int_{L+EG}^{2L+EG} (2L+EG-\xi) f_x(E, T, \xi) d\xi \right\}. \quad (4-22)$$

The functions f_z and f_x are given by the following:

$$f_z = 2 \left\{ \frac{[(-1+E)^2 + \xi^2]^{1/2}}{\xi} - \xi \frac{[(-1+E)^2 + T^2 + \xi^2]^{1/2}}{T^2 + \xi^2} \right\}$$

$$\begin{aligned}
& + 2\xi \frac{[E^2 + T^2 + \xi^2]^{\frac{1}{2}}}{T^2 + \xi^2} - \frac{2[E^2 + \xi^2]^{\frac{1}{2}}}{\xi} \\
& - \frac{\xi[(1+E)^2 + T^2 + \xi^2]^{\frac{1}{2}}}{T^2 + \xi^2} + \frac{[(1+E)^2 + \xi^2]^{\frac{1}{2}}}{\xi} \\
& + \frac{\xi}{[(1+E)^2 + \xi^2]^{\frac{1}{2}}} - \frac{2\xi}{[E^2 + \xi^2]^{\frac{1}{2}}} \\
& + \frac{2\xi[E^2 + T^2 + \xi^2]^{\frac{1}{2}}}{E^2 + \xi^2} - \frac{\xi[(1+E)^2 + T^2 + \xi^2]^{\frac{1}{2}}}{(1+E)^2 + \xi^2} \\
& + \frac{\xi}{[(-1+E)^2 + \xi^2]^{\frac{1}{2}}} - \frac{\xi[(-1+E)^2 + T^2 + \xi^2]^{\frac{1}{2}}}{(-1+E)^2 + \xi^2} \Big\} \\
f_x = 2 & \left\{ 2 \ln \left[\frac{E}{\xi} + \left(\frac{E^2}{\xi^2} + 1 \right)^{\frac{1}{2}} \right] - 2 \ln \left[\frac{E}{\sqrt{T^2 + \xi^2}} + \left(\frac{E^2}{T^2 + \xi^2} + 1 \right)^{\frac{1}{2}} \right] \right. \\
& + \ln \left[\frac{1+E}{\sqrt{T^2 + \xi^2}} + \left(\frac{(1+E)^2}{T^2 + \xi^2} + 1 \right)^{\frac{1}{2}} \right] - \ln \left[\frac{1+E}{\xi} + \left(\frac{(1+E)^2}{\xi^2} + 1 \right)^{\frac{1}{2}} \right] \\
& + \ln \left[\frac{-1+E}{\sqrt{T^2 + \xi^2}} + \left(\frac{(-1+E)^2}{T^2 + \xi^2} + 1 \right)^{\frac{1}{2}} \right] - \ln \left[\frac{-1+E}{\xi} + \left(\frac{(-1+E)^2}{\xi^2} + 1 \right)^{\frac{1}{2}} \right] \\
& + \frac{1+E}{[(1+E)^2 + \xi^2]^{\frac{1}{2}}} - \frac{2E}{[E^2 + \xi^2]^{\frac{1}{2}}} \\
& + \frac{2E[E^2 + T^2 + \xi^2]^{\frac{1}{2}}}{E^2 + \xi^2} - \frac{(1+E)[(1+E)^2 + T^2 + \xi^2]^{\frac{1}{2}}}{(1+E)^2 + \xi^2} \\
& \left. - \frac{(-1+E)[(-1+E)^2 + T^2 + \xi^2]^{\frac{1}{2}}}{(-1+E)^2 + \xi^2} + \frac{(-1+E)}{[(-1+E)^2 + \xi^2]^{\frac{1}{2}}} \right\}
\end{aligned}$$

The above integrals for the normal and transverse forces were evaluated numerically. The details of the numerical evaluation will be given in a later section.

4.3 Analysis for Cylinder-Shaped Magnets

Figure 4-2 shows two cylinder-shaped, permanent magnets in a repulsive mode. The two magnets are assumed to have identical dimensions. All the linear dimensions are nondimensionalized with respect to the radius R . The magnetization vectors \bar{M} and \bar{M}' are in the $+Z$ and $-Z$ directions as shown in the figure. Equivalent surface currents K and K' are also shown in the figure. As in the previous section, (X, Y, Z) and (X', Y', Z') represent points on the lower and upper magnets, respectively.

Considering elements on the surfaces of each of the magnets, the repulsive force between any two elements can be calculated by using Ampere's Law, Equation (4-9). A summation of these elemental forces gives the total repulsive force:

$$\bar{F} = \frac{\mu_0}{4\pi} KK'R^2 \int_{-L}^0 \int_{EG}^{L+EG} \int_0^{2\pi} \int_0^{2\pi} \frac{r}{3} \cos(\phi - \phi') d\phi' d\phi dz' dz \quad (4-23)$$

and

$$\bar{r} = (E + \cos\phi' - \cos\phi)\bar{U}_x + (\sin\phi' - \sin\phi)\bar{U}_y + (Z' - Z)\bar{U}_z. \quad (4-24)$$

The X -component of \bar{F} gives the transverse force while the Z -component yields the normal force. By symmetry, the Y -component is zero. The above integral can be integrated analytically twice with respect to Z and Z' , yielding:

$$F_z = \frac{\mu_0}{4\pi} KK'R^2 \int_0^{2\pi} \int_0^{2\pi} f_z(E, L, EG, P, Q) d\phi' d\phi, \quad (4-25)$$

where

$$f_z = \frac{Q}{2} \ln \left[\frac{\left[\frac{[P+(L+EG)^2]^{\frac{1}{2}} + (L+EG)}{[P+(L+EG)^2]^{\frac{1}{2}} - (L+EG)} \right]^2}{\frac{[P+EG^2]^{\frac{1}{2}}+EG}{[P+EG^2]^{\frac{1}{2}}-EG} \left/ \frac{[P+(2L+EG)^2]^{\frac{1}{2}} + (2L+EG)}{[P+(2L+EG)^2]^{\frac{1}{2}} - (2L+EG)} \right.} \right]$$

$$Q = \cos(\phi - \phi')$$

$$P = E^2 + 4E \sin \frac{\phi + \phi'}{2} \sin \frac{\phi - \phi'}{2} + 2 [1 - \cos(\phi - \phi')]$$

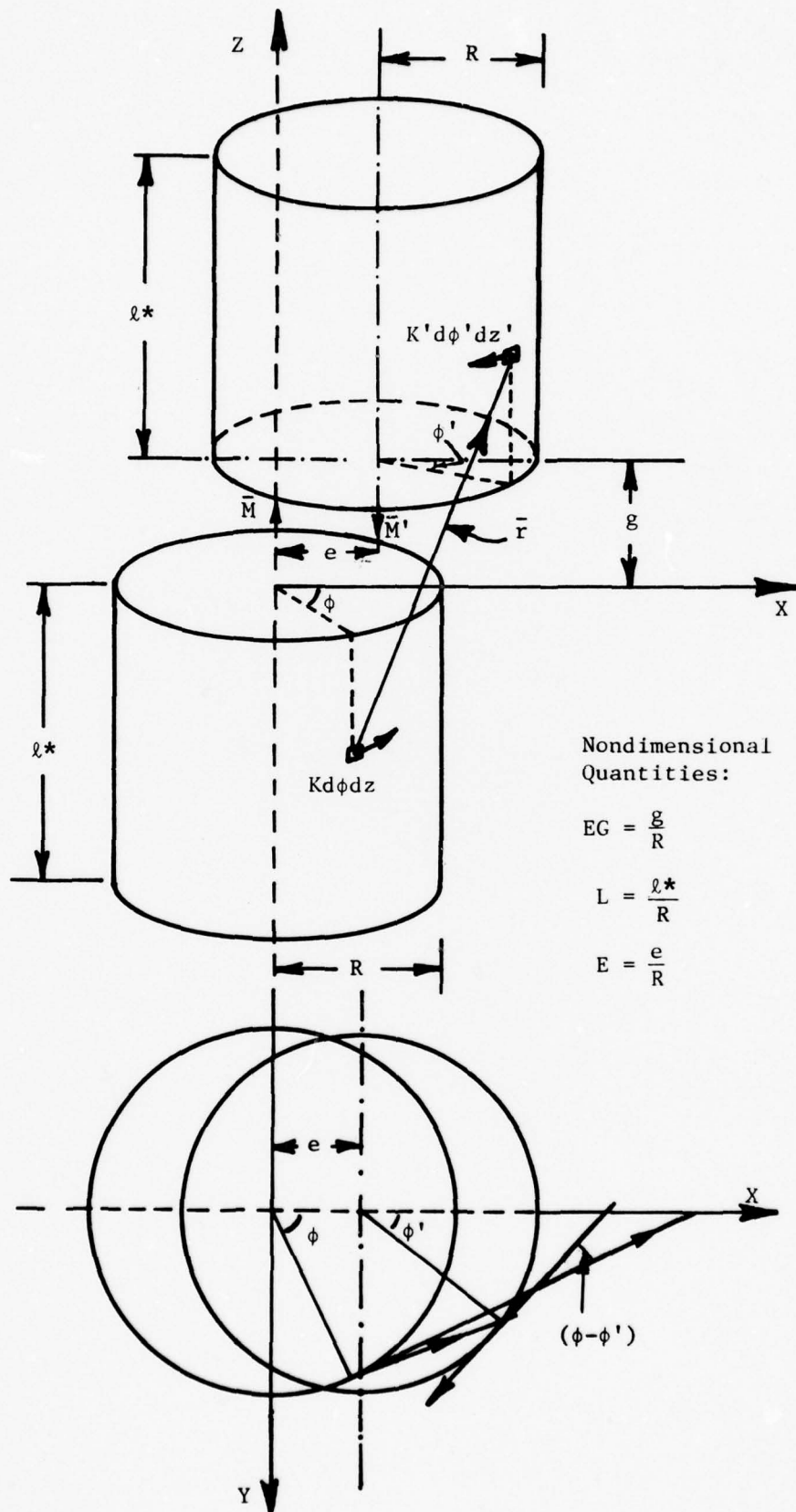


Fig. 4-2 Two Cylinder-Shaped Magnets in Repulsive Mode

and

$$F_x = \frac{\mu_0}{4\pi} KK'R^2 \int_0^{2\pi} d\phi \int_0^{2\pi} f_x(E, L, EG, P, A) d\phi' \quad (4-26)$$

where

$$f_x = -\frac{A \cdot EG}{P} \left[\frac{(L+EG)}{[P+(L+EG)^2]^{\frac{1}{2}}} - \frac{EG}{[P+EG^2]^{\frac{1}{2}}} \right] - \frac{A}{[P+(L+G)^2]^{\frac{1}{2}}} + \frac{A}{[P+EG^2]^{\frac{1}{2}}}$$

$$A = \left[E + 2 \sin \frac{\phi+\phi'}{2} \sin \frac{\phi-\phi'}{2} \right] \cos(\phi-\phi')$$

$$P = E^2 + 4E \sin \frac{\phi+\phi'}{2} \sin \frac{\phi-\phi'}{2} + 2 [1 - \cos(\phi-\phi')]$$

During the process of integration, when $E=0$, the parameter P can take on a value of zero. Under these conditions, f_z and f_x as defined above will be infinite. In order to overcome this problem, the above integrals were evaluated separately for $P=0$ and are given by:

$$f_z = Q \ln \left[\frac{(L+EG)^2}{EG(2L+EG)} \right], \quad (4-27)$$

and

$$f_x = \frac{AL^2}{EG(L+EG)(2L+EG)}. \quad (4-28)$$

By transforming the variables ϕ and ϕ' to \hat{X} and \hat{Y} by

$$\left. \begin{aligned} \hat{X} &= \frac{\phi+\phi'}{4} \\ \hat{Y} &= \frac{\phi-\phi'}{4} \end{aligned} \right\}, \quad (4-29)$$

the integrals for F_z and F_x have been transformed to

$$F_z = \frac{\mu_0}{4\pi} KK'R^2 \cdot 8 \int_0^{\pi/2} d\hat{Y} \int_{\hat{Y}}^{\pi-\hat{Y}} \left[f_z(P) + f_z(P^*) \right] d\hat{X} \quad (4-30)$$

where

$$P^* = E^2 - 4E \sin 2\hat{X} \sin 2\hat{Y} + 4 \sin^2 2\hat{Y}$$

P, Q, and f_z are as defined earlier, but \hat{X} and \hat{Y} substituted in place of ϕ and ϕ' using Equation (4-29).

Similarly,

$$F_x = \frac{\mu_0}{4\pi} KK'R^2 .8 \int_0^{\pi/2} d\hat{Y} \int_{\hat{Y}}^{\pi-\hat{Y}} [f_x(P) + f_x(P^*)] d\hat{X}$$

where

$$P^* = E^2 - 4E \sin 2\hat{X} \sin 2\hat{Y} + 4 \sin^2 2\hat{Y}.$$

P, A, and f_x are as defined earlier.

Computational details for the above integrals will be given in a later section.

4.4 Results and Discussion for Rectangular Parallelopiped-Shaped Magnets

The integrals for the normal and transverse forces given by Equations (4-21) and (4-22) were evaluated numerically by using a 10-point Gaussian quadrature. A computer program was written in order to perform this numerical evaluation. The values computed were the nondimensional values of the normal and transverse forces $\frac{F_z}{\frac{\mu_0}{4\pi} KK'W^2}$ and $\frac{F_x}{\frac{\mu_0}{4\pi} KK'W^2}$, respectively.

The computer program was run on the General Electric Mark IV computing facilities available at MTI. The numerical technique used (i.e., the 10-point Gaussian quadrature) was accurate to within 0.01 percent.

Using the above computer program, a systematic, parametric study was performed. The parameters studied were the eccentricity E, the gap EG, the thickness T, and the length L. All these parameters have been nondimensionalized with respect to the width (W) of the magnet.

The calculated normal and transverse forces are plotted against the operating parameters E and EG. $T=1.0$ and 5.0 and $L=.2$, $.5$ and 1.0 are studied which represent a practical range of these geometric parameters. Figures 4-3 through 4-26 show the results for the case of two rectangular parallelepiped-shaped magnets.

Figure 4-3 shows the normal component of the repulsive force plotted against the eccentricity E. The positive value of Z-force is repulsion and the negative value is attraction. For any constant value of gap EG, the force is seen to decrease with eccentricity, as expected. Also, for values of E greater than about 0.85, the force changes sign. This is because, at large eccentricities, faces of opposite polarity come closer to each other than the distance between faces of like polarity. This attraction force at large eccentricities, however, becomes insignificant at large values of gap.

Figures 4-4 and 4-5 show Z-force (the normal component of the repulsive force) plotted against the eccentricity E. Figures 4-3, 4-4, and 4-5 have the same value of T, but increasing values of L; therefore, the cross-sectional area of the magnets, remains the same. It can be seen from these figures that the Z-force (for example at $EG=0$) does not increase proportionately with increase in length. If we consider that a longer magnet is made up from stacking shorter magnets one on top of the other, the mutual demagnetizing effects are evident. Therefore, the Z-force increases with increase in L, but less than proportionately.

Figures 4-6, 4-7, and 4-8 show plots of Z-force versus eccentricity at $T=5.0$ and various values of L. If we compare figures 4-6, 4-7, and 4-8 with Figures 4-3, 4-4, and 4-5, the effect of increasing the thickness can be observed. Increasing the thickness while keeping the length the same is equivalent to stacking the magnets one by the side of another. The mutual interaction and demagnetizing effects are clearly evident. For this reason, the Z-force increases with T, but less than proportionately. By comparing the results shown in Figures 4-3 through 4-8, it can be seen that, for the same volume of the magnet, increasing the thickness increases Z-force more than increasing the length. This is because the effective gap for a longer magnet is larger than that for a magnet with higher value of T.

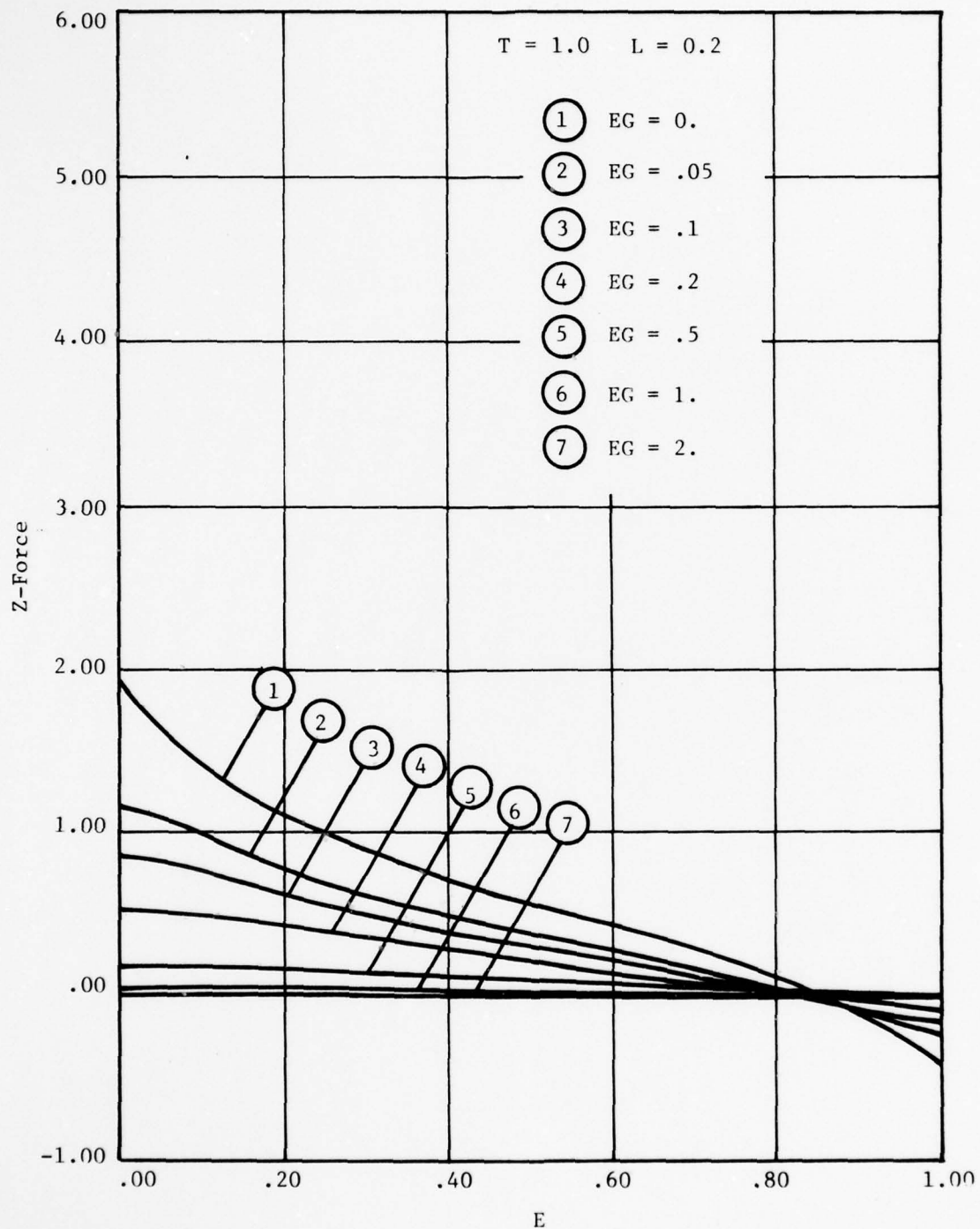


Fig. 4-3 Z-Force Versus E ($T = 1.0$, $L = 0.2$)

791265

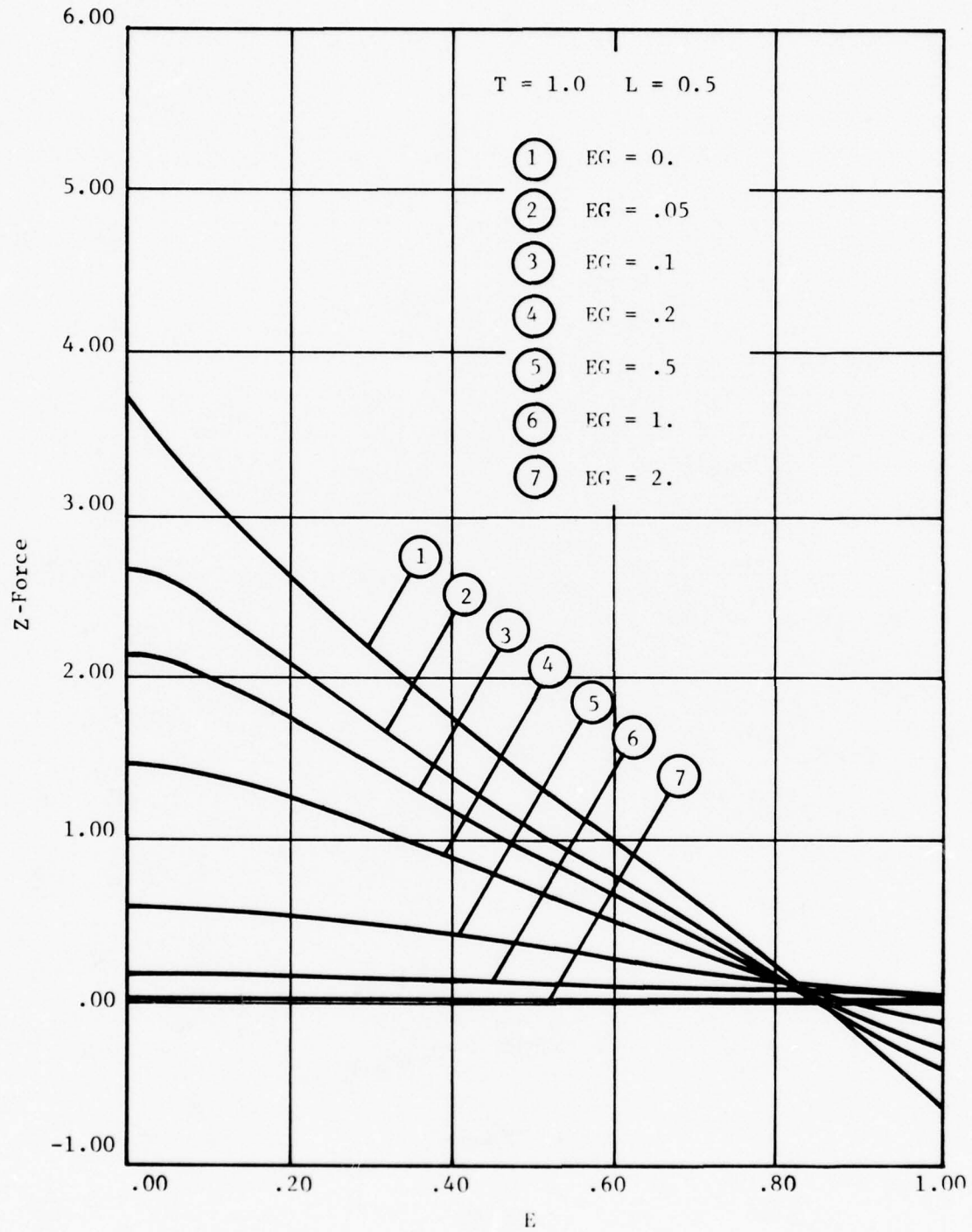


Fig. 4-4 Z-Force Versus E ($T = 1.0$, $L = 0.5$)

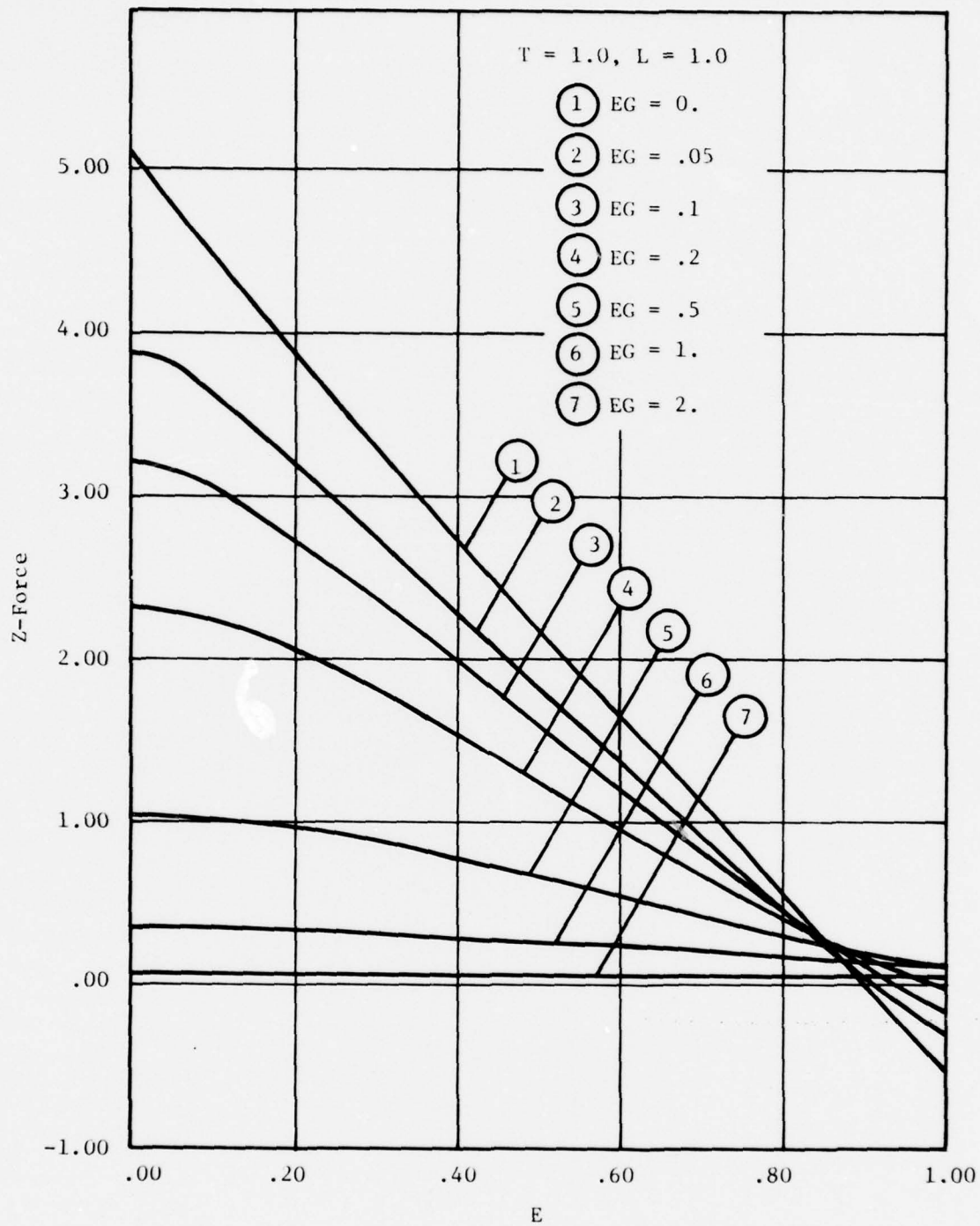


Fig. 4-5 Z-Force Versus E ($T = 1.0, L = 1.0$)

791267

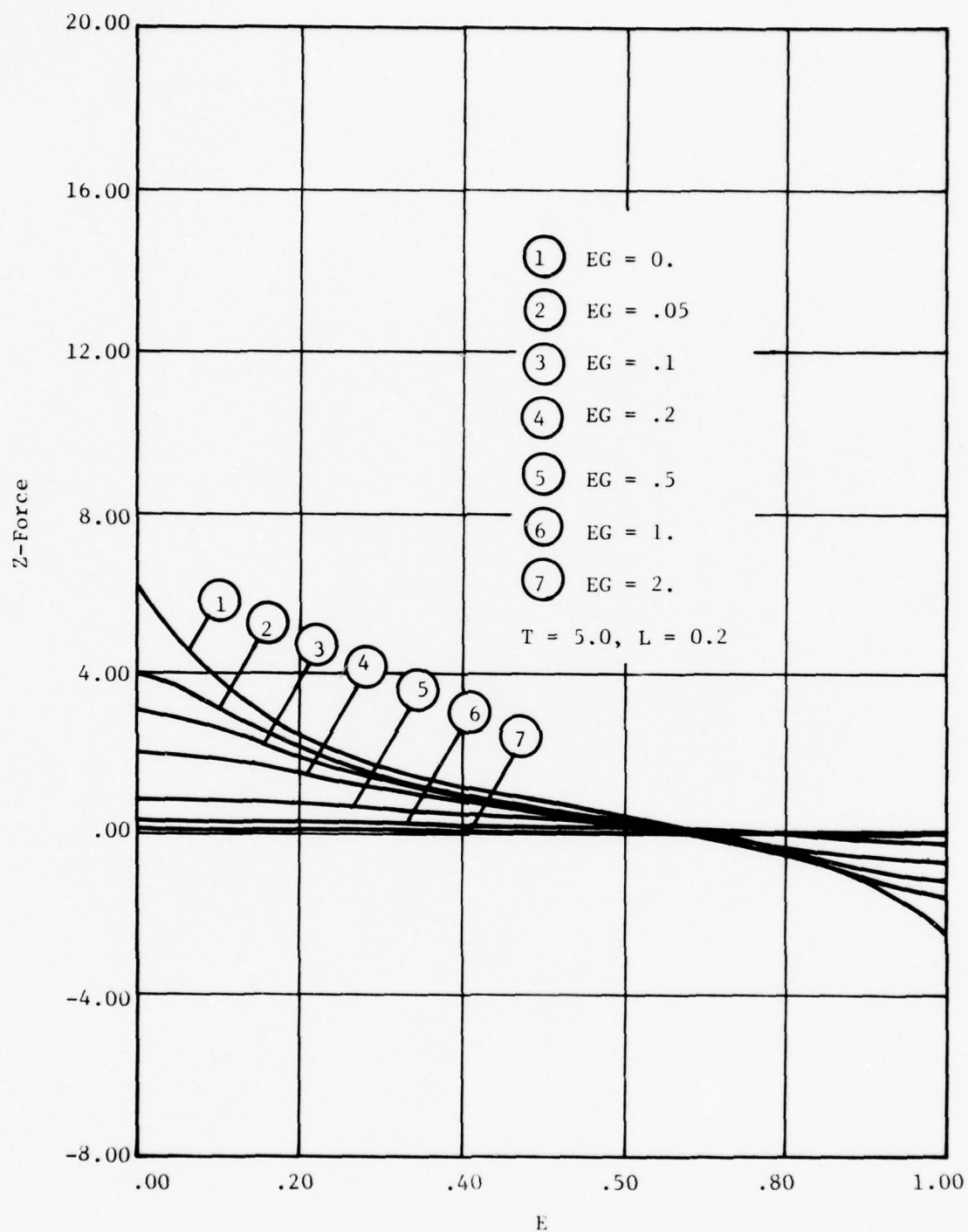


Fig. 4-6 Z-Force Versus E ($T = 5.0, L = 0.2$)

791268

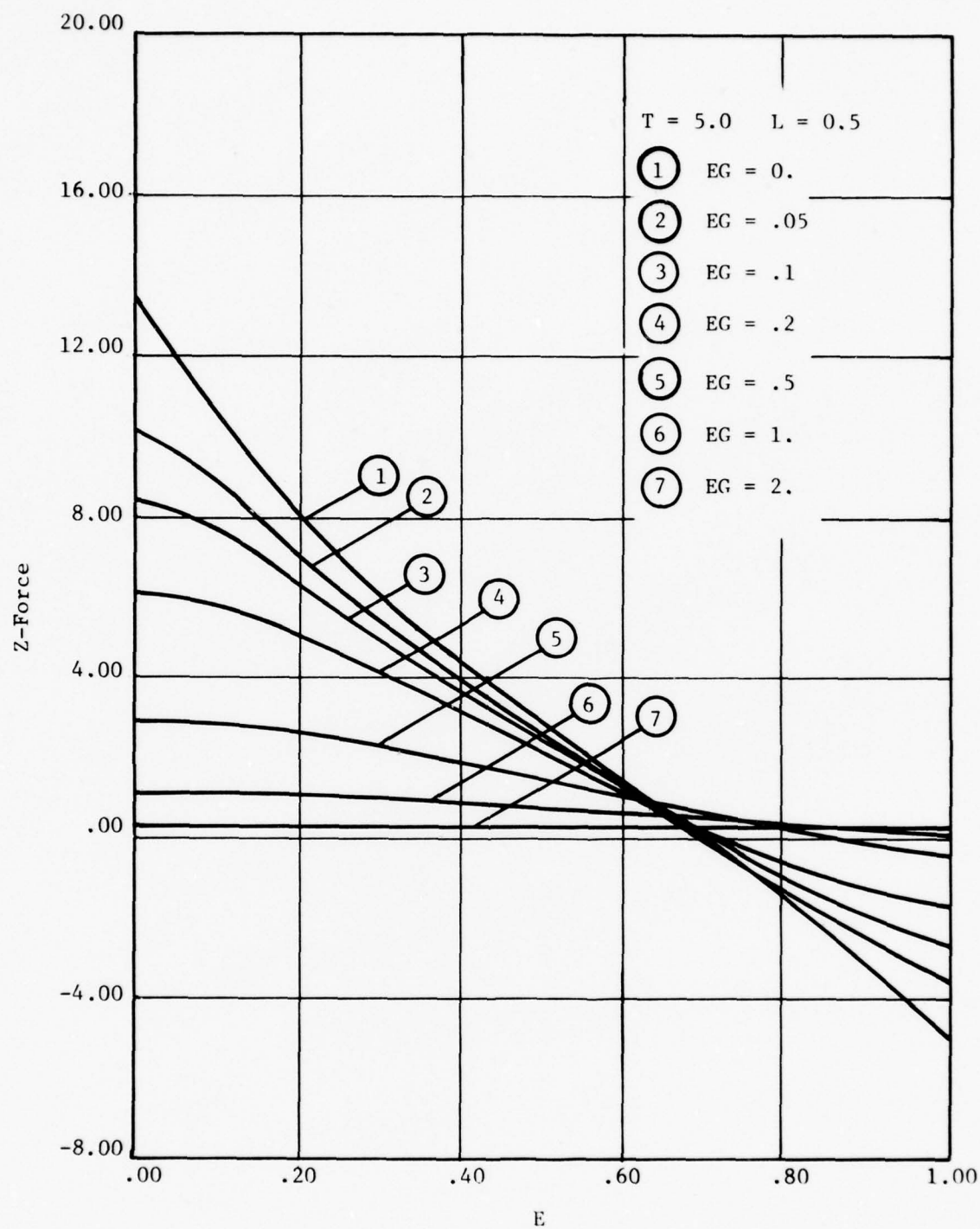


Fig. 4-7 Z-Force Versus E ($T = 5.0$, $L = 0.5$)

791269

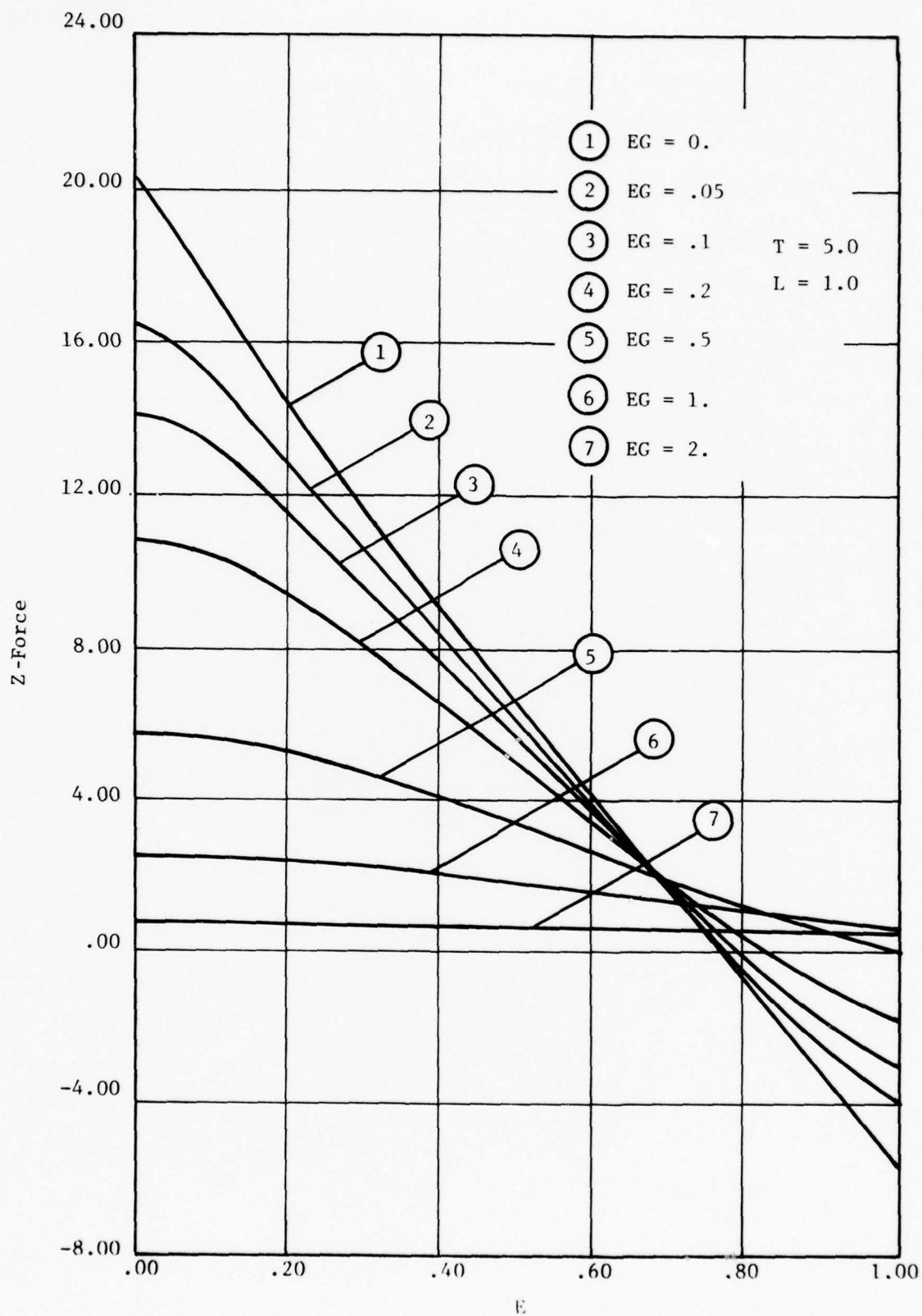


Fig. 4-8 Z-Force Versus E (T = 5.0, L = 1.0)

The transverse component of the repulsive force versus eccentricity E at various values of the gap is shown in Figure 4-9. The transverse force is zero at $E = 0$ because of symmetry. But, interestingly enough, the transverse force reaches a maximum and then starts decreasing with further increase in eccentricity. The transverse component of the repulsive force depends on two quantities: the angle (θ) between the total repulsive force and the X-axis, and the distance (r). r increases with eccentricity while θ decreases. The repulsive force is inversely proportional to the square of the distance r , whereas the transverse component is proportional to the cosine of the angle θ . Because of these two competing quantities, the X-force reaches a maximum at a certain value of E and then starts decreasing. The value of E for which the X-force is a maximum depends on the gap, and this value of E increases with the gap, as can be expected.

At small values of eccentricity E , the slope of the repulsive X-force versus curve E is positive. In this region, the equilibrium is unstable. However, it can be seen from Figures 4-9, 4-10, and 4-11 that, at far enough eccentricities, the equilibrium can indeed be stable. Although a stable equilibrium can be established in the X- and Z-directions, instability cannot be avoided in the Y-direction (perpendicular to X-Z plane), simultaneously.

Figures 4-10 and 4-11 show plots of X-force versus eccentricity at various values of gap for $T=1.0$ and $L=.5$ and 1.0 , respectively. Figures 4-12, 4-13, and 4-14 show similar plots but for $T=5.0$. An observation of these figures reveals the following: (1) at a given value of T , an increase in length produces transverse forces which increase more than proportionately to begin with; (2) increase in the thickness T produces a more than proportionate increase in the transverse force. These observations can be rationalized by considering that the larger magnets are made by stacking smaller magnets. It can then be easily seen that the mutual interaction of smaller magnets enhances the transverse forces under some conditions.

Figures 4-15 through 4-20 show plots of Z-force versus the gap E_G at various values of the eccentricity E and at different values of L and T . The positive values represent repulsion, while negative values represent attraction. The Z-force goes to zero at large values of gap, as expected.

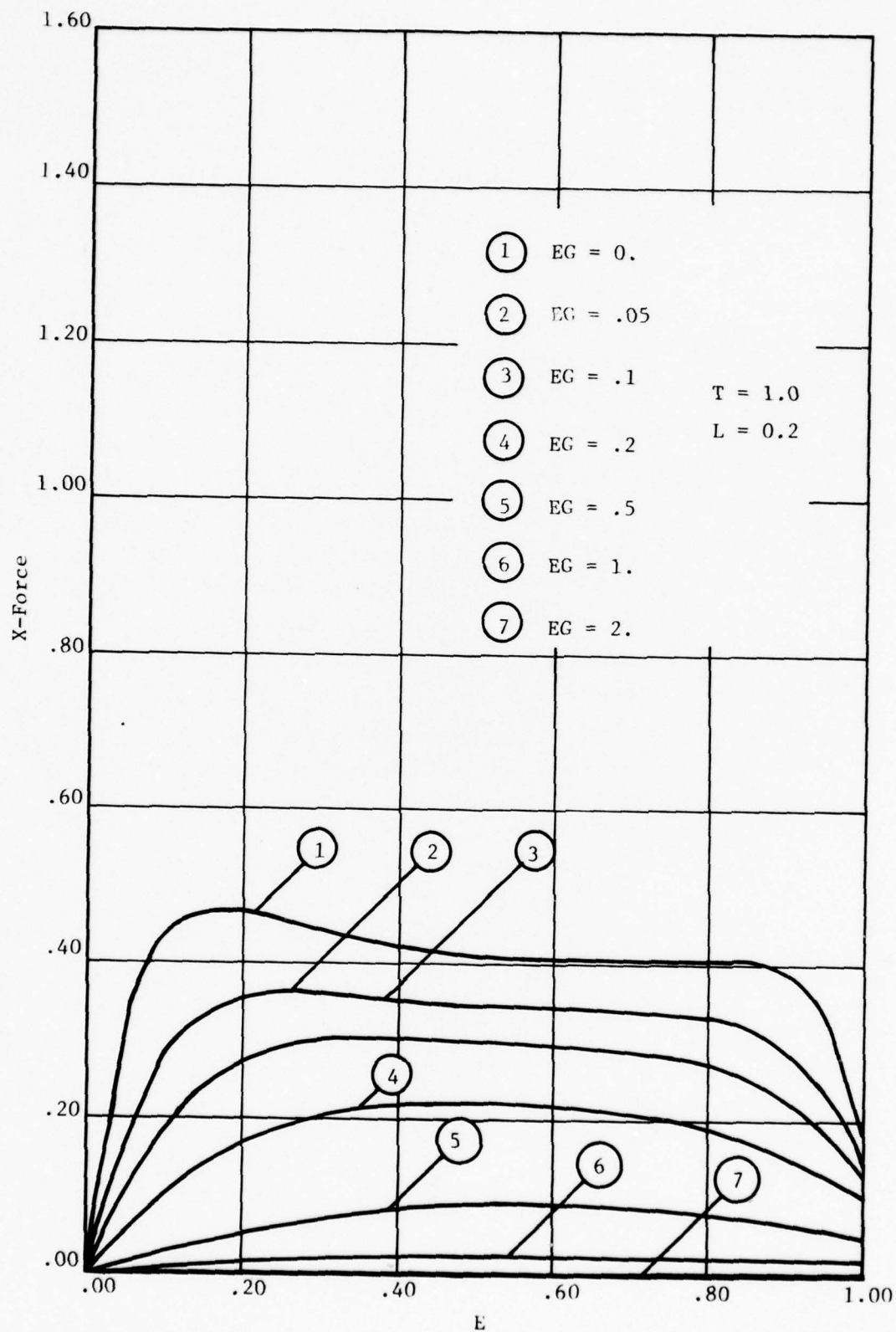


Fig. 4-9 X-Force Versus E ($T = 1.0$, $L = 0.2$)

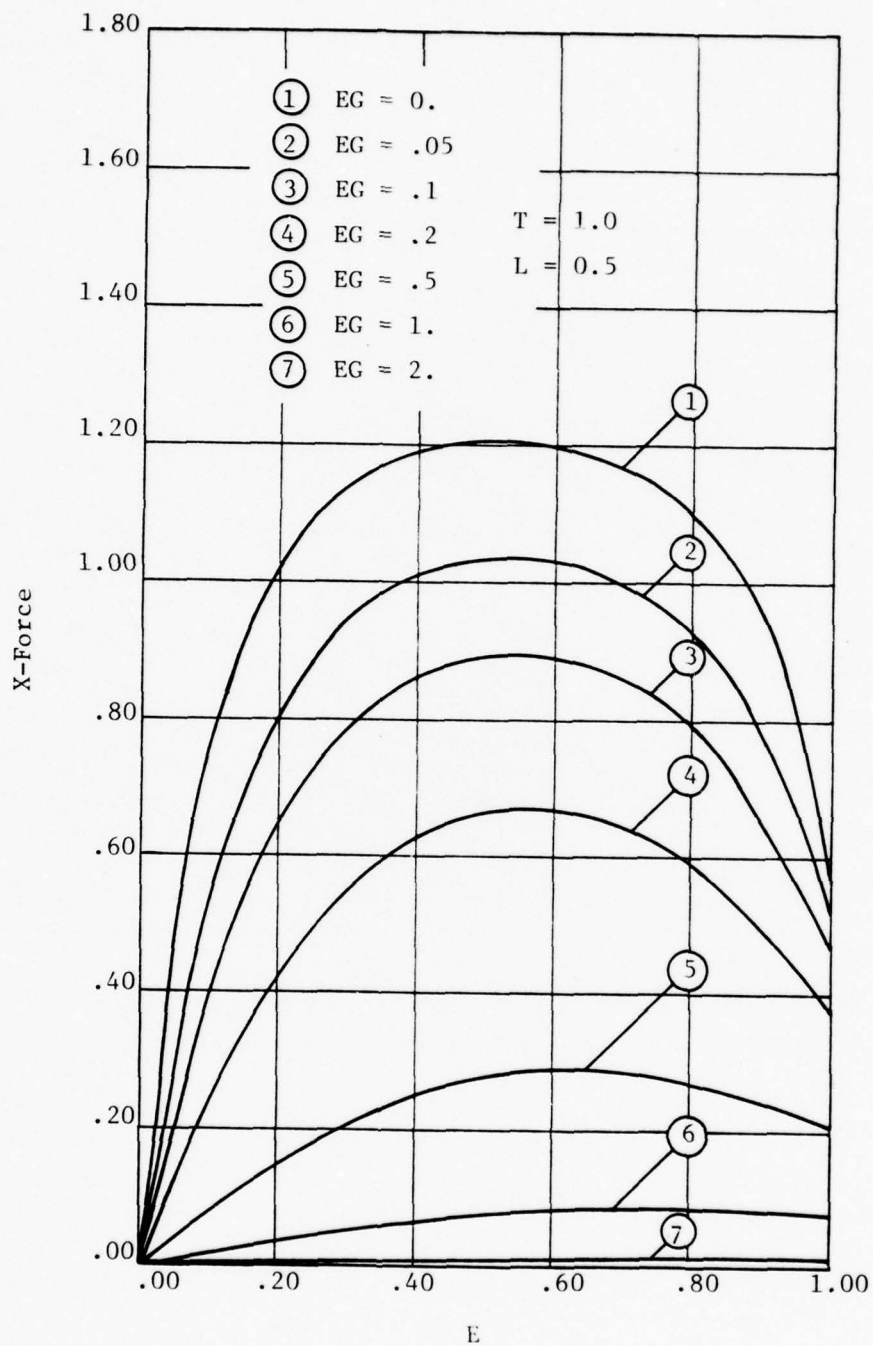


Fig. 4-10 X-Force Versus E ($T = 1.0$, $L = 0.5$)

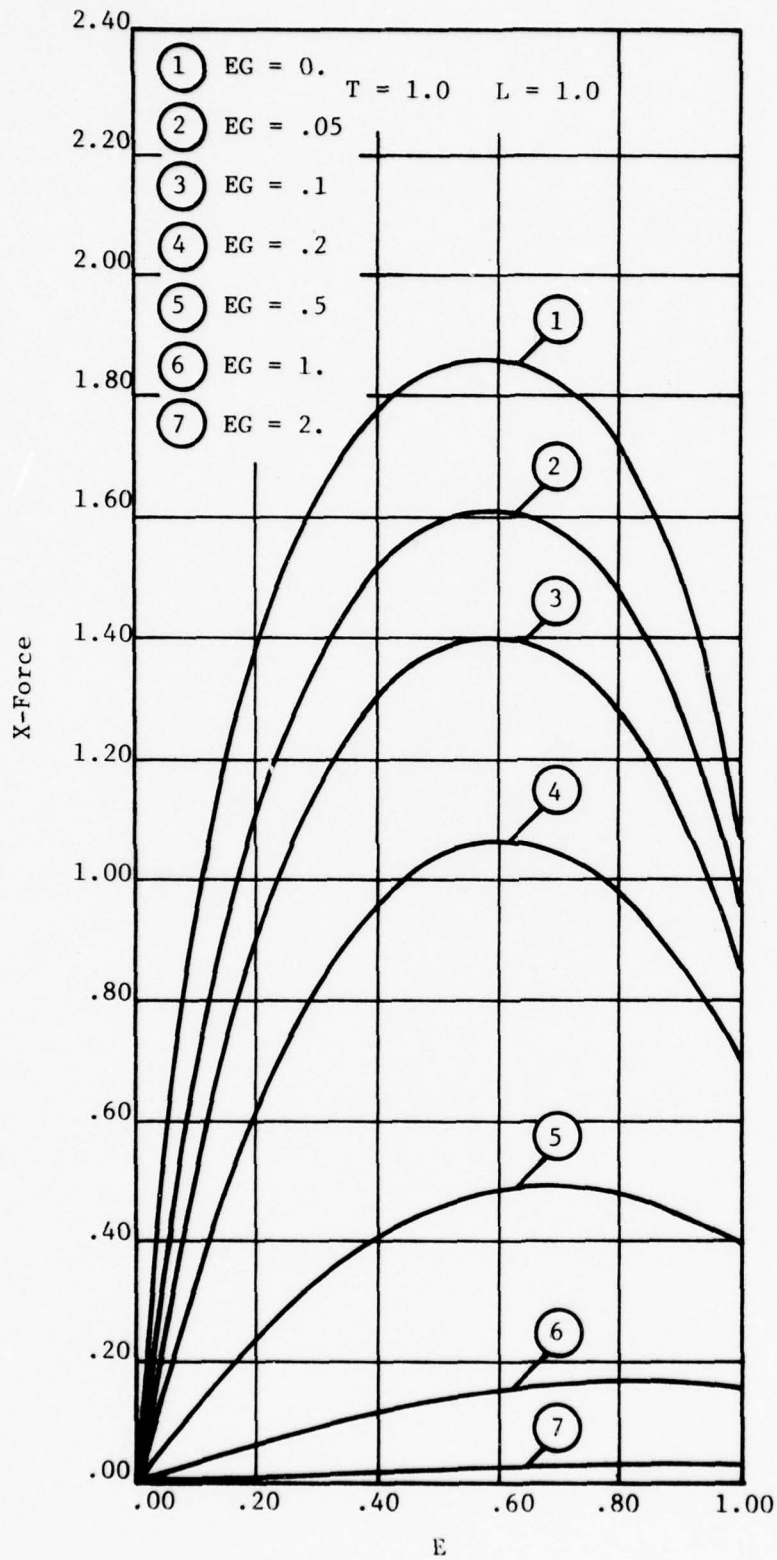


Fig. 4-11 X-Force Versus E ($T = 1.0$, $L = 1.0$)

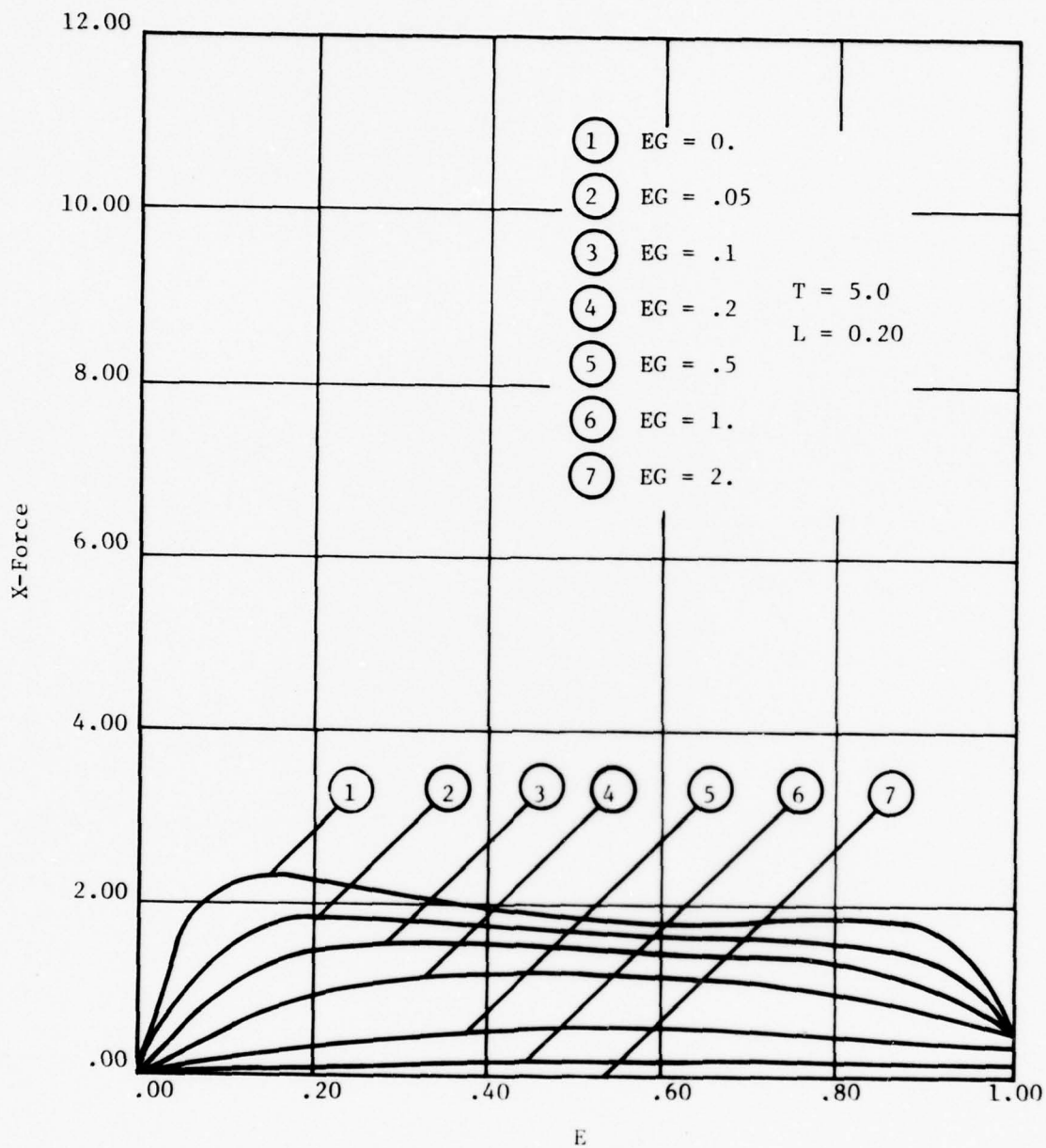


Fig. 4-12 X-Force Versus E ($T = 5.0$, $L = 0.2$)

791274

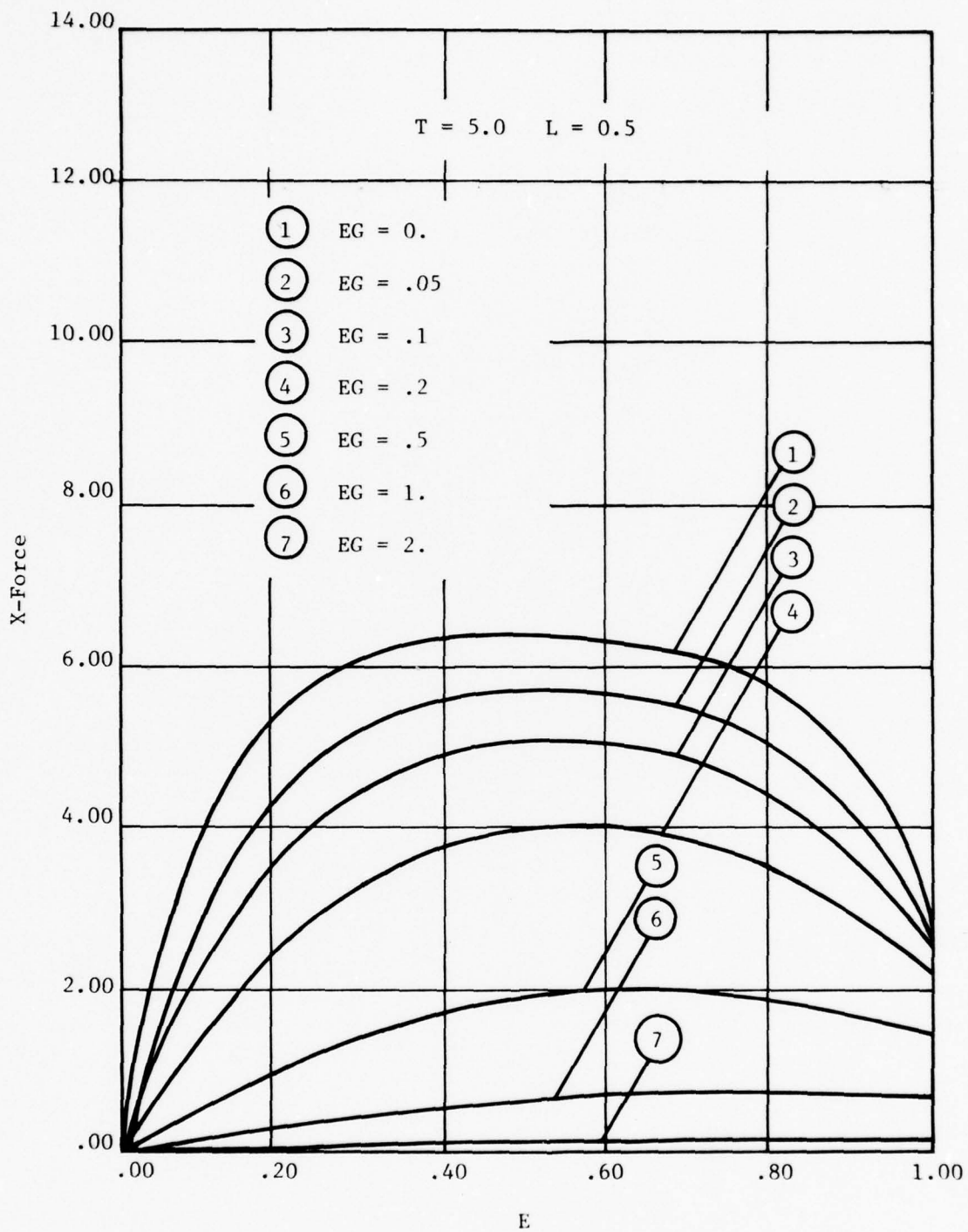


Fig. 4-13 X-Force Versus E ($T = 5.0$, $L = 0.5$)

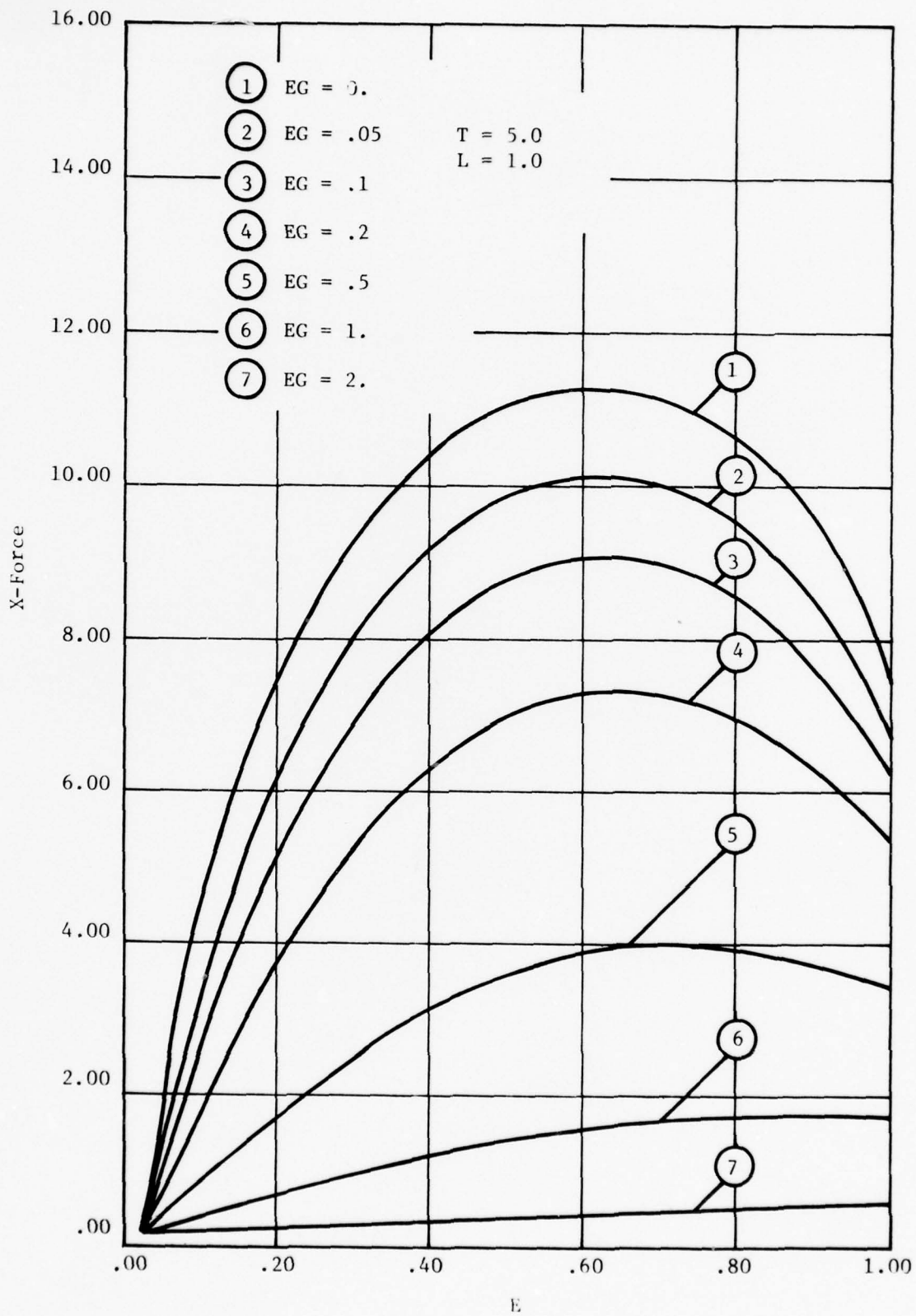


Fig. 4-14 X-Force Versus E (T = 5.0, L = 1.0)

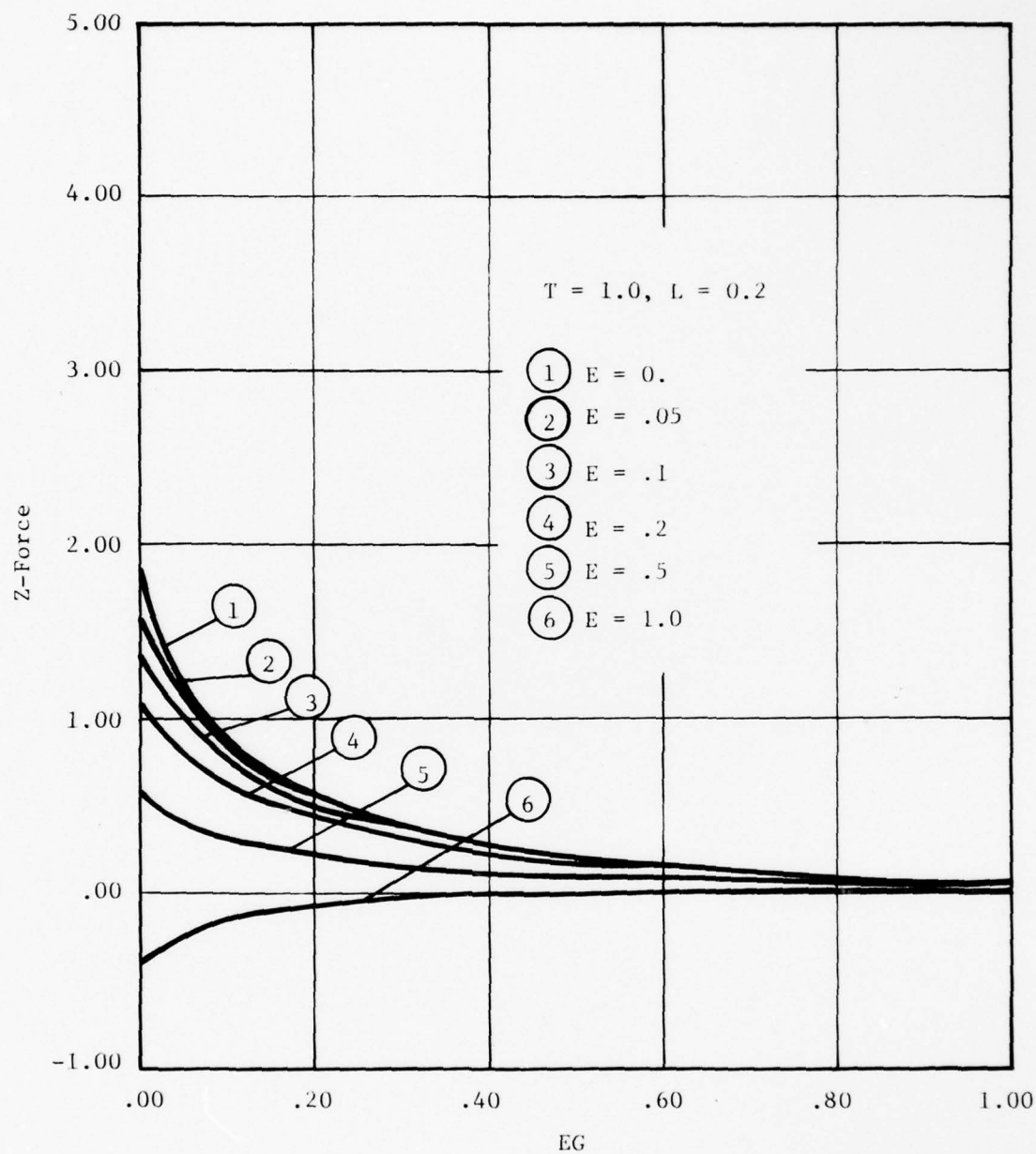


Fig. 4-15 Z-Force Versus EG ($T = 1.0, L = 0.2$)

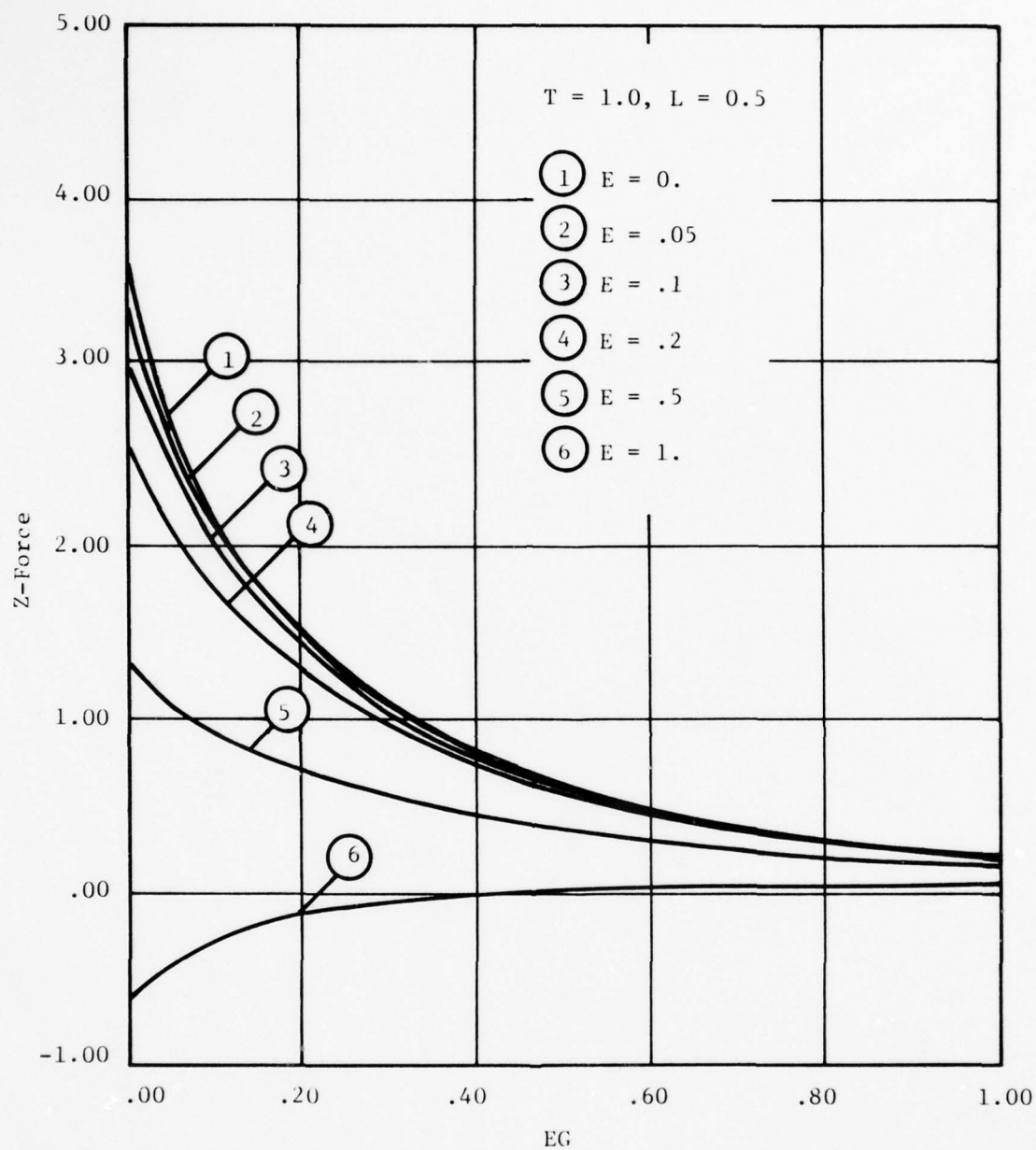


Fig. 4-16 Z-Force Versus EG ($T = 1.0, L = 0.5$)

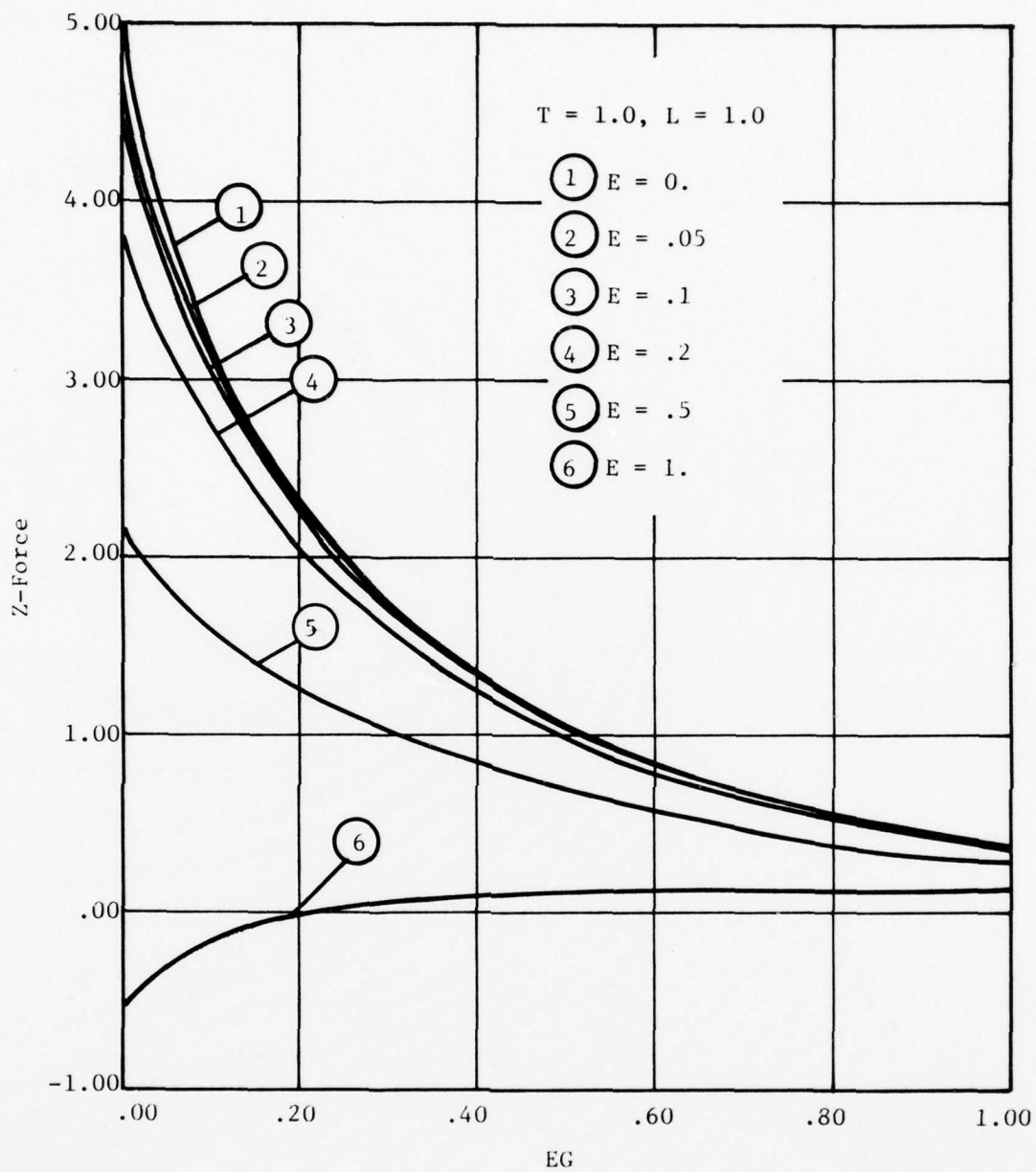


Fig. 4-17 Z-Force Versus EG ($T = 1.0$, $L = 1.0$)

791279

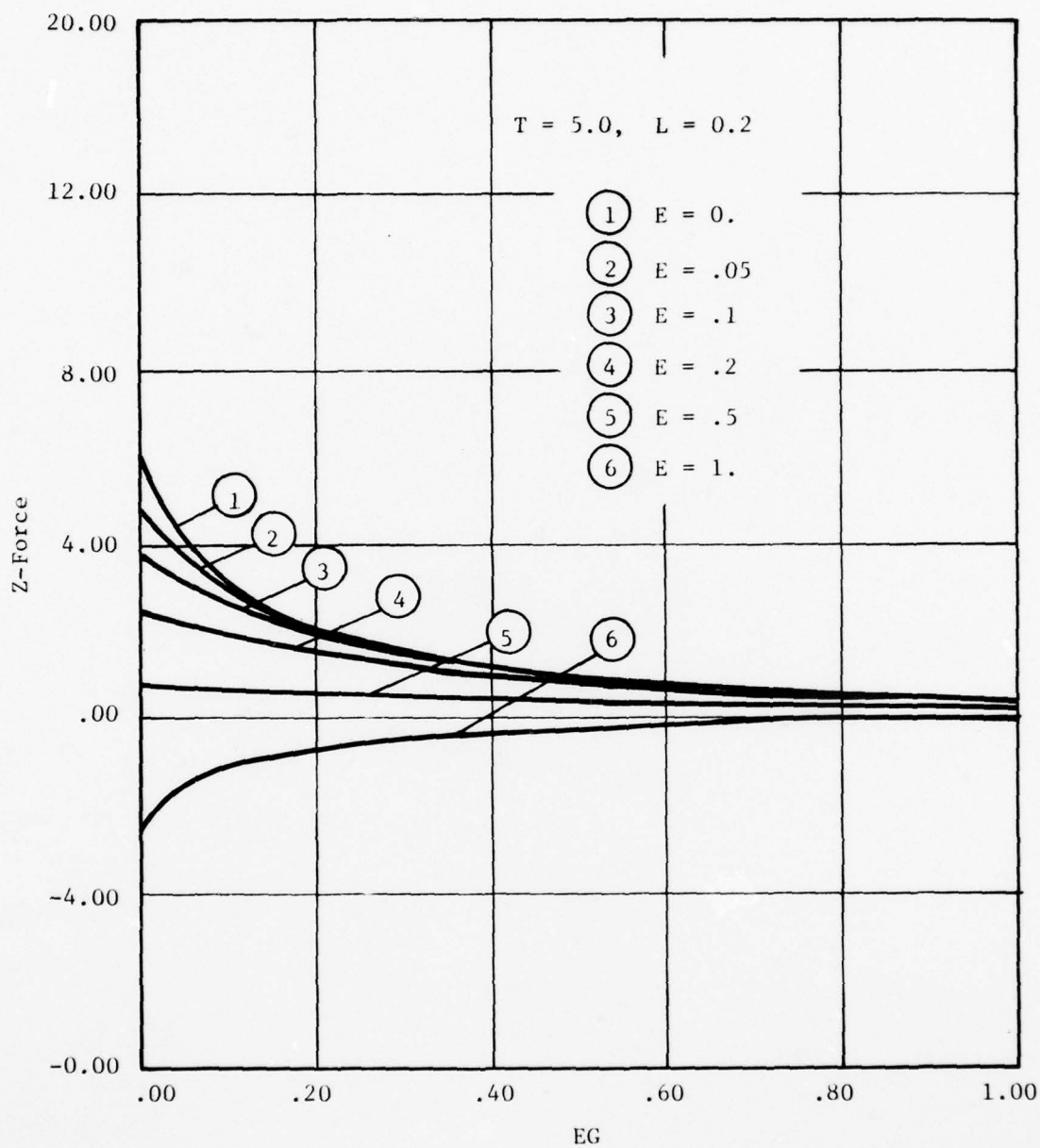


Fig. 4-18 Z-Force Versus EG ($T = 5.0, L = 0.2$)

791280

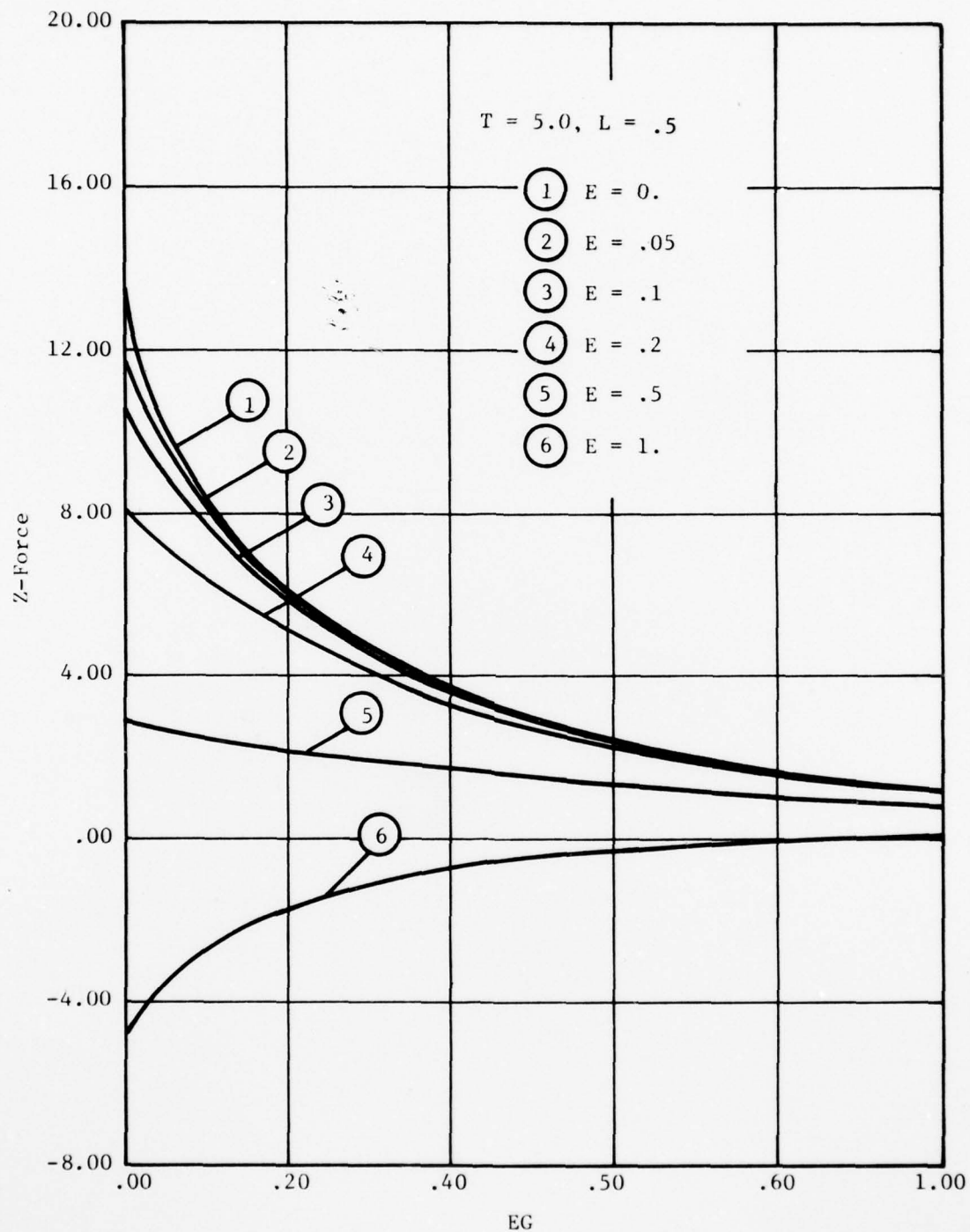


Fig. 4-19 Z-Force Versus EG ($T = 5.0, L = 0.5$)

791281

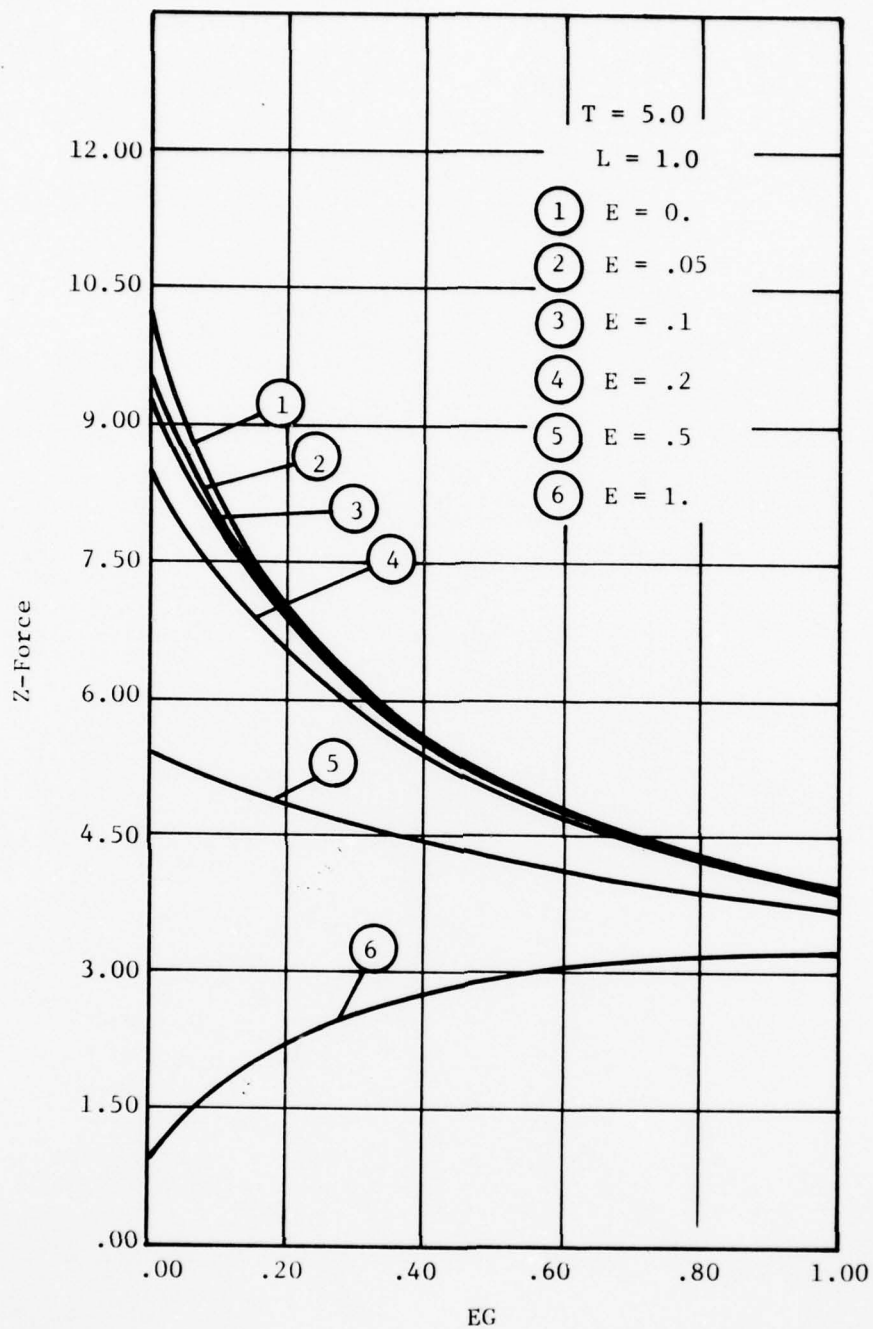


Fig. 4-20 Z-Force Versus EG ($T = 5.0$, $L = 1.0$)

791282

Figures 4-21 through 4-26 show the variation of X-force with the gap EG at various values of the eccentricity E and at different values of T and L. The transverse forces approach zero at large values of gap, as expected. The rate of decrease appears to depend on the size of the magnet.

4.5 Results and Discussion for Cylinder-Shaped Magnets

The double integrals for the normal and transverse forces were evaluated by using the Gaussian quadrature technique. Considerable computational difficulty was experienced in terms of convergence of the integral at lower order Gaussian quadrature schemes. This difficulty was overcome by dividing the interval of the outer integral (of the double integral) into four equal subintervals. A 24 x 16 quadrature was used in each of these subintervals. A separate computer program written for this purpose was run on a Control Data computer system.

A parametric study similar to the one reported in the previous section was carried out for the cylinder-shaped magnets also. The parameters studied were E, EG, and L, nondimensionalized with respect to the radius R of the magnets. The results have been plotted with respect to E and EG. Figures 4-27 through 4-38 show these plots.

Figure 4-27 shows a plot of the normal repulsive force against eccentricity. No negative values of Z-force are predicted in this case, as opposed to the rectangular magnets. This appears to be due to the geometry of the cylindrical magnets.

Figures 4-28 and 4-29 show the variation of Z-force with eccentricity at various values of gap and at different values of L. An increase in L increases the Z-force, but less than proportionately. The reasons are similar to those cited in the previous section on rectangular magnets.

Figure 4-30 shows the transverse component of the repulsive force (X-force) plotted against eccentricity at various values of the gap. The transverse force is zero at zero eccentricity because of symmetry. The transverse force increases with E, reaches a maximum, and then decreases with further increase

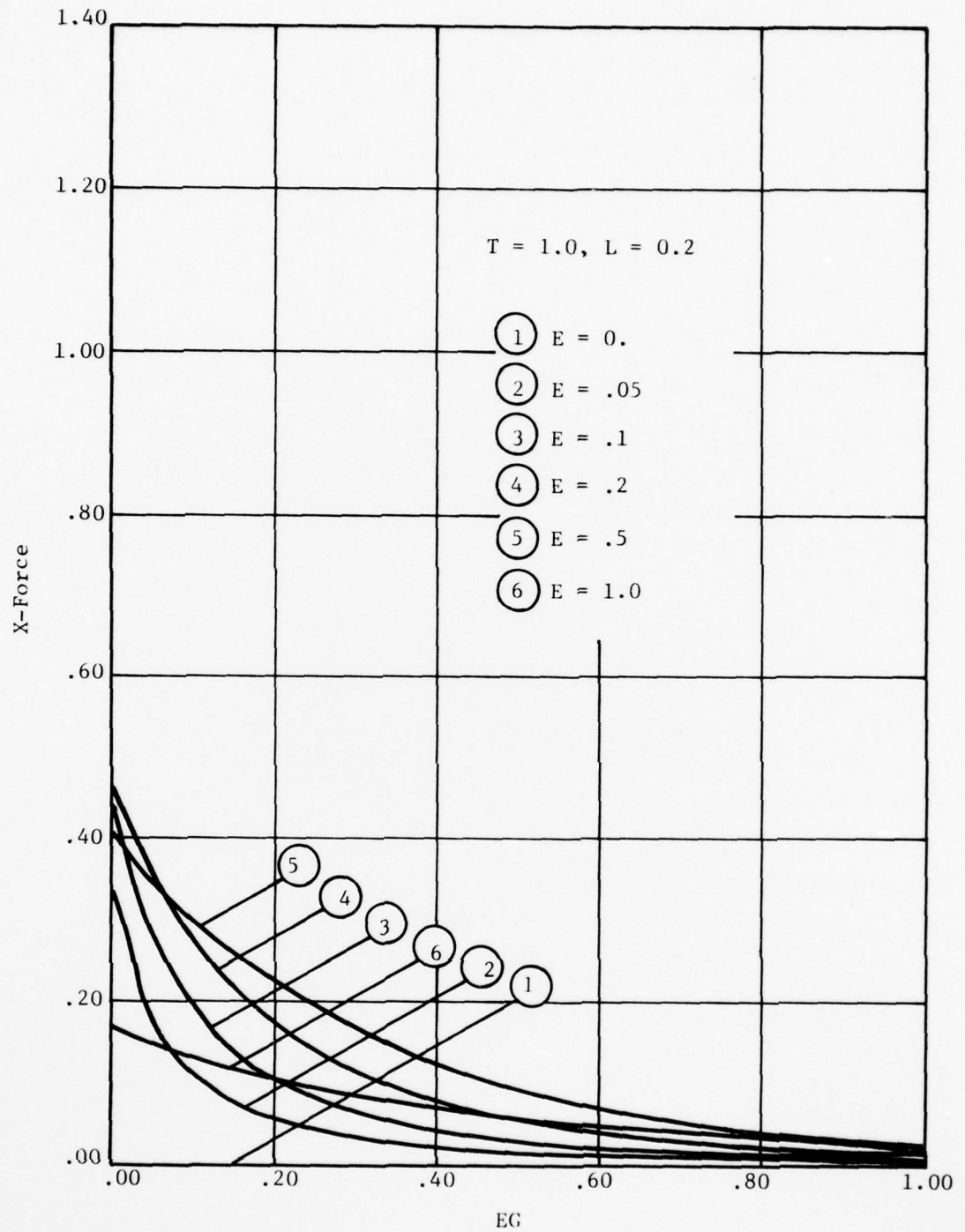


Fig. 4-21 X-Force Versus EG ($T = 1.0, L = 0.2$)

751203

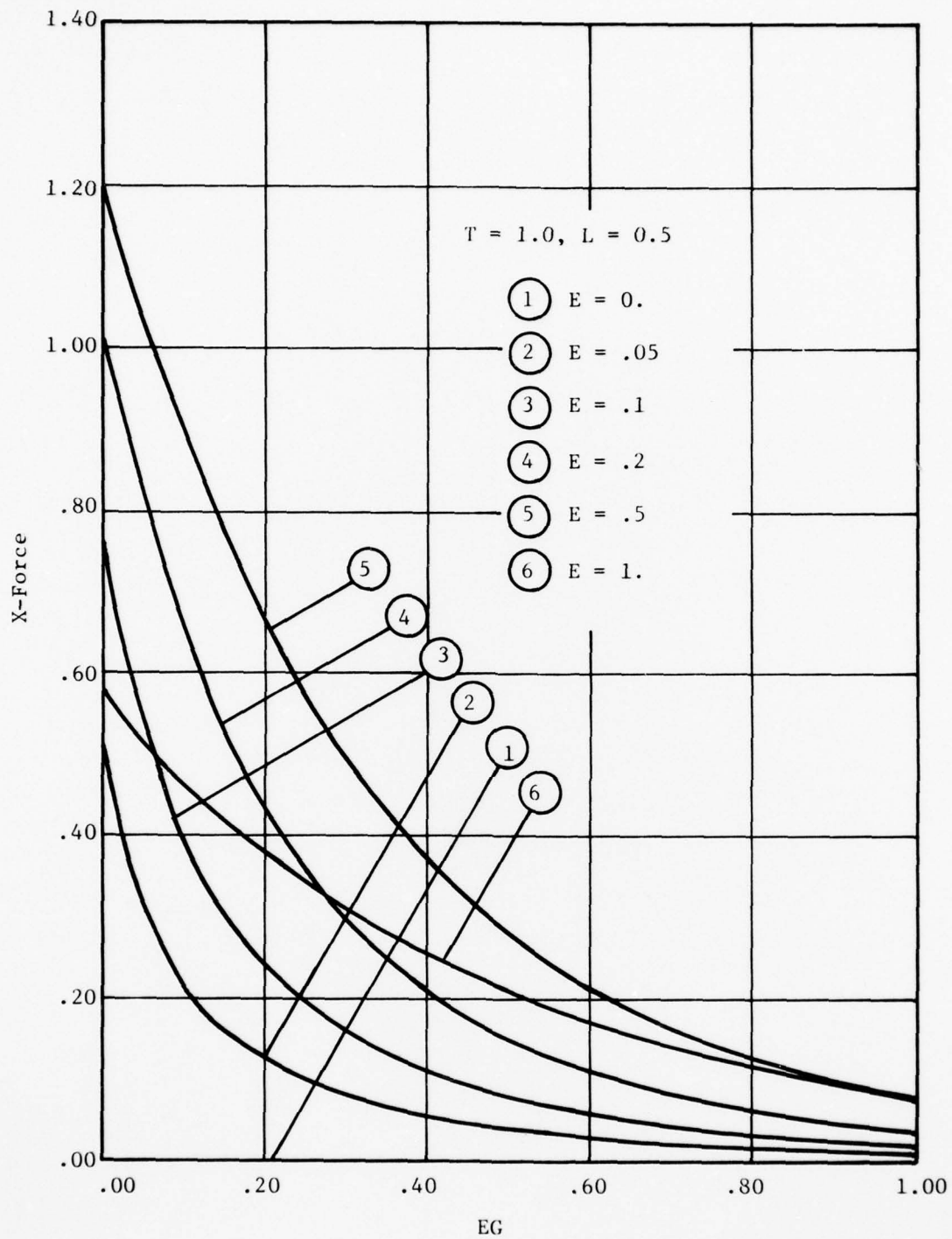


Fig. 4-22 X-Force Versus EG ($T = 1.0, L = 0.5$)

791234

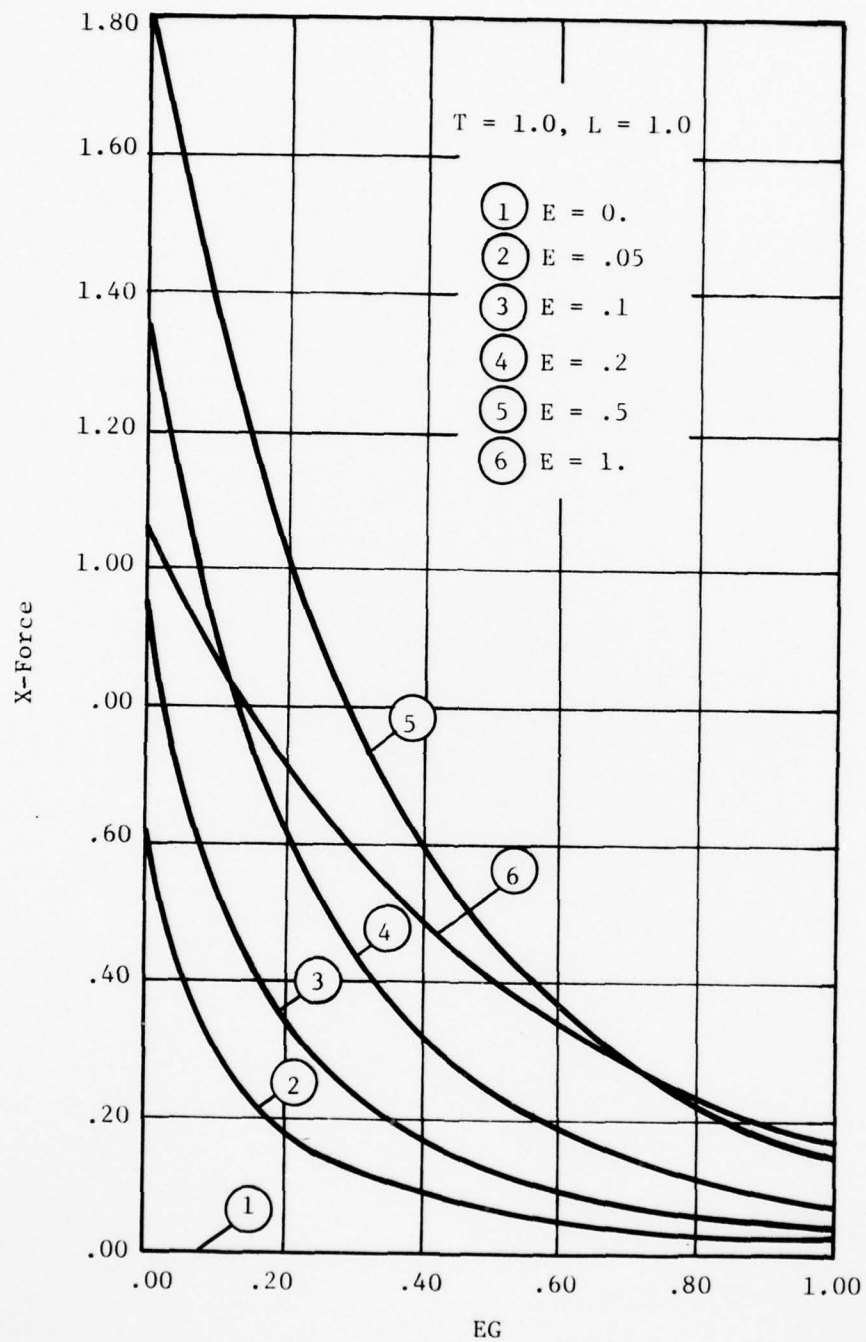


Fig. 4-23 X-Force Versus EG ($T = 1.0$, $L = 1.0$)

791255

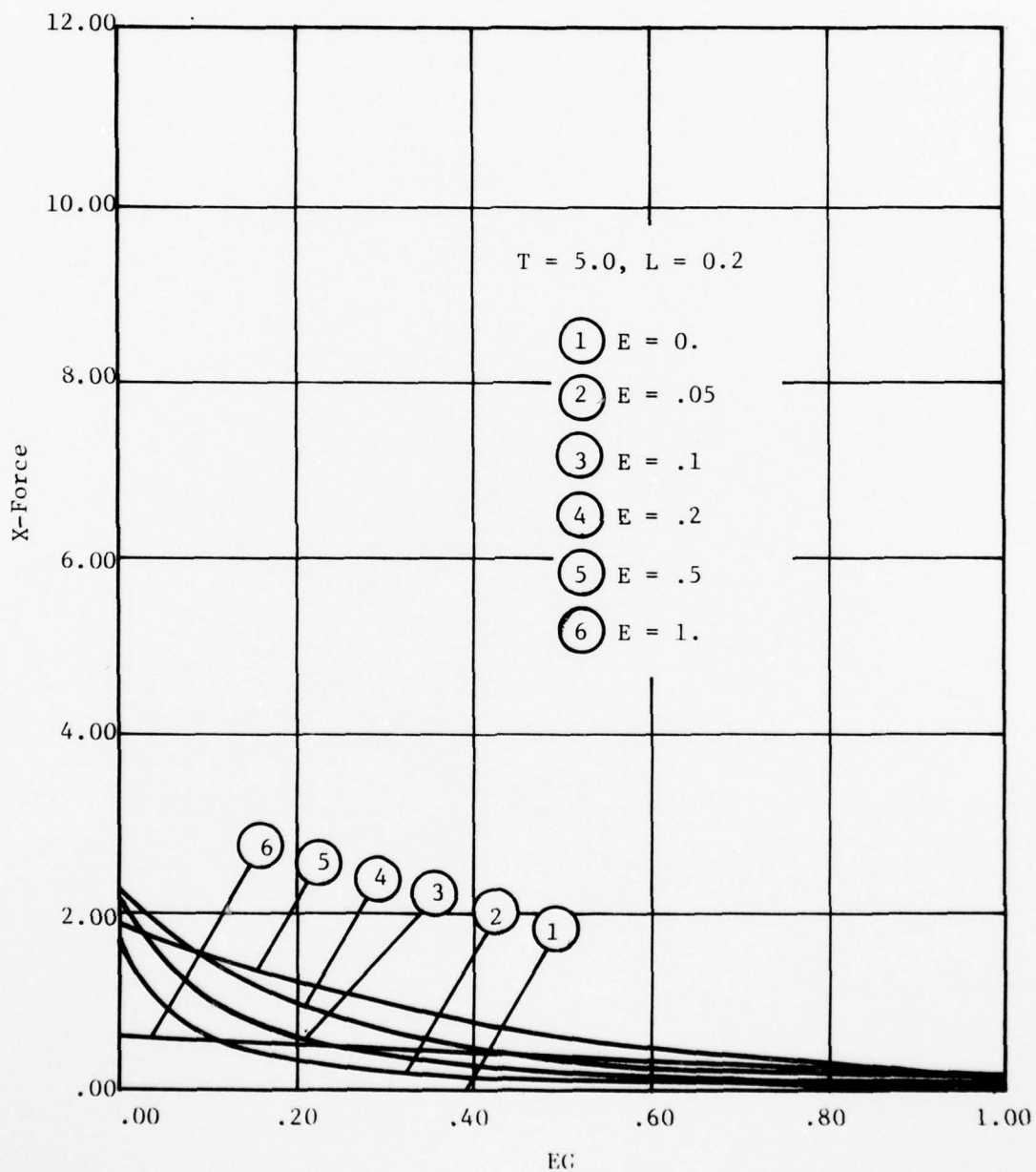


Fig. 4-24 X-Force Versus EG ($T = 5.0, L = 0.2$)

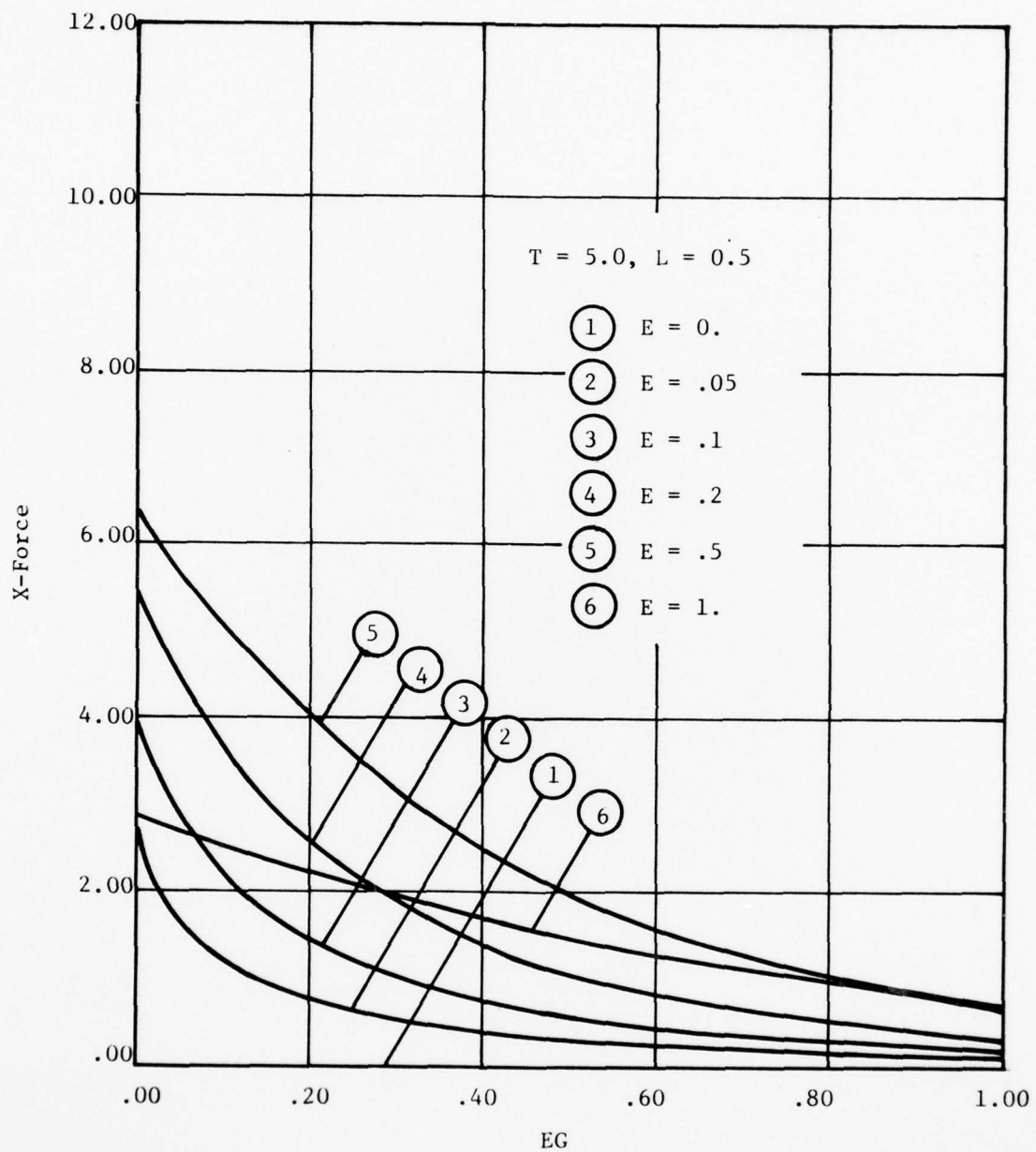


Fig. 4-25 X-Force Versus EG ($T = 5.0, L = 0.5$)

791257

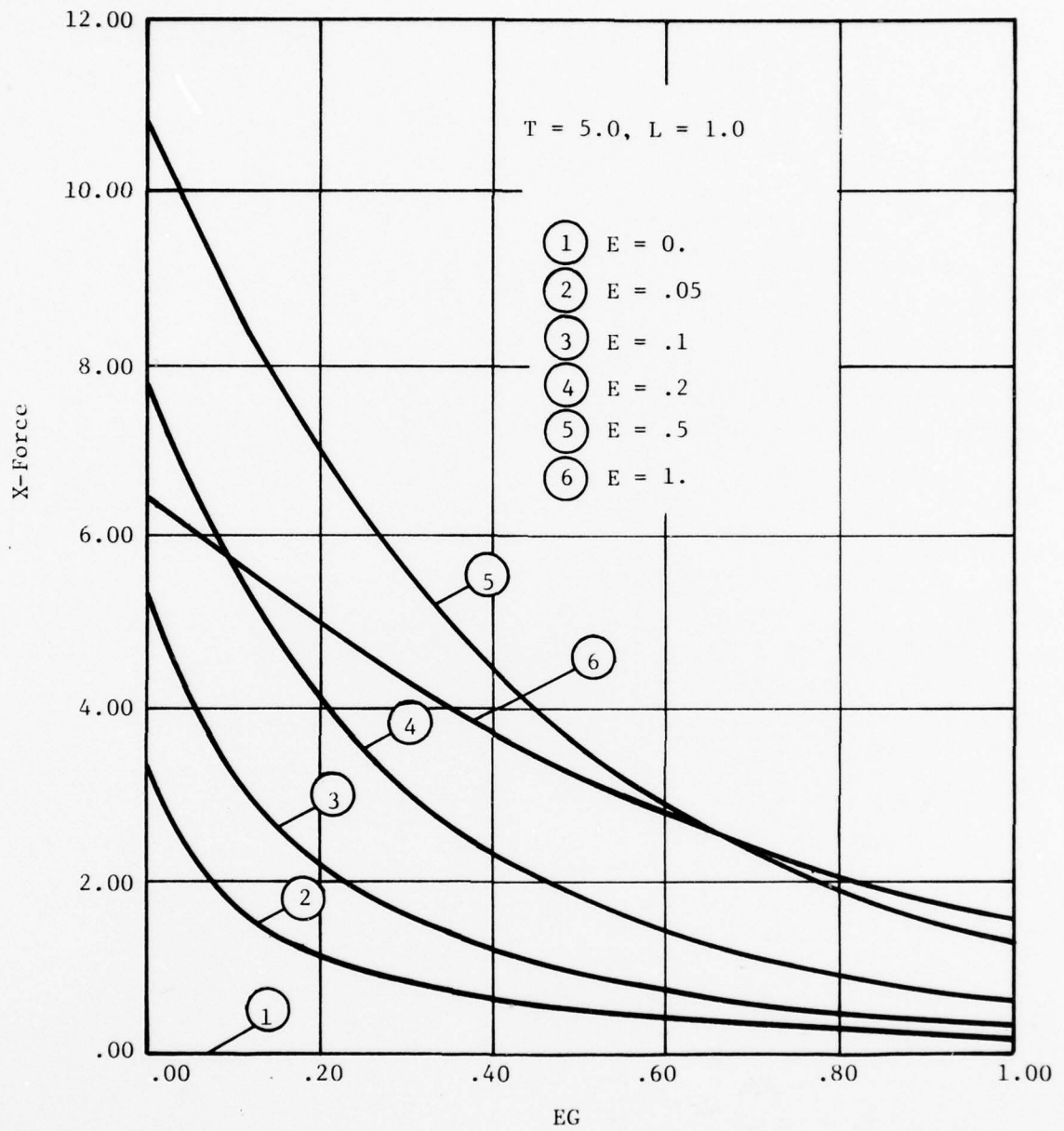


Fig. 4-26 X-Force Versus EG ($T = 5.0, L = 1.0$)

791288

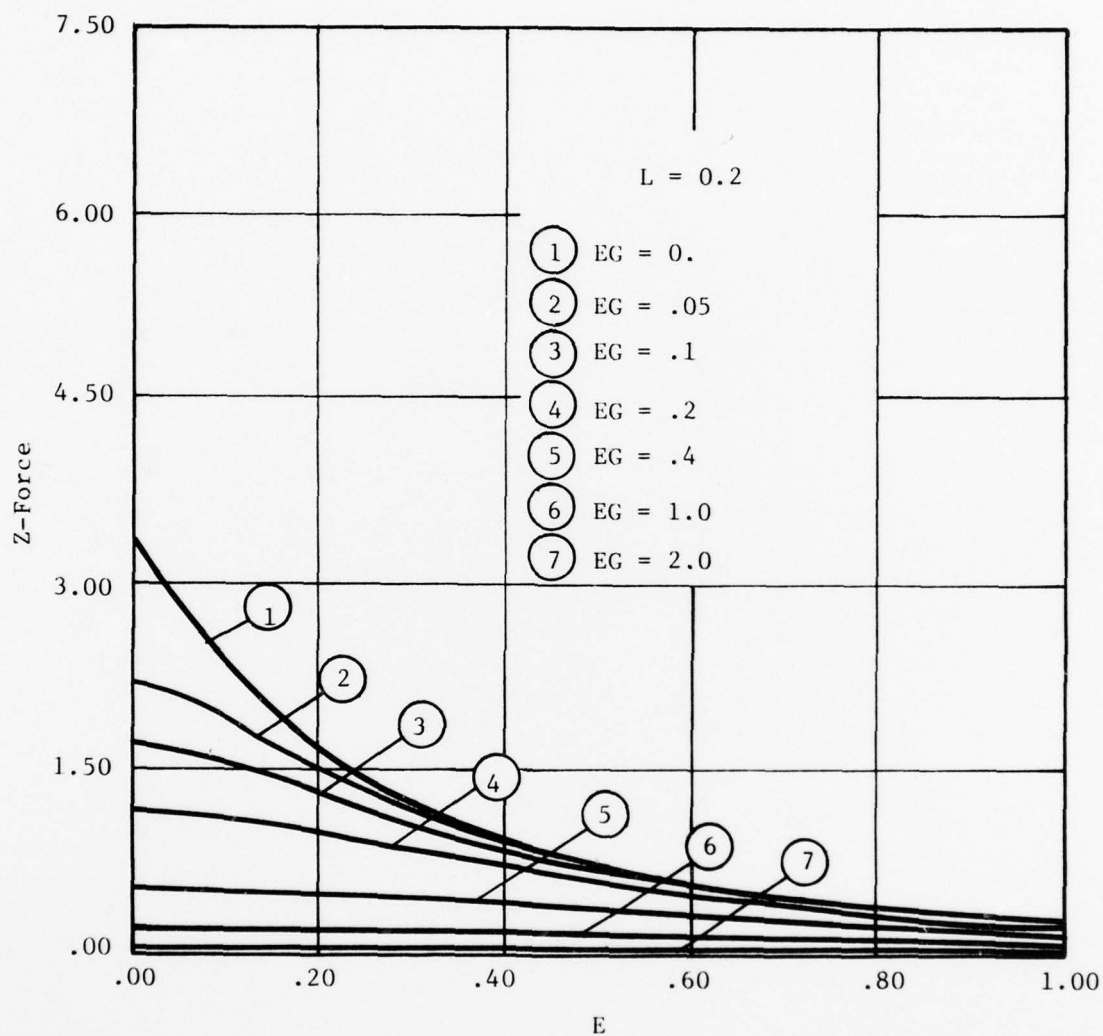


Fig. 4-27 Z-Force Versus E ($L = 0.2$)

791239

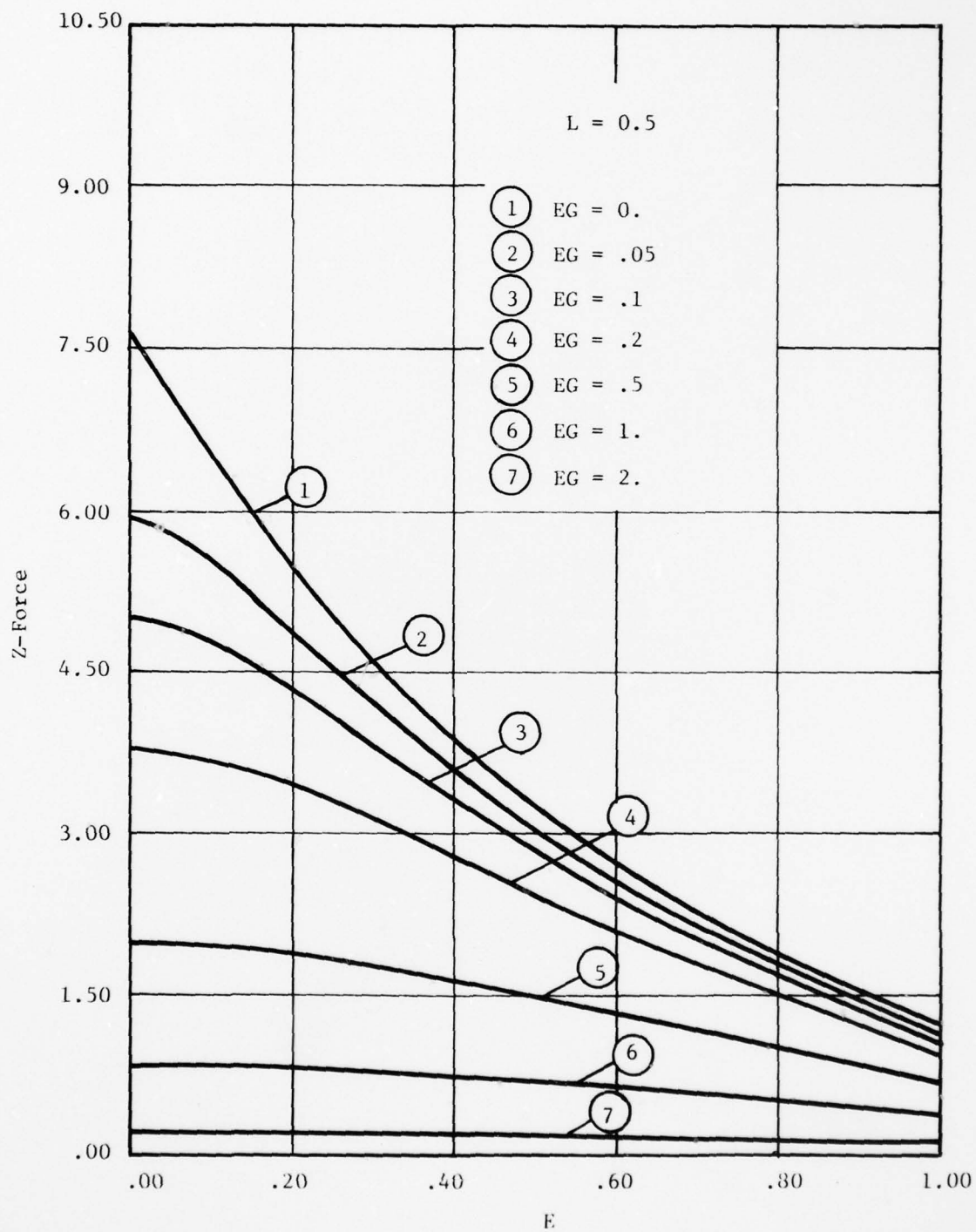


Fig. 4-28 Z-Force Versus E ($L = 0.5$)

791290

AD-A065 923

MECHANICAL TECHNOLOGY INC LATHAM NY RESEARCH AND DEV--ETC F/6 13/9
INVESTIGATION OF MAGNETIC FIELDS AND FORCES ARISING IN CLOSED--ETC(U)
FEB 79 H S NAGARAJ, J A MCCORMICK
MTI-79TR35

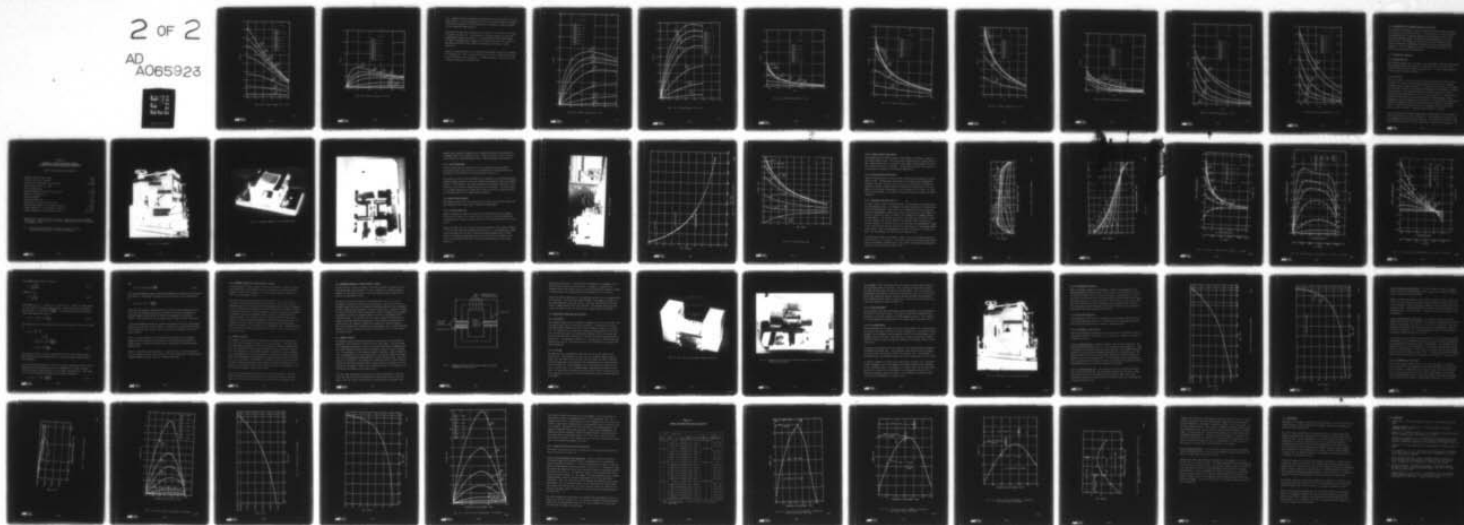
N00014-78-C-0098

NL

UNCLASSIFIED

2 OF 2

AD
A065923



END
DATE
FILMED

5-79

DDC

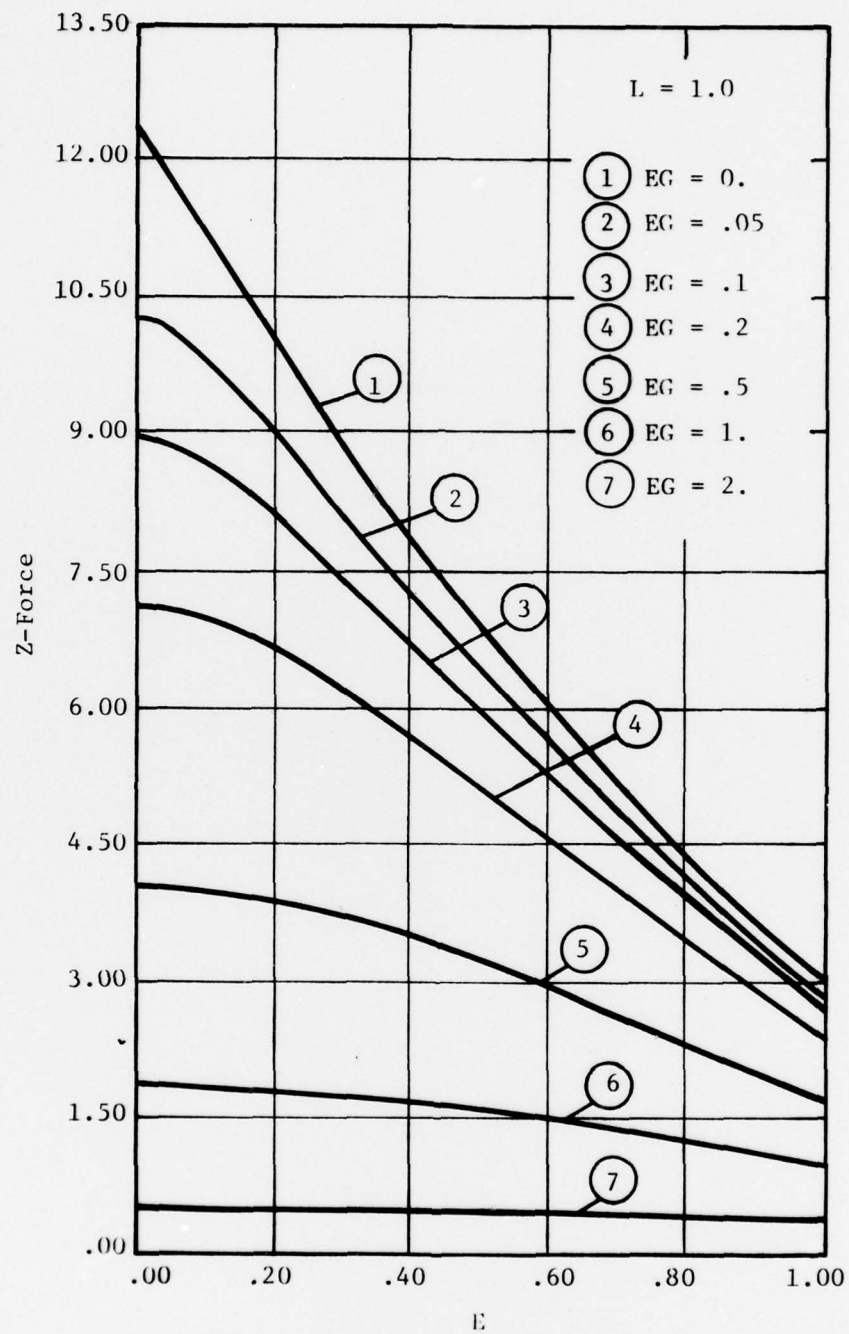


Fig. 4-29 Z-Force Versus E ($L = 1.0$)

791291

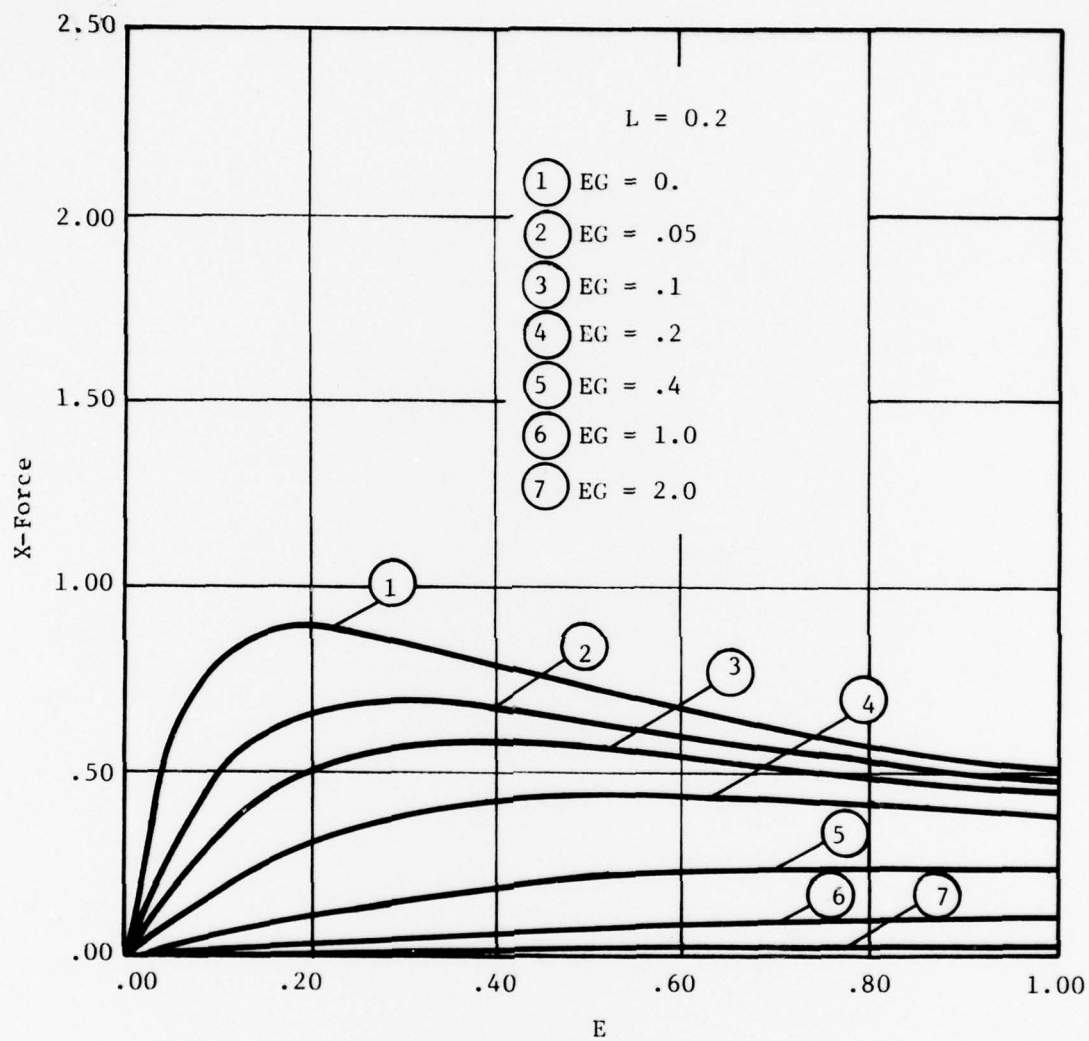


Fig. 4-30 X-Force Versus E ($L = 0.2$)

791292

in E. Reasons for such a behavior are identical to the ones cited in the previous section. In the decreasing side of the curve while stability of equilibrium can be achieved in X- and Z-directions, instability cannot be avoided in the Y-direction simultaneously.

Variations of X-force with eccentricity at values of $L = 0.5$ and 1.0 are shown in Figures 4-31 and 4-32. An increase in L initially produces a more than proportionate increase in X-force. By considering that the larger magnets are made by stacking smaller magnets one on top of the other, it can be seen that mutual interaction may enhance the transverse force under certain conditions.

X-force at various values of L is shown plotted against the gap EG in Figures 4-33 through 4-35. The repulsive Z-force goes to zero at large values of gap for all eccentricities, as expected. A similar behavior of X-force with gap is shown in Figures 4-36 through 4-38.

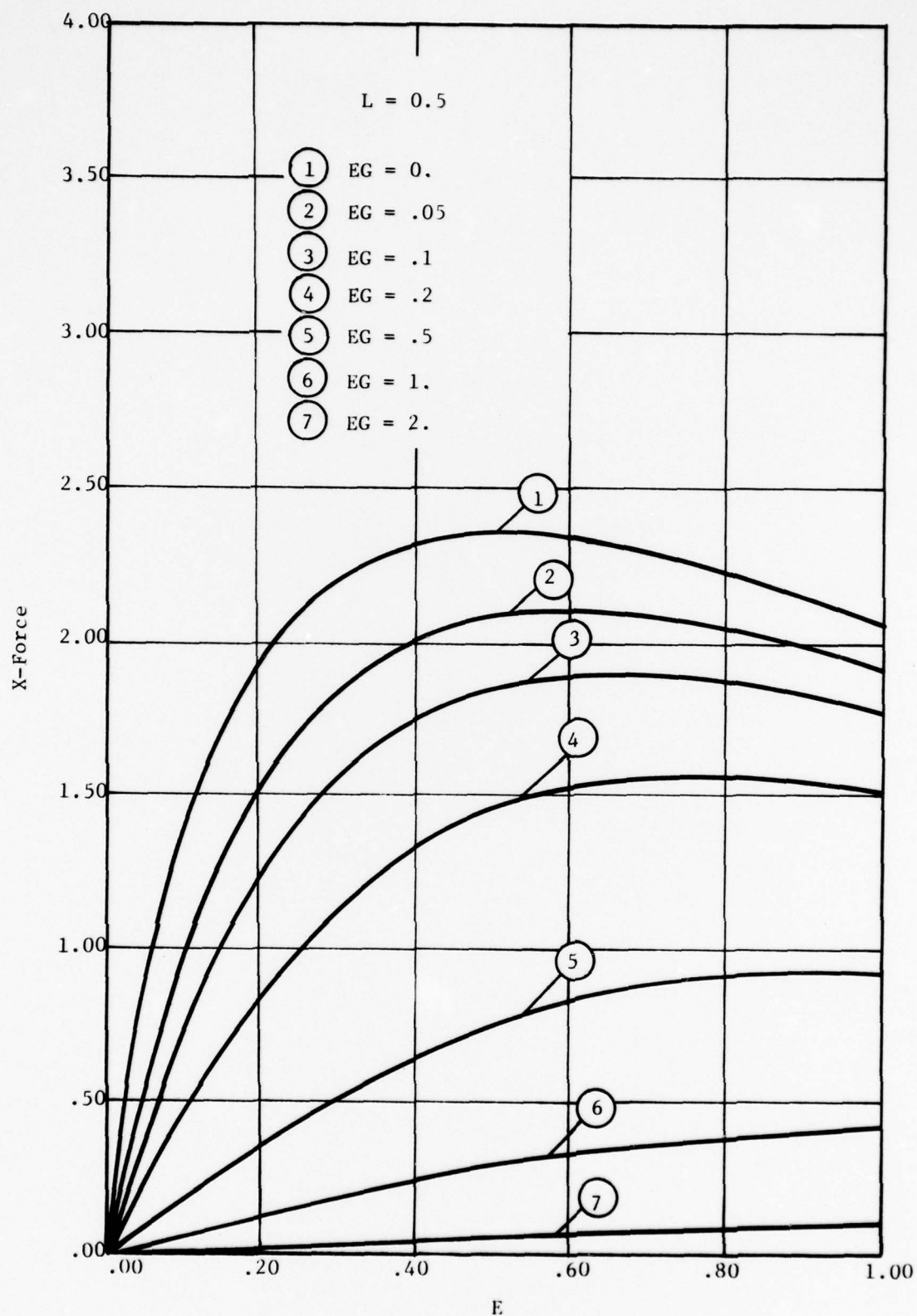


Fig. 4-31 X-Force Versus E (L = 0.5)

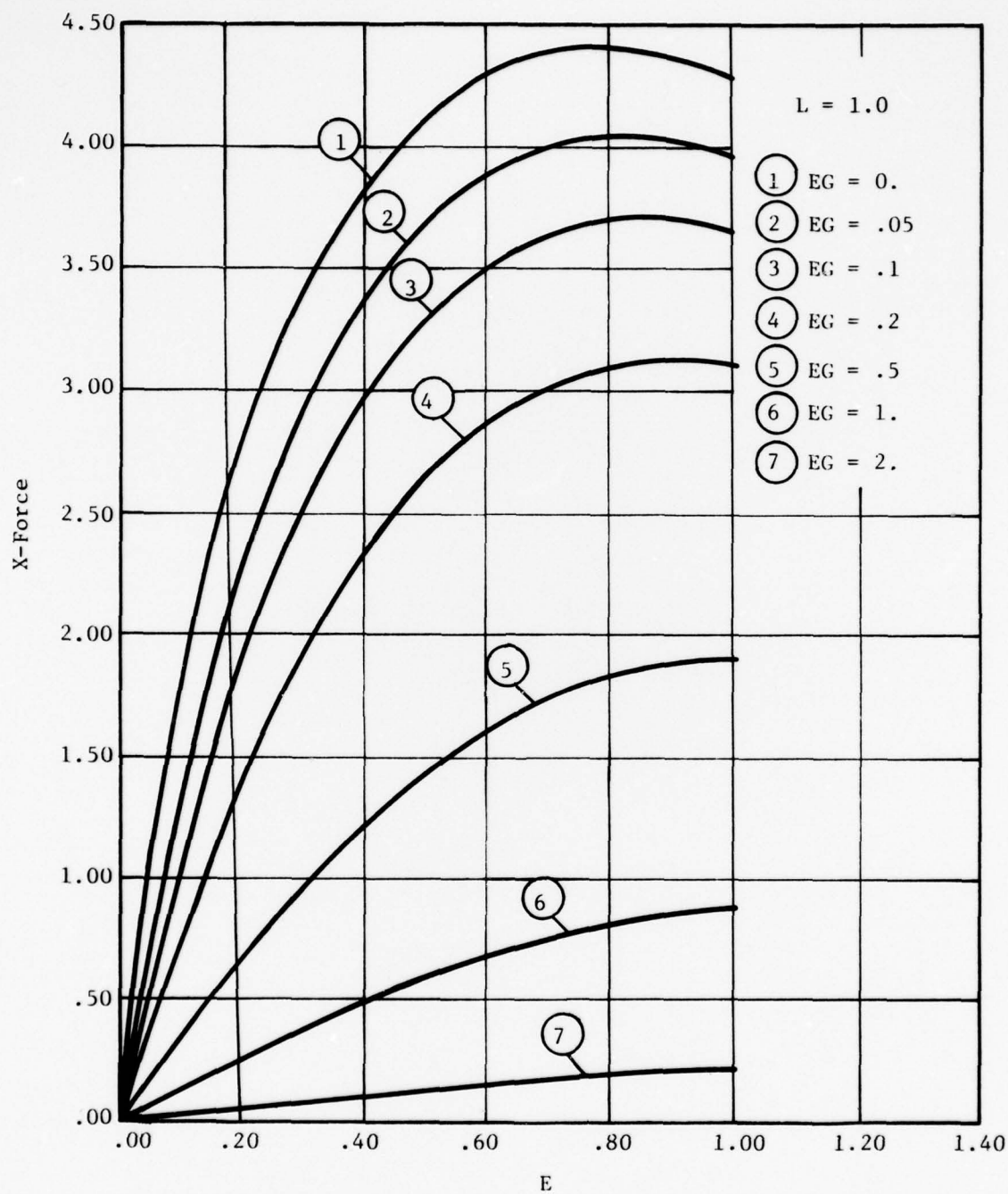


Fig. 4-32 X-Force Versus E ($L = 1.0$)

791294

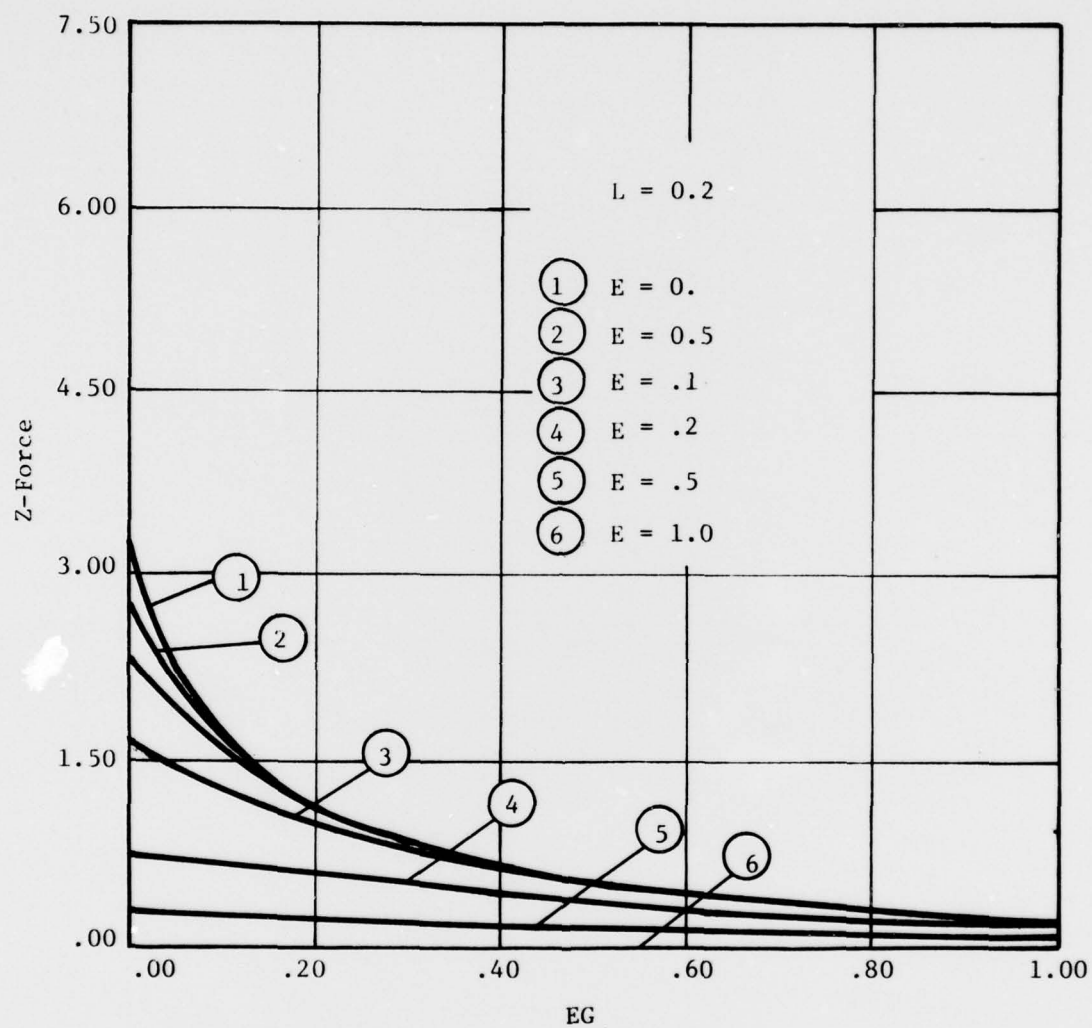


Fig. 4-33 Z-Force Versus EG ($L = 0.2$)

791295

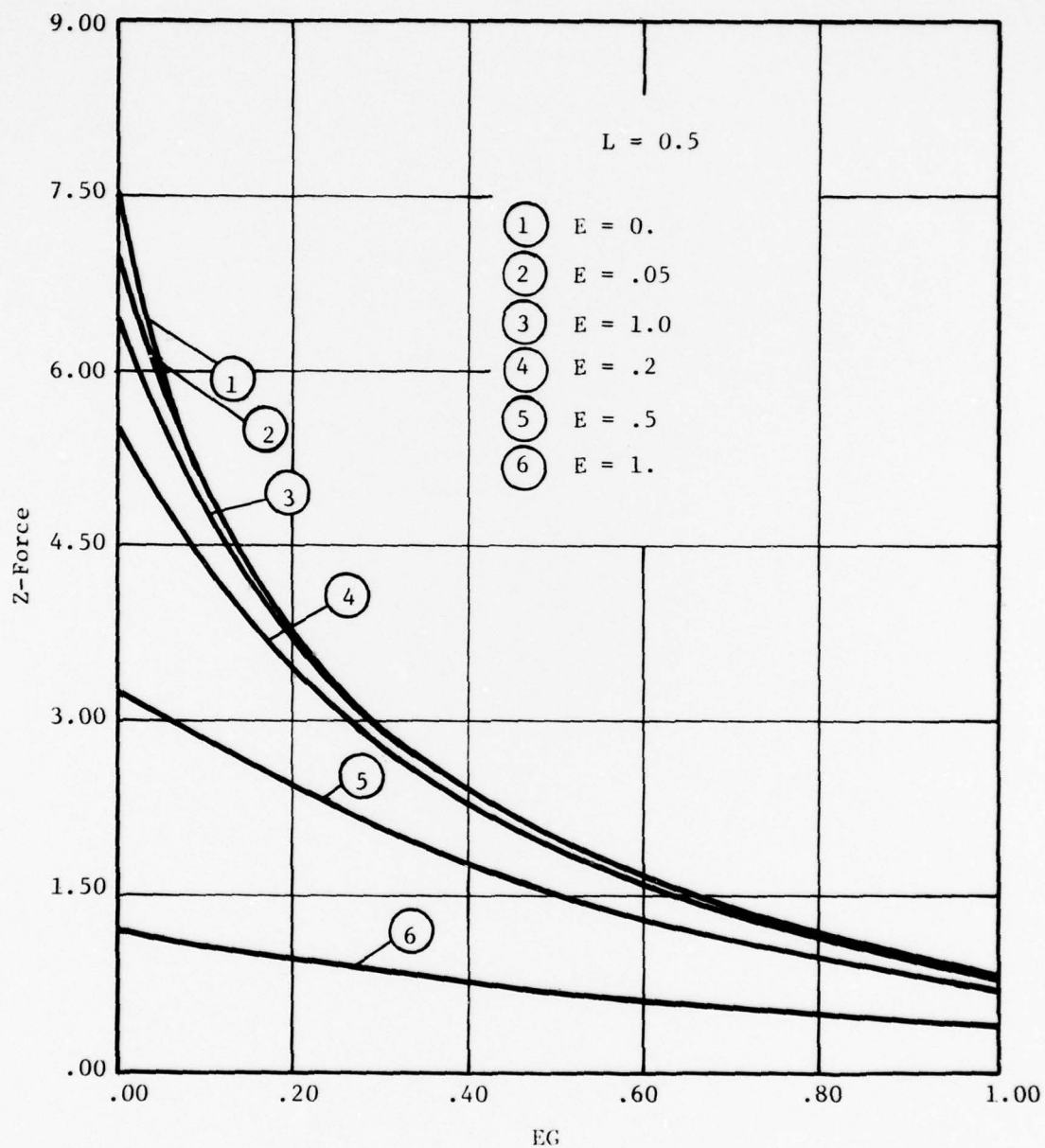


Fig. 4-34 Z-Force Versus EG ($L = 0.5$)

791296

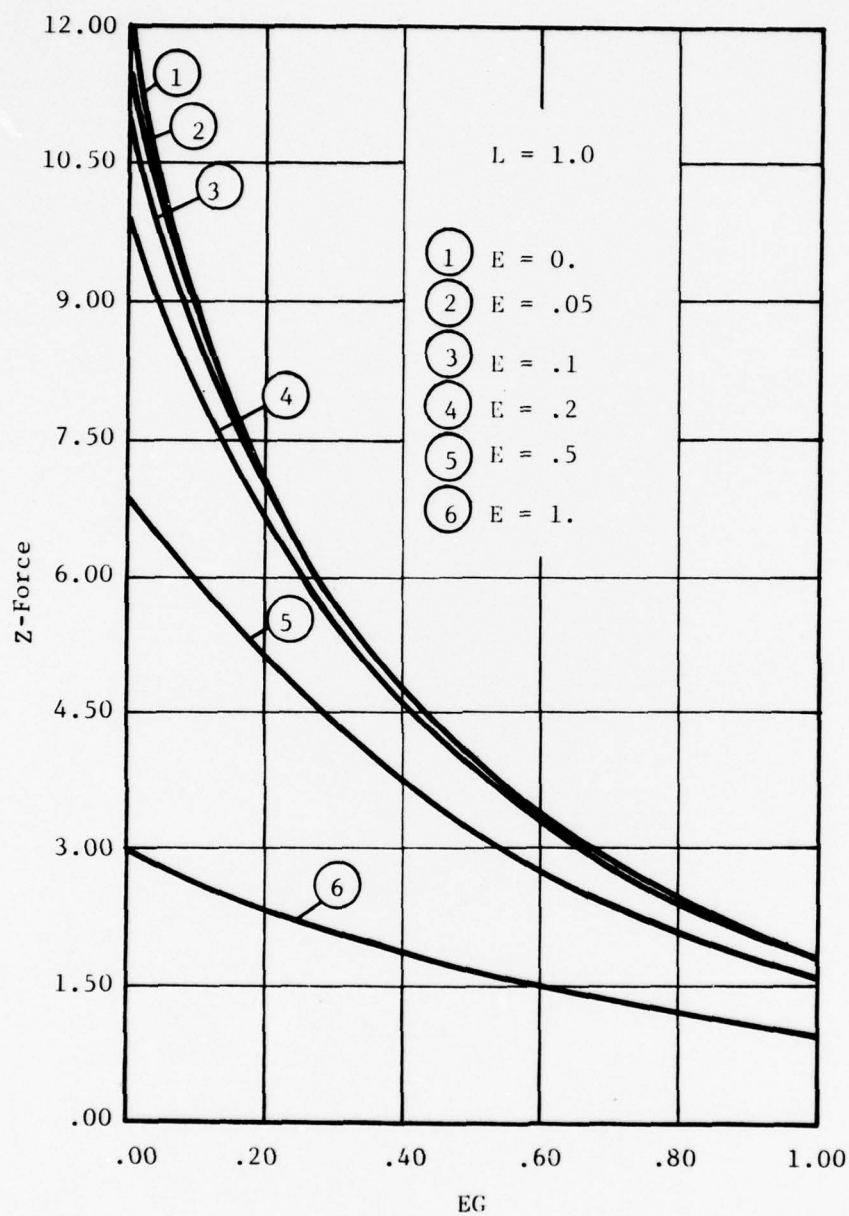


Fig. 4-35 Z-Force Versus EG ($L = 1.0$)

791297

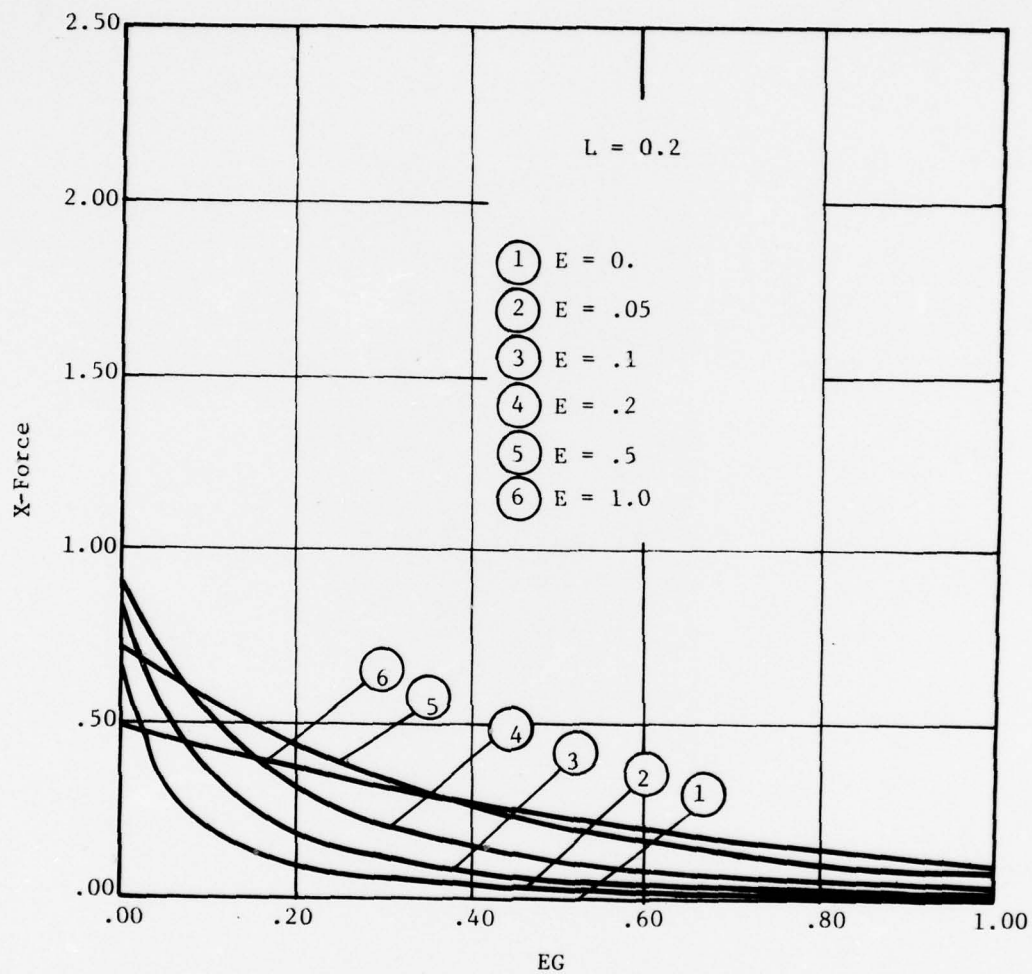


Fig. 4-36 X-Force Versus EG ($L = 0.2$)

791298

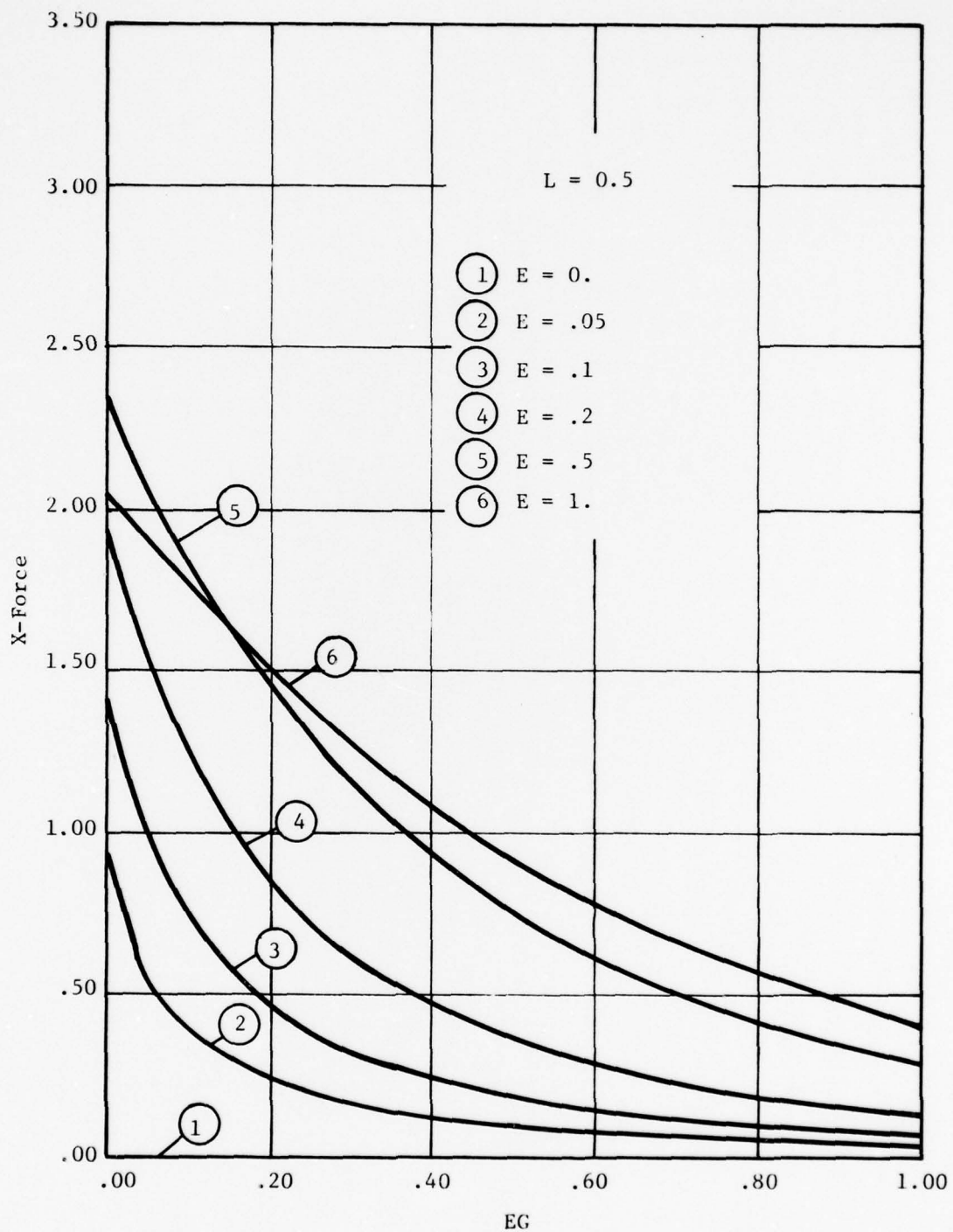


Fig. 4-37 X-Force Versus EG ($L = 0.5$)

791299

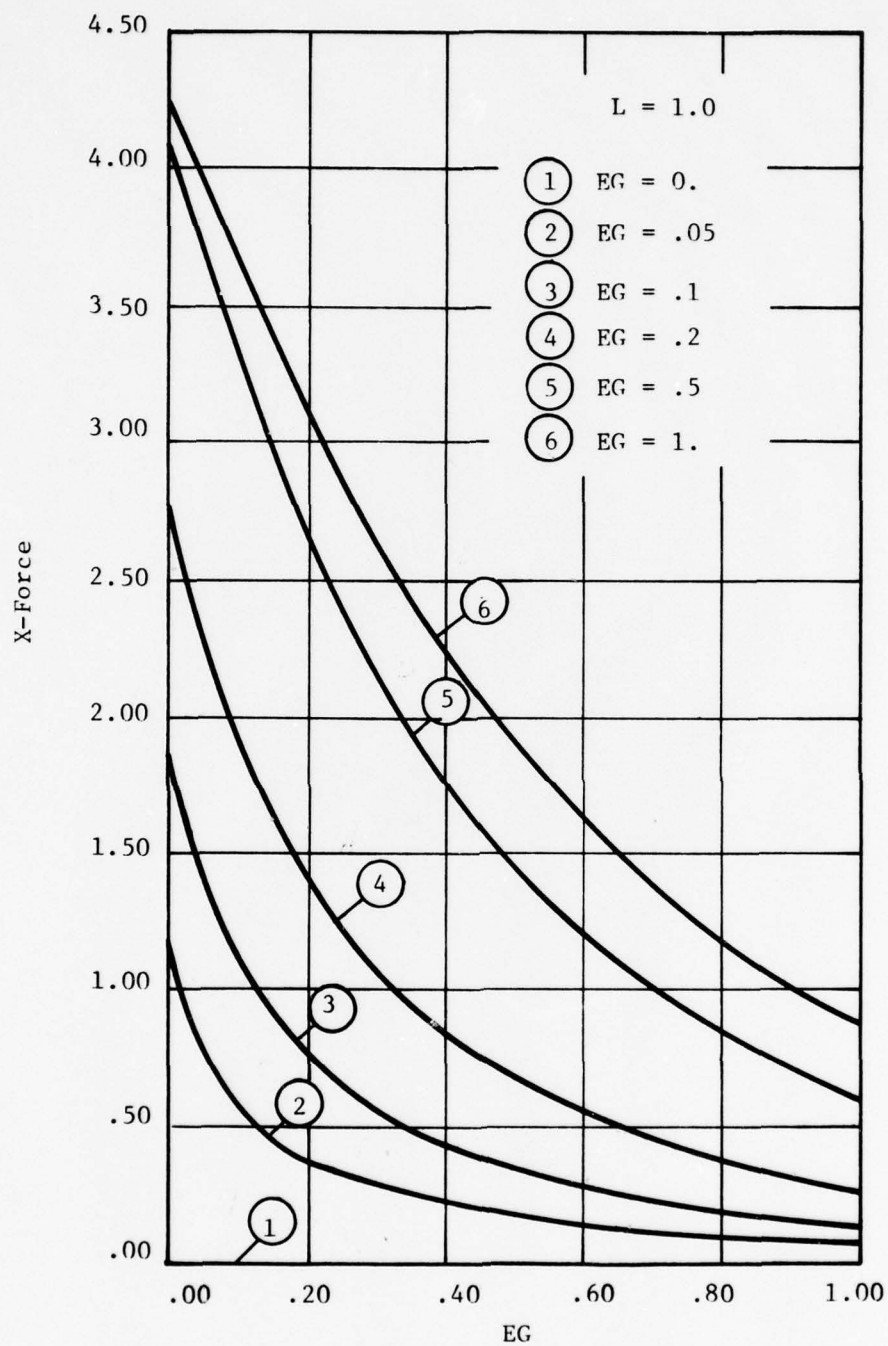


Fig. 4-38 X-Force Versus EG ($L = 1.0$)

791300

5.0 EXPERIMENTS WITH PERMANENT MAGNETS IN REPULSION

The analytical calculation of forces between two repelling permanent magnets was reported in the previous section. In this section, a report is made of the experimental work performed regarding the measurement forces between repelling permanent magnets to validate the theory reported in the previous section. Both normal and transverse forces were measured using quartz piezoelectric transducers as functions of gap and transverse displacement. A direct comparison is made of the forces predicted by the theory and those measured experimentally.

5.1 Experimental Apparatus

5.1.1 Magnet Material

The permanent magnets that were used in the experimental study were rectangular parallelopiped-shaped and were made of high coercivity, rare-earth-cobalt (Hicorex 90A from Hitachi Magnetics Corporation). A list of some properties of this material appears in Table 5-1.

5.1.2 Test Rig

The test rig used is the same as that described in Section 2.0 and is shown in Figure 5-1. Each of the two magnets being tested is held in a separate aluminum holder as shown in Figure 5-2. Extreme care was taken not to tighten the bolts much, because of the extreme brittleness of the sintered, rare-earth-cobalt material. The aluminum holders were directly attached to the top (movable) and the bottom plates, as can be seen in Figure 5-3. The top plate was moved up and down over the screw rods and the ball bushings, thereby changing the air gap separating the two magnets. The magnets were transversely displaced by manually moving the translation stage, mounted on the bottom plate. It was found necessary to mount a translation stage on the bottom plate in order to achieve a transverse displacement of 2 inches.

The air gap and the transverse displacement were monitored by dial indicators and also by DC-LVDT's as seen in Figure 5-1. Any required gap was set by using nonmagnetic shims and the dial indicator. The outputs of the LVDT's were used for obtaining plots of forces versus gap or transverse displacement. The

TABLE 5-1

PROPERTIES OF RARE-EARTH-COBALT MATERIAL
(HICOREX 90A OF HITACHI MAGNETICS CORPORATION)

Typical Room-Temperature Properties

Residual Induction (B_r), gauss	8,200
Coercive Force (H_c), oersteds	7,500
Intrinsic Coercive Force (H_{ci}), oersteds	>30,000
Energy Product (B.H) Max., mgo	16
Recoil Permeability	1.05
Required Magnetization Field (H_s) oersteds	20,000*
Hardness, Vickers D.P.H.	500
Density grams/cm ³	8.2
Tensile Strength, psi	5,000
Resistivity, ρ , micro ohm-cm (@ 25°C)	50
Thermal Conductivity, K, (cal-cm)/(°C.sec.cm ²)	0.025
Thermal Expansion to Orientation, cm/cm, °C	5×10^{-6}
Thermal Expansion \perp to Orientation, cm/cm, °C	13×10^{-6}

*Magnetization requirement based on having a magnet that has been thermally demagnetized. Higher fields are required if demagnetized state was achieved by a magnetic field.

Ref.: "Hicorex Rare-Earth-Cobalt Permanent Magnets", Technical Brochure-Hitachi Magnetics Corporation, Michigan.

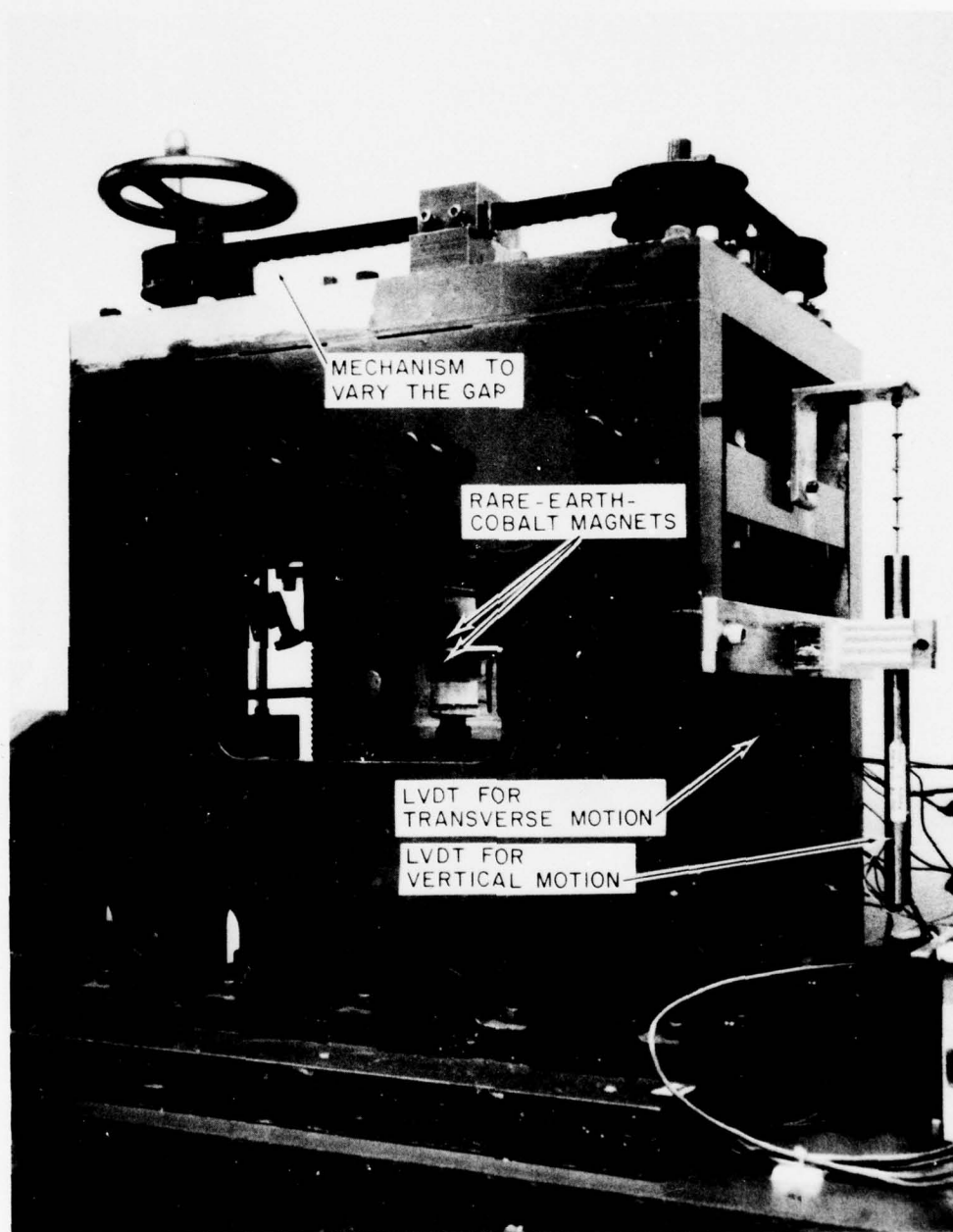


Fig. 5-1 Test Apparatus

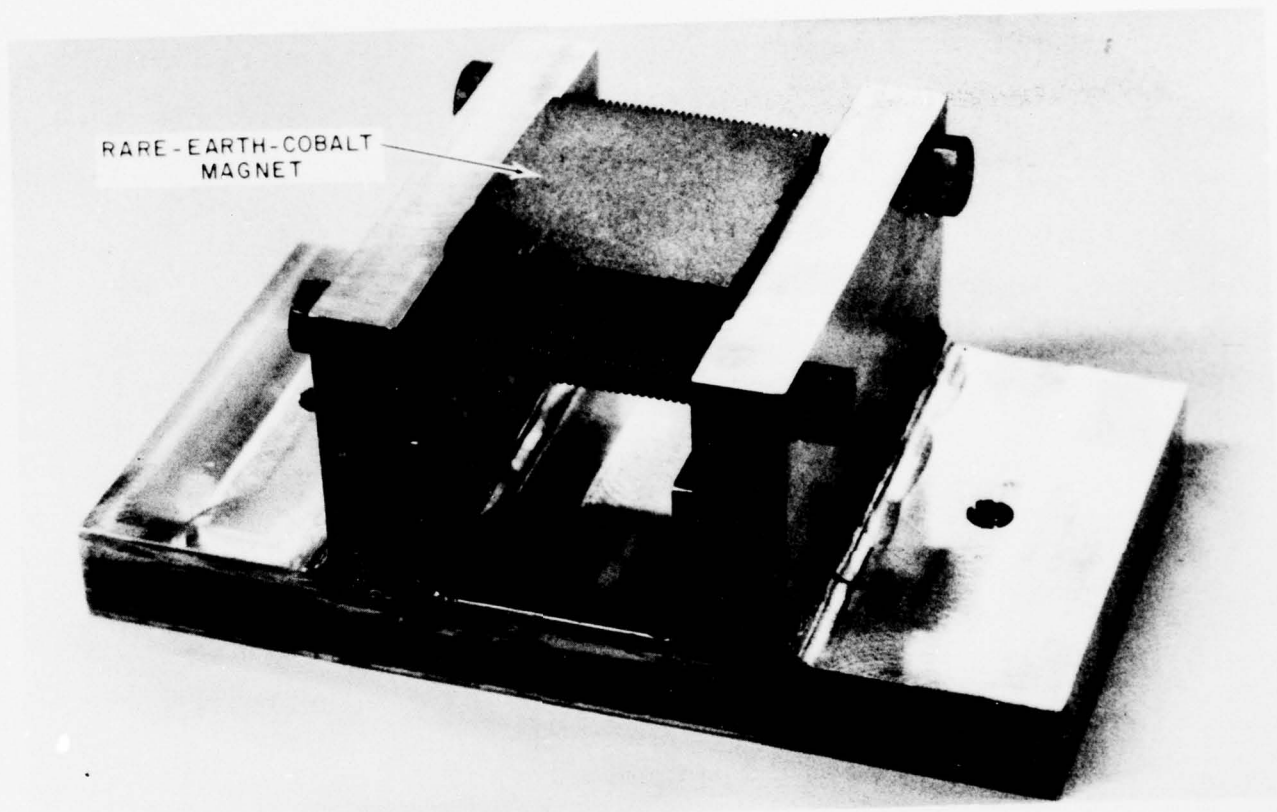


Fig. 5-2 Permanent Magnet in the Aluminum Holder

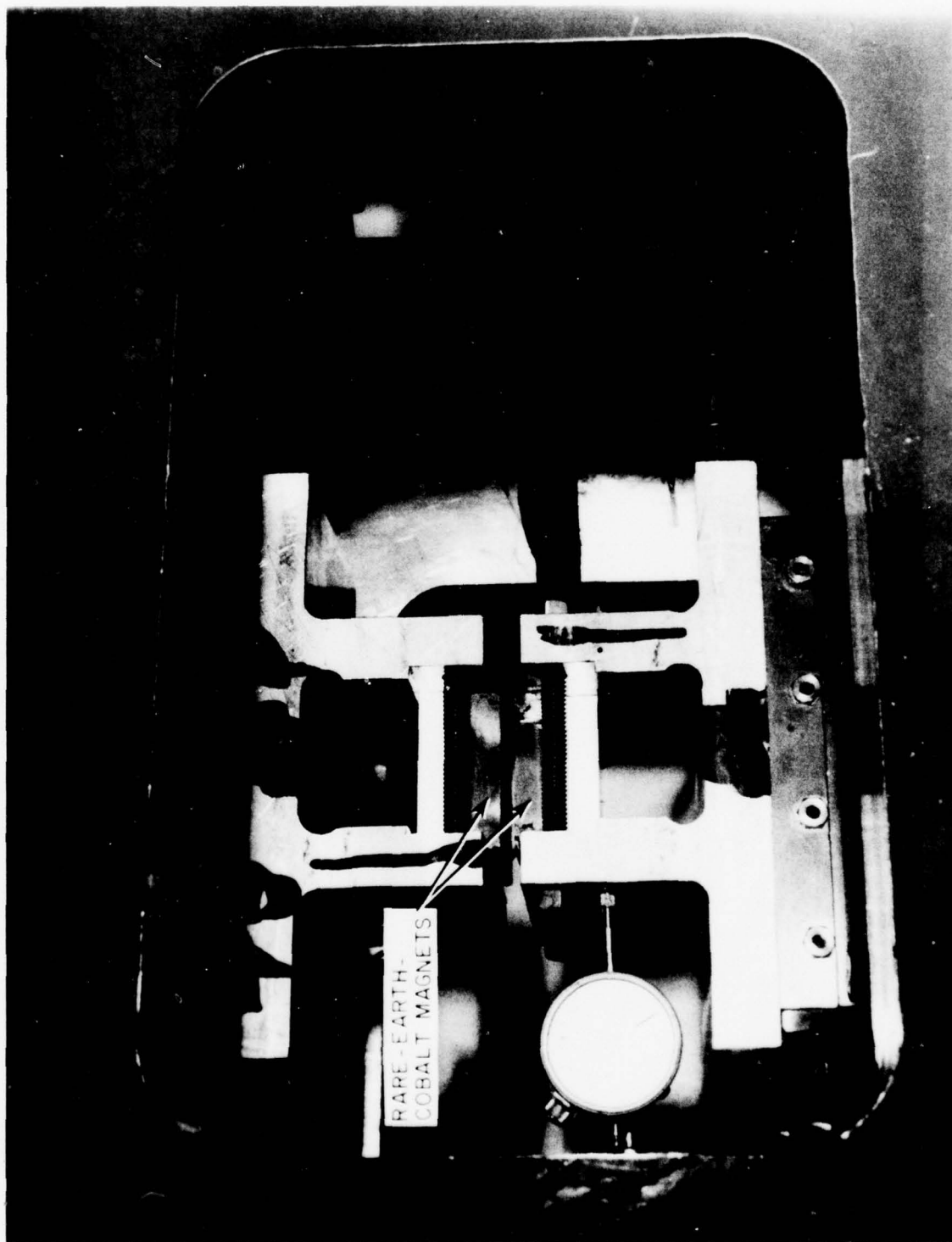


Fig. 5-3 Arrangement of Magnets Used in Experiments

MTI-18884

magnets were accurately aligned in the transverse direction by searching for a minimum value of the transverse force. Figure 5-4 shows a view of the test setup with all the instrumentation used for the measurements reported here.

5.1.3 Force Measurement

Both the normal and the transverse forces are measured using two multi-directional quartz piezoelectric force transducers, and the measurement was performed in a way similar to that described in Section 3.0.

The outputs of the two force transducers are connected to the charge amplifiers through summing junctions so that the normal and transverse forces are measured directly. The outputs of the charge amplifiers are directly connected to the Y-axis of an X-Y plotter, whenever plots are to be recorded. The input cables to the charge amplifiers are always kept clean to avoid stray capacitance and the resulting drift of the charge amplifier output.

5.2 Results and Discussion

Experimental results will be presented in the form of plots of the normal and the transverse force versus gap or transverse displacement.

5.2.1 Z-Force Versus Gap

Figure 5-5 shows the curve of normal force versus gap when the two magnets are perfectly aligned. The figure shows the curves for both decreasing and increasing gaps, although the two curves do not significantly deviate from one another.

Figure 5-6 shows curves of Z-force versus gap (similar to that shown in Figure 5-5) at various values of transverse displacement (e). The minimum gap reached in all the tests was .010 inch. The forces reduce significantly at large values of transverse displacement and, as can be seen in the figure, the Z-force in fact becomes attractive instead of being repulsive at very large values of e .



Fig. 5-4 Test Setup

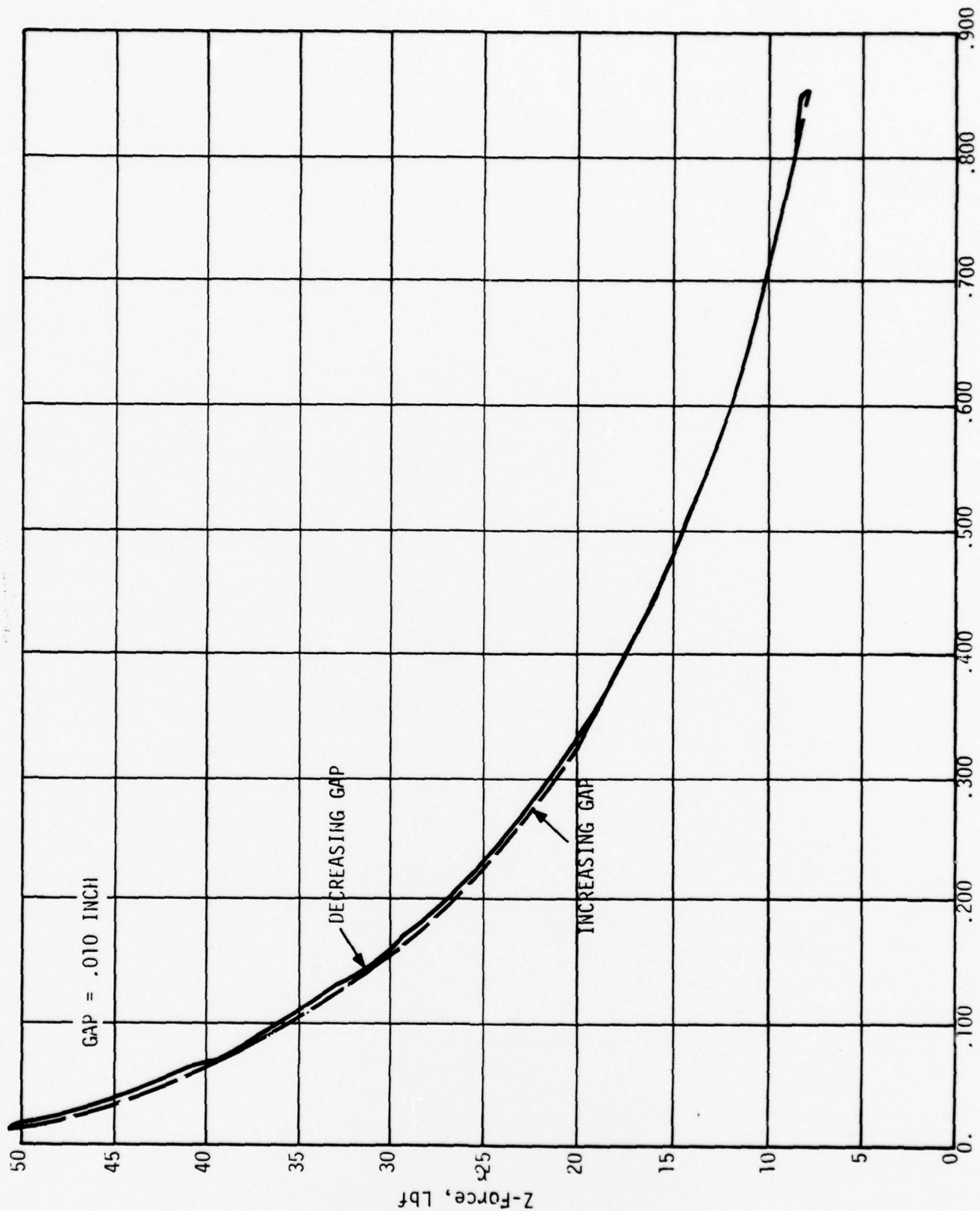


Fig. 5-5 Z-Force Versus Gap ($e=0$)

79P17

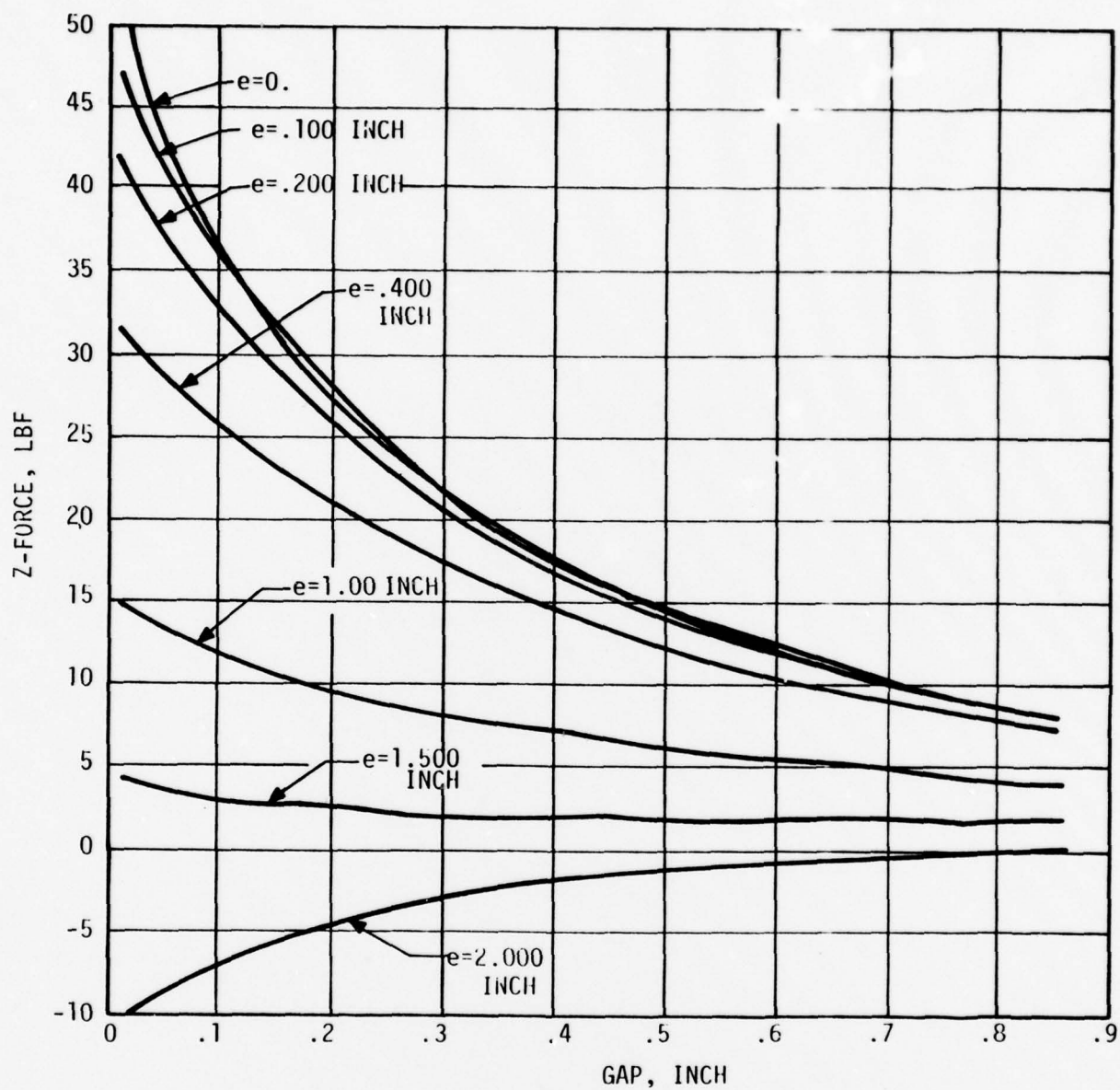


Fig. 5-6 Z-Force Versus Gap

79P17

5.2.2 X-Force Versus Displacement

The transverse force versus transverse displacement is plotted in Figure 5-7 at various values of gap. The forces reduce significantly at large values of gap. There appears to be a relatively large range of displacement over which the variation in X-force is minimal. The maximum transverse force appears to be only about 30 percent of the maximum normal force.

5.2.3 Z-Force Versus Displacement

Figure 5-8 shows a plot of Z-force versus transverse displacement at various values of gap. Although the curves shown in the figure were independently obtained, they are, in effect, cross plots of the data shown in Figure 5-6. Figure 5-8, however, clearly shows the variation of normal force as the two magnets are displaced transversely, one with respect to the other. At large values of displacement, the normal force becomes attractive instead of being repulsive.

5.2.4 Comparison with Theoretical Predictions

In order to make a direct comparison between the theoretical predictions and the experimental results, the computer code that was written to calculate and plot the nondimensional forces versus the nondimensional values of gap and transverse displacement (reported in Section 3.0) was run for the values of T equal to 1.0625 and L equal to 0.2469, corresponding to the magnets used in the experiments. The results thus obtained are shown by solid lines in Figures 5-9 through 5-11 and are similar to the results shown in Section 3.0. In these figures, the vertical axes on the left show the nondimensional values of the forces and the vertical axes on the right show the corresponding dimensional values. Both the nondimensional and the actual values of either the gap or the displacement are shown on the horizontal axes.

For comparison purposes, the theory is made to fit the experimental data for normal force at $E = 0$, and $EG = .05$, and the equivalent surface-current densities of the magnets (assumed equal to each other) are deduced as indicated in Equations (5-1) through (5-4) which follow.

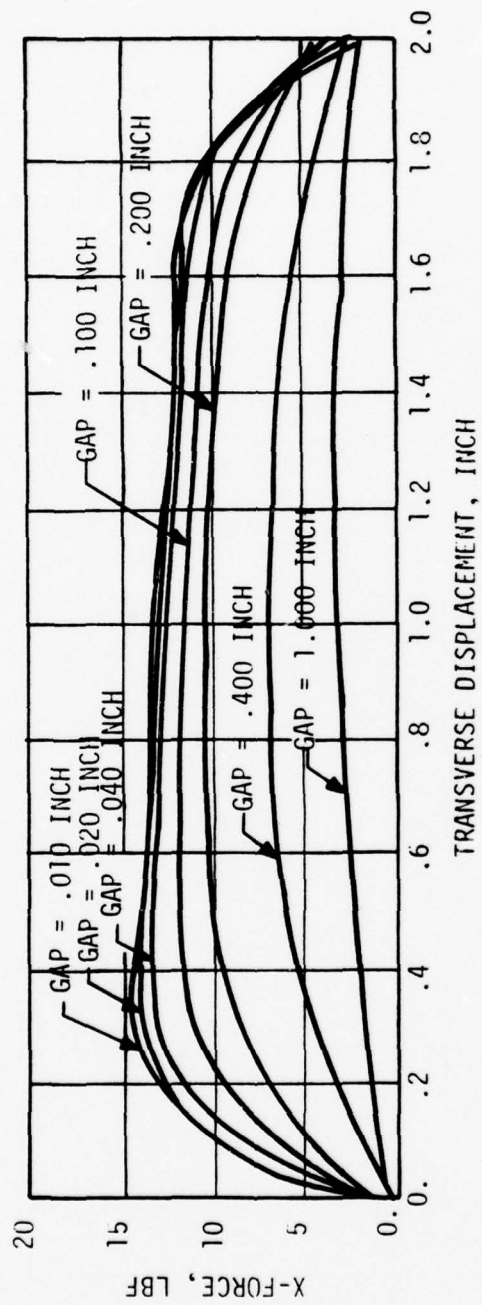
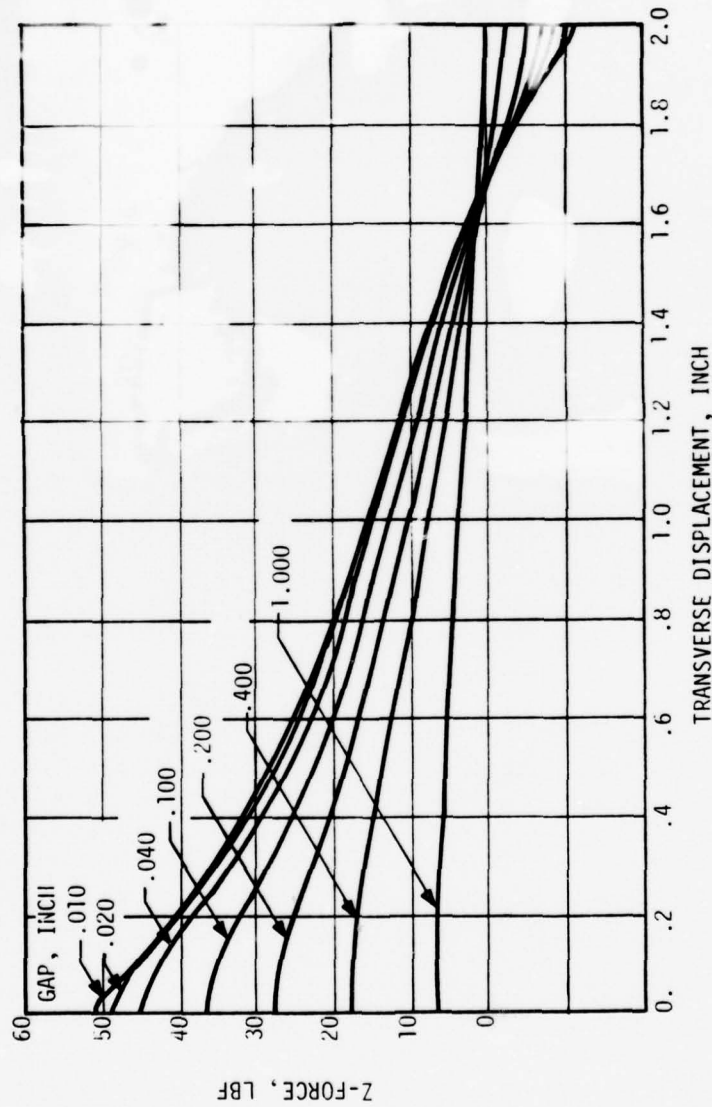


Fig. 5-7 X-Force Versus Displacement

79P17



79P17

Fig. 5-8 Z-Force Versus Displacement

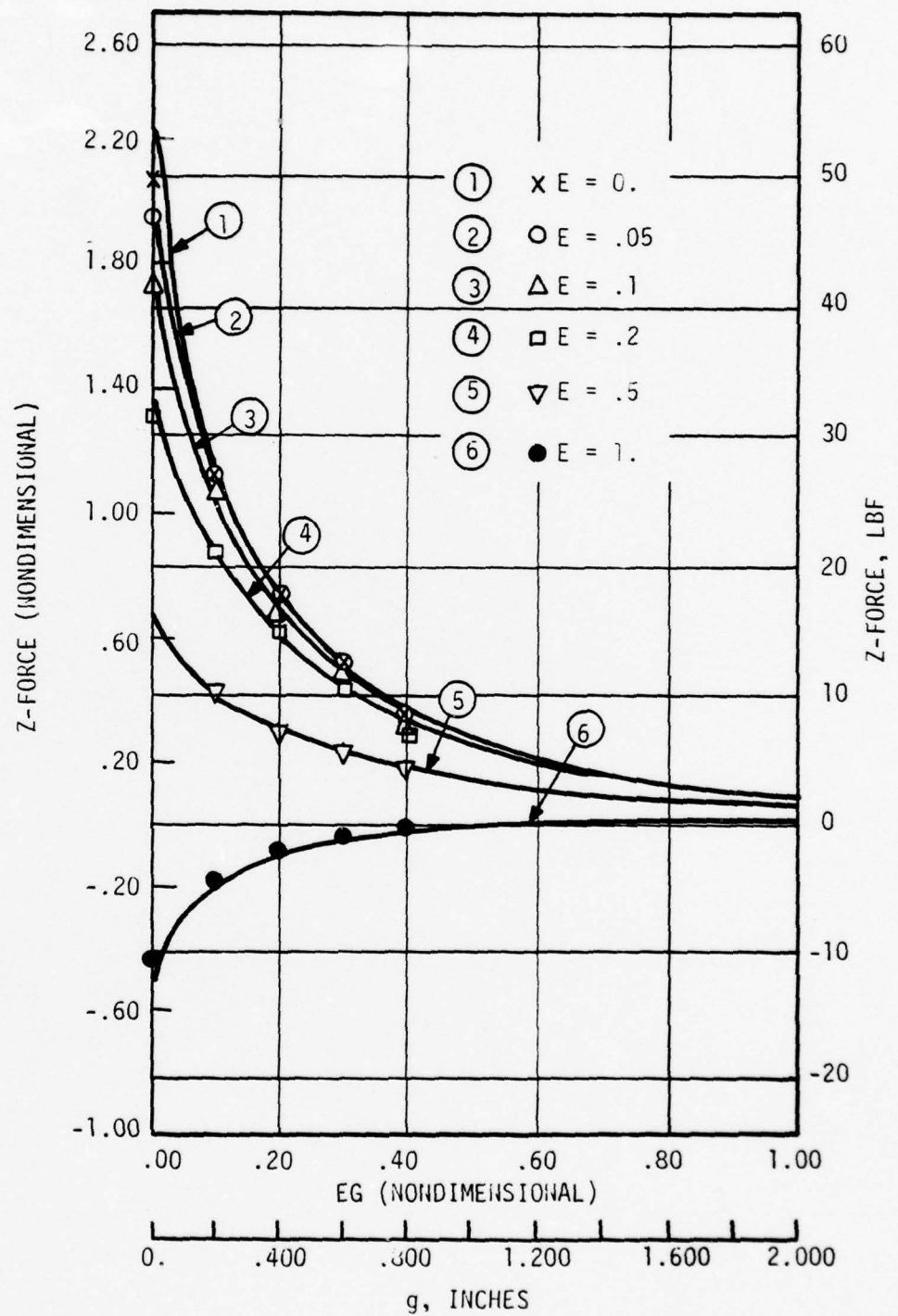


Fig. 5-9 Z-Force Versus Gap ($T = 1.0625$, $L = 0.2469$)

79P17

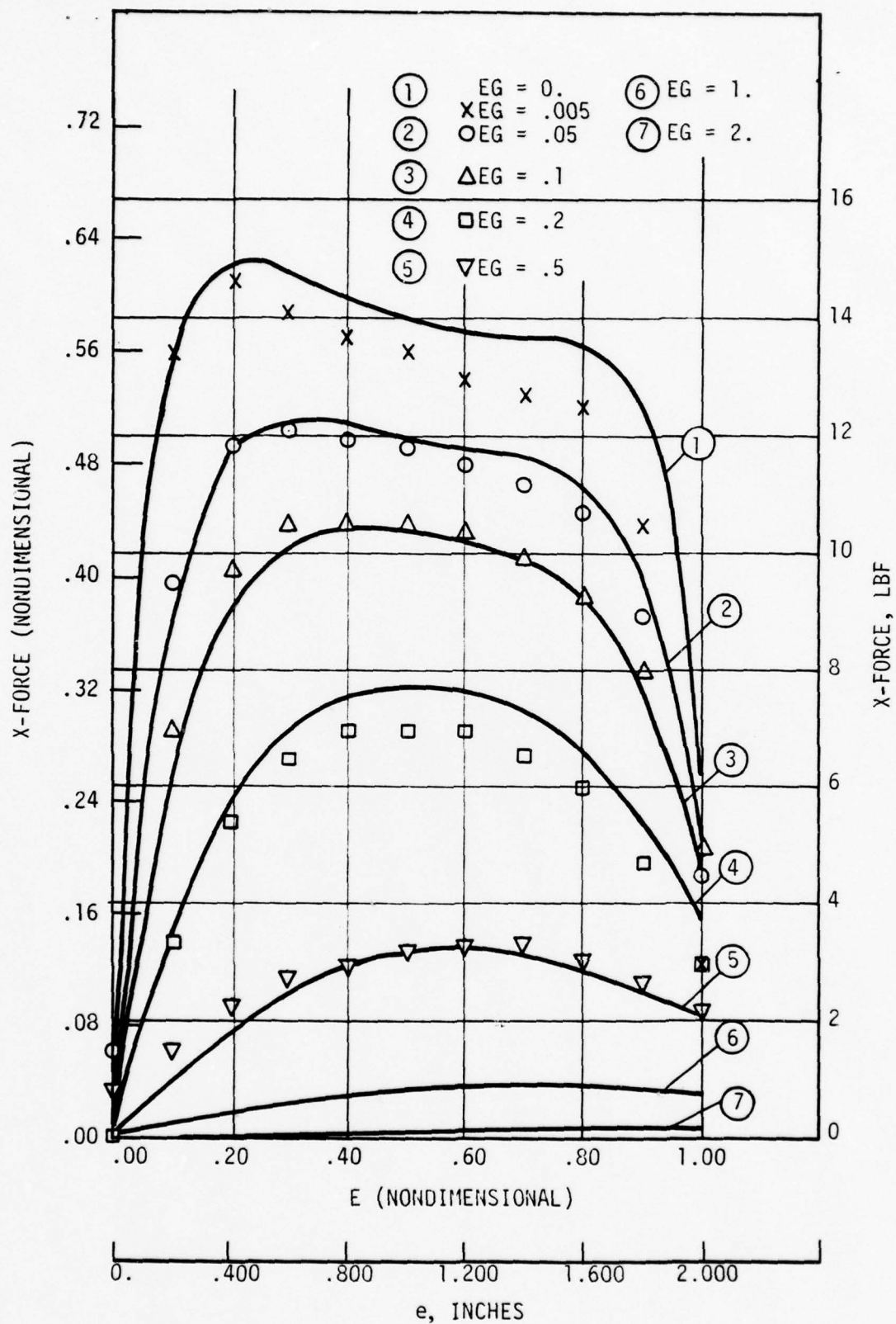


Fig. 5-10 X-Force Versus Displacement (T = 1.0625, L = 0.2469)

79P17

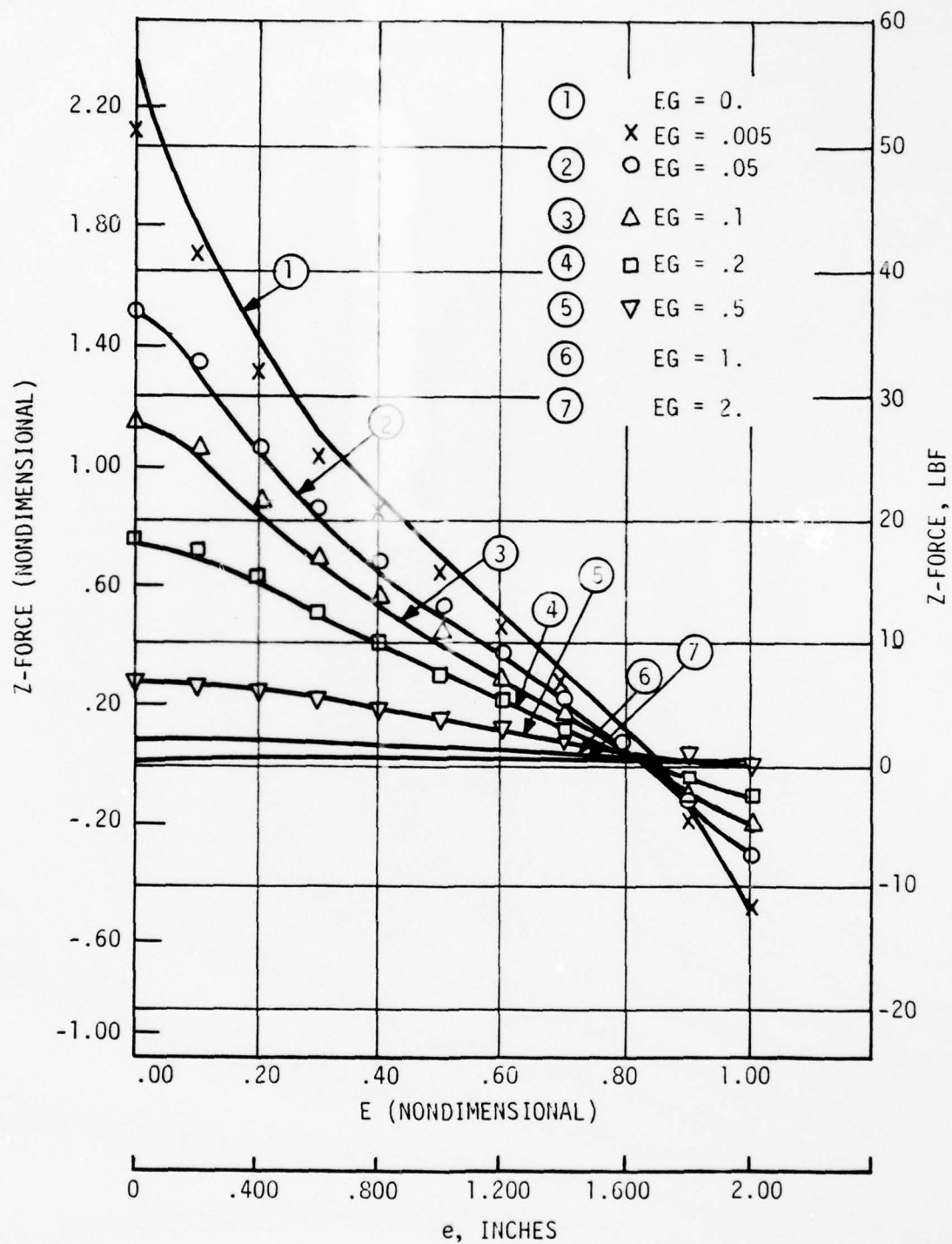


Fig. 5-11 Z-Force Versus Displacement ($T = 1.0625$, $L = 0.2469$)

79P17

The nondimensional Z-force is given by

$$I_z = \frac{F_z}{\frac{\mu}{4\pi} K K' W^2} \quad (5-1)$$

assuming $K = K'$,

$$I_z = \frac{F_z}{\frac{\mu}{4\pi} K^2 W^2} \quad (5-2)$$

From Figure 5-11, $I_z = 1.5162$ at $E = 0$ and $EG = .05$. Figure 5-11 also shows $F_z = 36.1$ lbf for the same values E and EG . Using these values in Equation (5-2) and for $\mu = 1.05 * 4\pi * 10^{-7} \frac{(\text{Wb}/\text{m}^2)}{(\text{A}/\text{m})}$, the equivalent surface-current densities of the magnets are given by

$$K = K' = 6.2519 * 10^5 \frac{\text{Amp.}}{\text{meter}} \quad (5-3)$$

The catalog value of the equivalent surface-current densities can be calculated by

$$\begin{aligned} K = K' &= \frac{Mr}{\mu} = \frac{Br}{\mu} \\ &= \frac{.82 \frac{\text{Wb}}{\text{m}^2}}{1.05 * 4\pi * 10^{-7} \frac{(\text{Wb}/\text{m}^2)}{(\text{A}/\text{m})}} \\ &= 6.2146 * 10^5 \frac{\text{Amp.}}{\text{meter}} \end{aligned} \quad (5-4)$$

The values of K and K' , shown in Equations (5-3) and (5-4), differ by less than 0.6 percent, and this demonstrates an excellent agreement between theory and experiments.

μ and the associated values of K and K' can also be calculated so that K and K' deduced from force measurements (as done in Equation 5-3), equal to those calculated from the catalog value of μ_r (as done in Equation 5-4). The values of μ , K and K' calculated following this procedure are given by

$$\mu = 1.04 * 4\pi * 10^{-7} \frac{(\text{Wb}/\text{m}^2)}{(\text{A}/\text{m})} \quad (5-5)$$

and

$$K = K' = 6.2744 * 10^5 \frac{\text{Amp}}{\text{meter}} \quad (5-6)$$

An excellent agreement between theory and experiments can again be seen, because the value of μ calculated in Equation (5-5) is very close to the catalog value of

$$1.05 * 4\pi * 10^{-7} * \frac{(\text{Wb/m}^2)}{(\text{A/m})}$$

Using the experimentally deduced values of K and K' given by Equations (5-3) and (5-4), the experimental results described in the previous sections are plotted (marked by data points) in Figures 5-9 through 5-11, mentioned earlier. The vertical axes on the right show the actual values of the forces.

A very good agreement between the theoretical predictions and the experimental results can be noticed in these figures. In addition to predicting the normal forces accurately, the theory is able to predict the transverse forces with great accuracy.

Thus, it can be stated that the current-density analogy for the permanent magnets used in theoretical predictions is a valid and usable approach to predict forces in open-circuit-type magnetic suspensions employing permanent magnets alone.

Based on the findings described above, it appears that, although nonuniformities in a magnet do exist, their influence on force predictions in open-circuit, permanent-magnet systems is only of secondary importance.

6.0 PERMANENT MAGNETS IN CLOSED MAGNETIC CIRCUIT

In this section, a report is made of the study performed on magnetic suspensions based upon closed magnetic circuits, energized by permanent magnets. Because of their high coercivity, rare-earth-cobalt permanent magnets were used in the experimental study.

The theory that was developed for predicting forces in closed-circuit-type magnetic suspensions has been reported earlier. This theory has been validated under both static and dynamic (vibratory) conditions, but the magnetic circuit considered was energized by electrical means only. However, in order to reduce the electrical power requirements, it may be beneficial to energize the magnetic circuits by permanent magnets alone or in combination with electrical means. The objective of the research reported here has been to compare the forces measured experimentally with theoretical predictions for closed-circuit-type magnetic suspensions energized by permanent magnets. Only plane geometry was considered in the experiments, and a slightly modified version of the test apparatus described in Sections 3.0 and 5.0 was used in the present study.

6.1 Magnetic Circuit

The magnetic circuit studied was essentially the same as that described in Reference 4 and referred to in Section 3.0 of this report. The coils used for energizing the magnetic circuit were removed and instead, permanent magnets were installed in series with the magnetic circuit as shown in Figure 6-1. The reluctance of the permanent magnets, therefore, plays an important role in determining the circuit performance. Provision was made for installing up to four magnets of approximately 0.5-inch thickness each. The tolerance on the thickness of the magnets was 0.0001 inch and the surface finish was better than 16 microinches; these features enabled the magnets to be installed in the magnetic circuit with a reasonably tight fit, ensuring no air gap between the magnets and the pole pieces.

The core piece with machined teeth used in earlier experiments (.020 inch thick and .060 inch pitch) was modified for the present study so that the legs of the core piece could be used as pole pieces for the present work.

6.0 PERMANENT MAGNETS IN CLOSED MAGNETIC CIRCUIT

In this section, a report is made of the study performed on magnetic suspensions based upon closed magnetic circuits, energized by permanent magnets. Because of their high coercivity, rare-earth-cobalt permanent magnets were used in the experimental study.

The theory that was developed for predicting forces in closed-circuit-type magnetic suspensions has been reported earlier. This theory has been validated under both static and dynamic (vibratory) conditions, but the magnetic circuit considered was energized by electrical means only. However, in order to reduce the electrical power requirements, it may be beneficial to energize the magnetic circuits by permanent magnets alone or in combination with electrical means. The objective of the research reported here has been to compare the forces measured experimentally with theoretical predictions for closed-circuit-type magnetic suspensions energized by permanent magnets. Only plane geometry was considered in the experiments, and a slightly modified version of the test apparatus described in Sections 3.0 and 5.0 was used in the present study.

6.1 Magnetic Circuit

The magnetic circuit studied was essentially the same as that described in Reference 4 and referred to in Section 3.0 of this report. The coils used for energizing the magnetic circuit were removed and instead, permanent magnets were installed in series with the magnetic circuit as shown in Figure 6-1. The reluctance of the permanent magnets, therefore, plays an important role in determining the circuit performance. Provision was made for installing up to four magnets of approximately 0.5-inch thickness each. The tolerance on the thickness of the magnets was 0.0001 inch and the surface finish was better than 16 microinches; these features enabled the magnets to be installed in the magnetic circuit with a reasonably tight fit, ensuring no air gap between the magnets and the pole pieces.

The core piece with machined teeth used in earlier experiments (.020 inch thick and .060 inch pitch) was modified for the present study so that the legs of the core piece could be used as pole pieces for the present work.

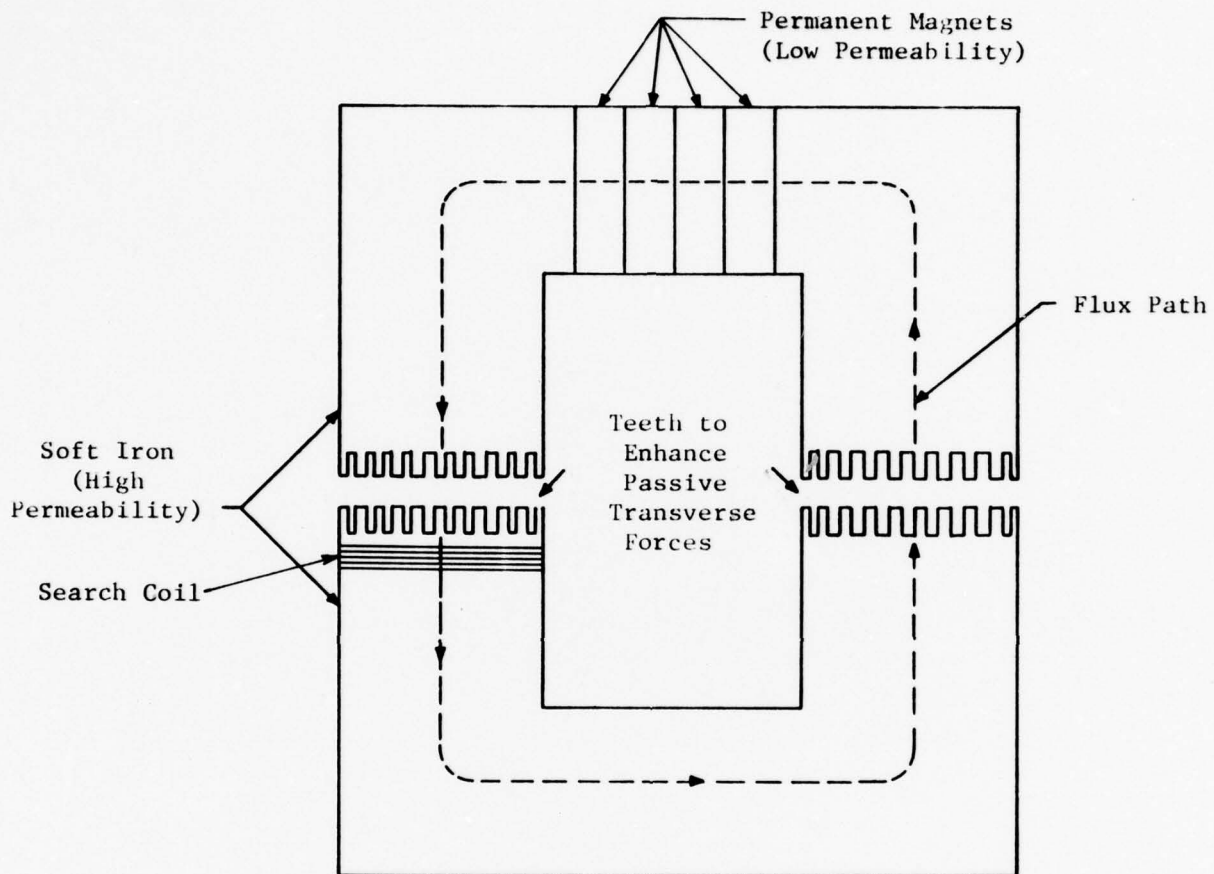


Fig. 6-1 Magnetic Circuit with Permanent Magnets and High-Permeability Pole Pieces

79P17

During the modification, it was necessary to maintain the alignment of the teeth on the two legs of the core piece. In order to accomplish this, aluminum plates were fixed to the core piece on either side by means of dowel pins and screws, before machining away the material of the core piece.

Figure 6-2 shows a photograph of the modified core piece with a permanent magnet installed. The three pieces seen adjacent to the magnet in Figure 6-2 are high-permeability iron pole pieces. These are used whenever different levels of magnetization have to be realized. The aluminum plates and dowel pins on the sides of the core piece can be clearly seen in this figure.

6.2 Experimental Apparatus and Procedure

6.2.1 Materials

The permanent magnets used to energize the magnetic circuit in this work were the same as those used for repulsion experiments. The properties of this rare-earth-cobalt material have already been listed in Table 5-1 of Section 5.0. The material of the pole piece was made of high-permeability iron and in fact, the pole pieces are the modified versions of the core pieces used for the study described in Section 3.0 and also for earlier work reported in Reference 4. As described in Reference 4, the teeth were .020 inch wide and separated by a gap of .040 inch and were cut to precision by electrical discharge machining.

6.2.2 Test Rig

The same test rig as described in Sections 2.0 and 4.0 was used for the present work. The modified core piece with the permanent magnet, shown in Figure 6-2, was fixed to the top plate, and the lower core piece (that has been used previously) with matching teeth was mounted on the bottom plate as shown in Figure 6-3. The energizing coils, shown mounted on the lower core piece, were not used in the permanent-magnet experiments described in this work. The gap and the transverse displacement were varied by moving the top and bottom plates respectively and were monitored by dial indicators and also by DC-LVDT'S.

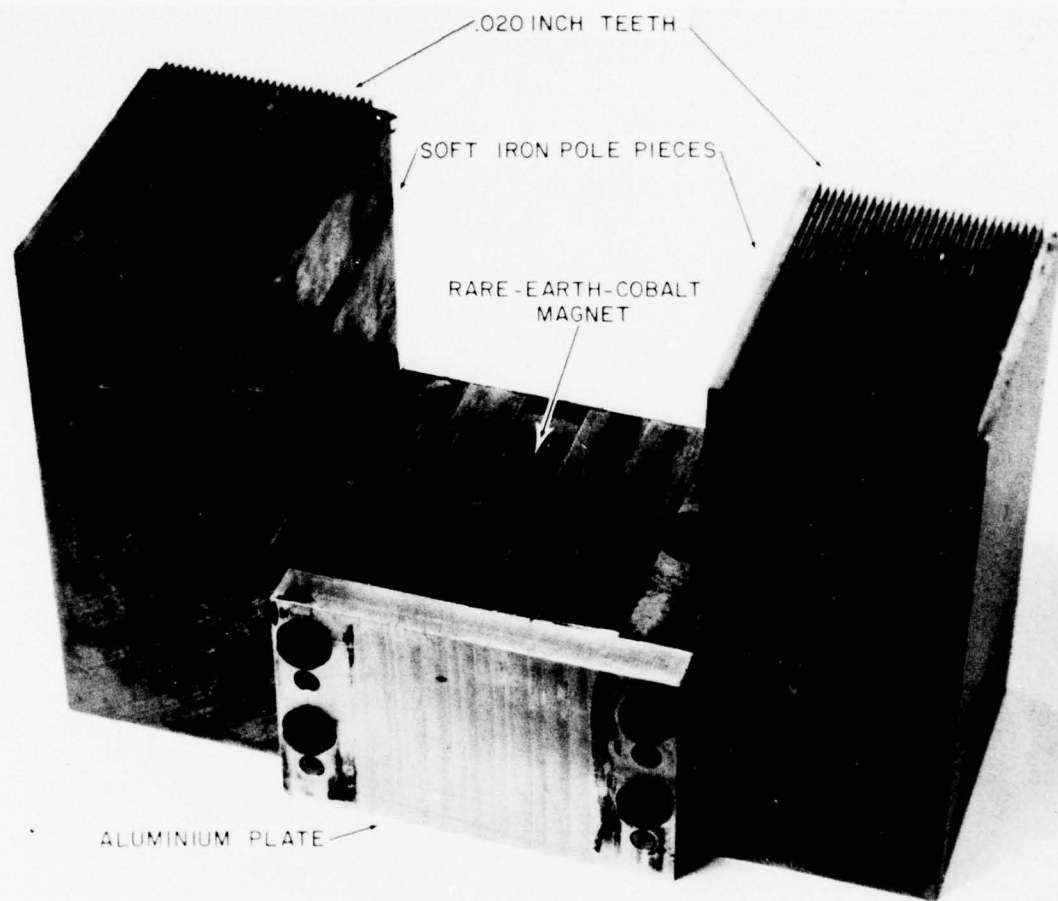


Fig. 6-2 Core Piece with Permanent Magnet Installed

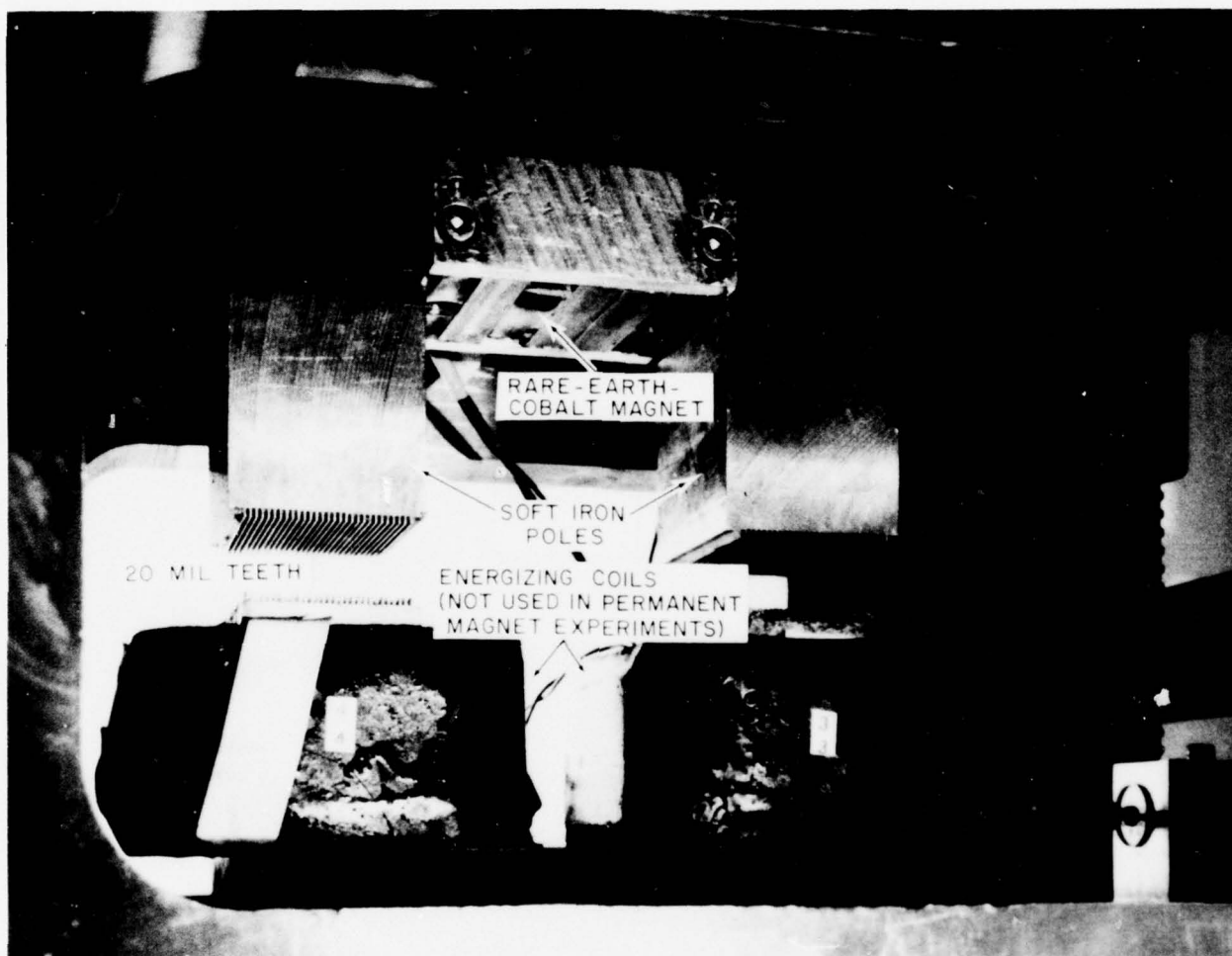


Fig. 6-3 Magnetic Cores Used with Permanent Magnets in Closed-Circuit Suspension Experiments

The alignment of the core pieces was very critical in these tests because of the very small width of the teeth. Also, extreme care was taken to obtain the same air gap at both the legs of the core pieces. Since the transverse displacement was limited to 0.030 inch (one-half the pitch of the teeth), the motion was obtained by directly manually moving the bottom plate mounted on ball bushings with the help of a screw rod. A view of the test rig with the core pieces mounted is shown in Figure 6-4.

6.2.3 Force Measurement

The previously used, multi-directional quartz piezoelectric force transducers were used in the present study. The outputs of the force transducers were connected to two charge amplifiers through summing junctions. The outputs of the charge amplifiers yielded directly the normal and the transverse forces.

6.2.4 Flux Measurement

Flux measurement was performed by using a 10-turn search coil, mounted around the teeth of the lower core piece as shown in Figure 6-1. The search coil was designed to be removable from the magnetic circuit for the measurement of the absolute value of the flux. Care was taken to wind the search coil closely around the teeth to avoid any possible linking of the leakage fluxes with the search coil.

The output of the search coil was connected to an integrating-type fluxmeter (LDJ Electronics Model 101). The fluxmeter output directly gave the number of lines of flux linking the 10 turns of the search coil. For purposes of obtaining plots, the fluxmeter output was directly connected to an X-Y plotter.

In order to measure the flux at any required gap, the search coil is mounted around the magnet, and the two magnets are brought together until separated by the required air gap. The fluxmeter is reset to zero, and the flux-versus-gap curve is plotted as the two magnets are withdrawn from each other. To measure the absolute value of the flux, it is necessary to take the search coil away from the magnet to a distant point.

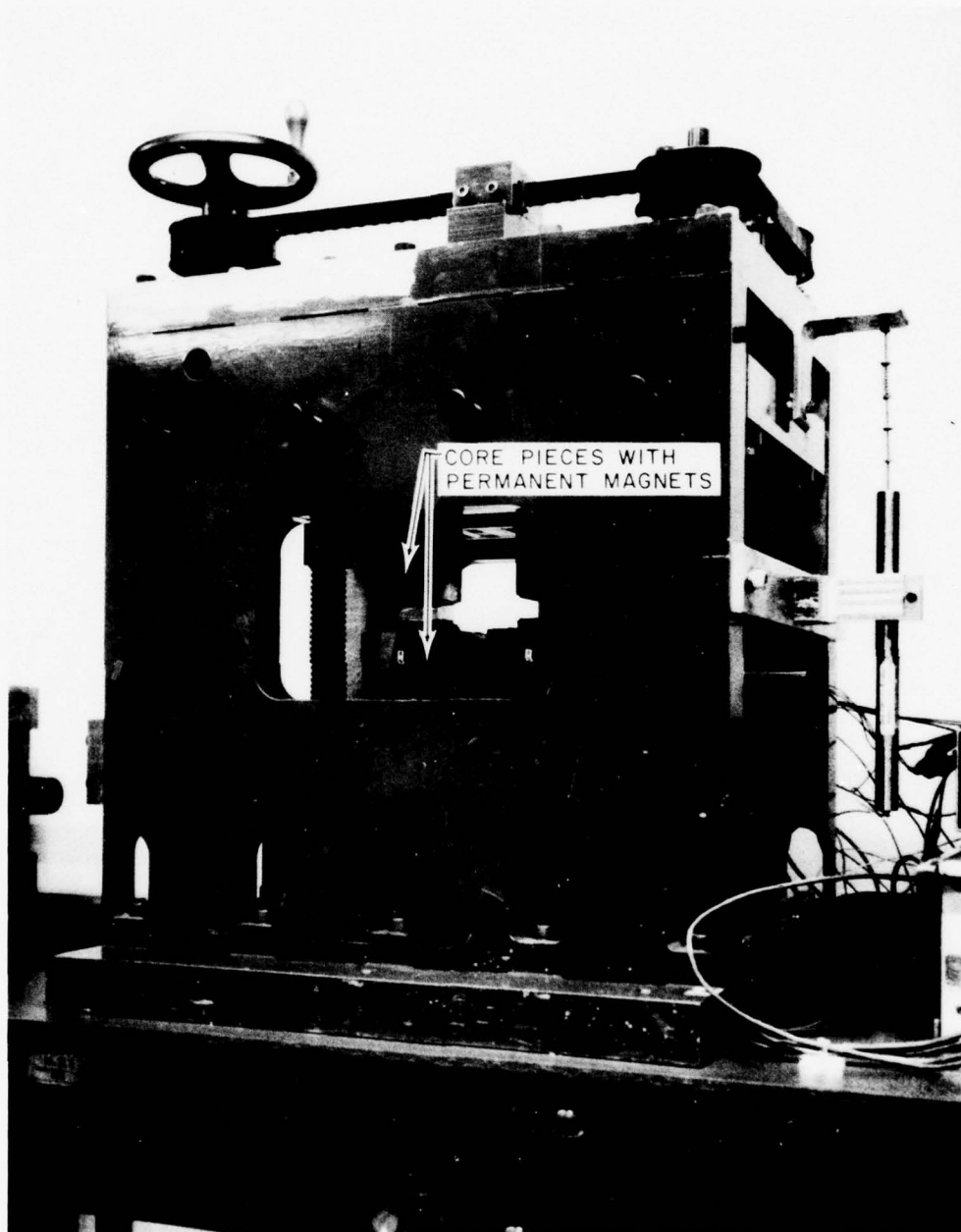


Fig. 6-4 Test Rig with Core Pieces Installed

6.2.5 Experimental Procedure

With the permanent magnets in the magnetic circuit, the degaussing of the high-permeability material present in the circuit is not possible. In order to obtain repeatable values of fluxes and forces, the material of the core pieces was cycled through the flux changes before each experiment by bringing the upper core piece in close proximity of the lower core piece (gap of .005 inch) and retracting it and then repeating this procedure about ten times. The increasing and decreasing flux curves did not deviate by any substantial amount after the above procedure was followed.

6.3 Results and Discussion

The experimental results will be presented in two sections, each section for a different magnetization level. A comparison of the experimental results with theoretical predictions is made in a separate section.

6.3.1 One Magnet in the Circuit

This section presents measurements of flux and forces as functions of gap or displacement when only one magnet (2 in. * 2-1/8 in. * .4937 in.) is used to energize the circuit.

6.3.1.1 Flux Versus Gap. Figure 6-5 shows a plot of flux versus gap. The flux was measured with search coil in the position shown in Figure 6-1. Both increasing and decreasing flux curves were recorded. The deviation obtained between the two curves was considered negligible for the present work. The absolute value of the flux was obtained by moving the search coil from the magnetic circuit to a distant point. The flux reduces with increasing gap, but it appears that the decrease in flux is more gradual than found in earlier measurements when the circuit was energized electrically.

6.3.1.2 Z-Force Versus Gap. The variation of Z-Force (attractive) versus gap is shown in Figure 6-6. The minimum gap reached was .005 inch. Fairly high normal forces are experienced at small values of gap. Here again, negligible deviation was noticed between force-gap curves for increasing and decreasing values of flux.

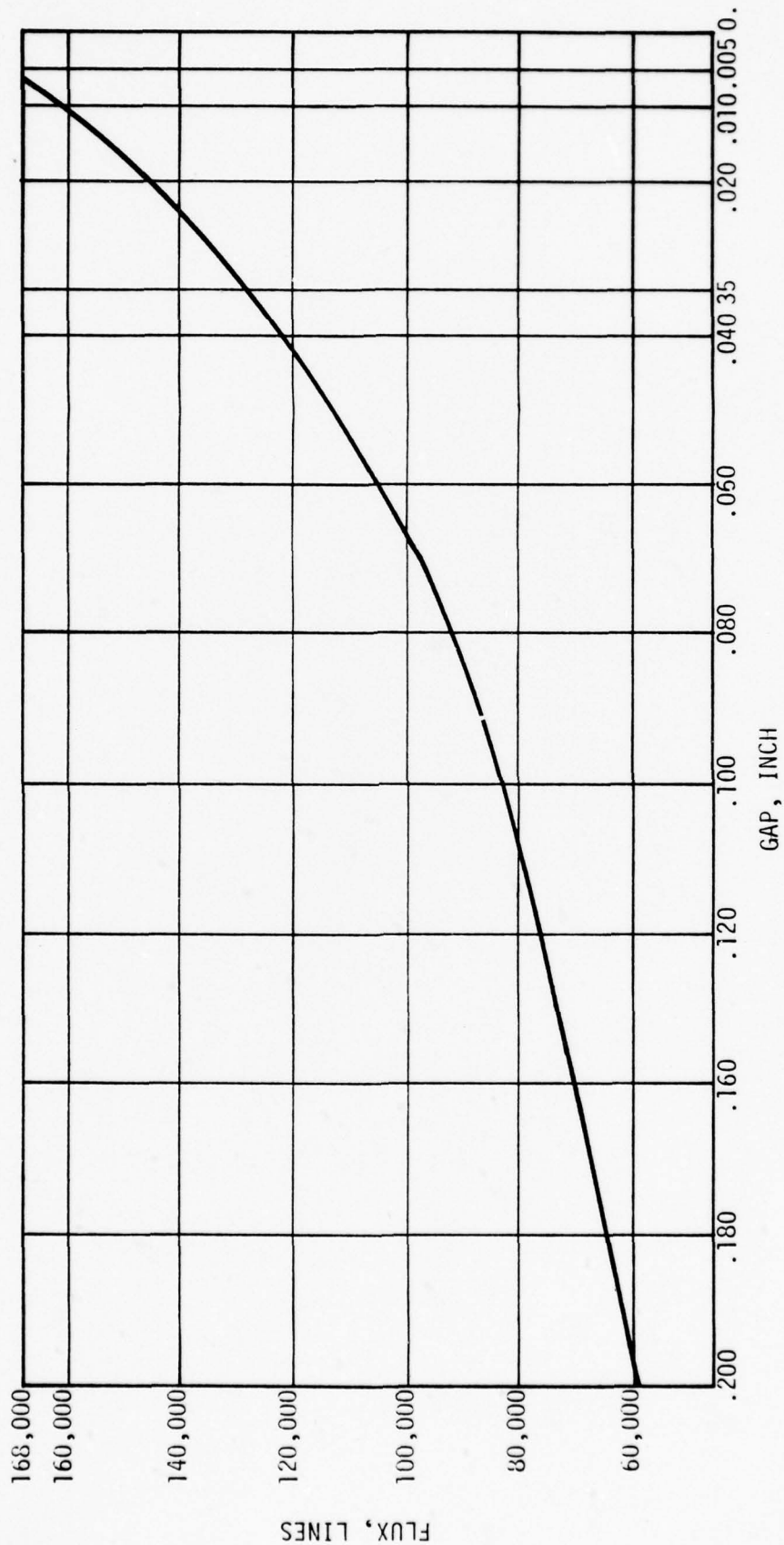


Fig. 6-5 Flux Versus Gap - One Magnet

79P17

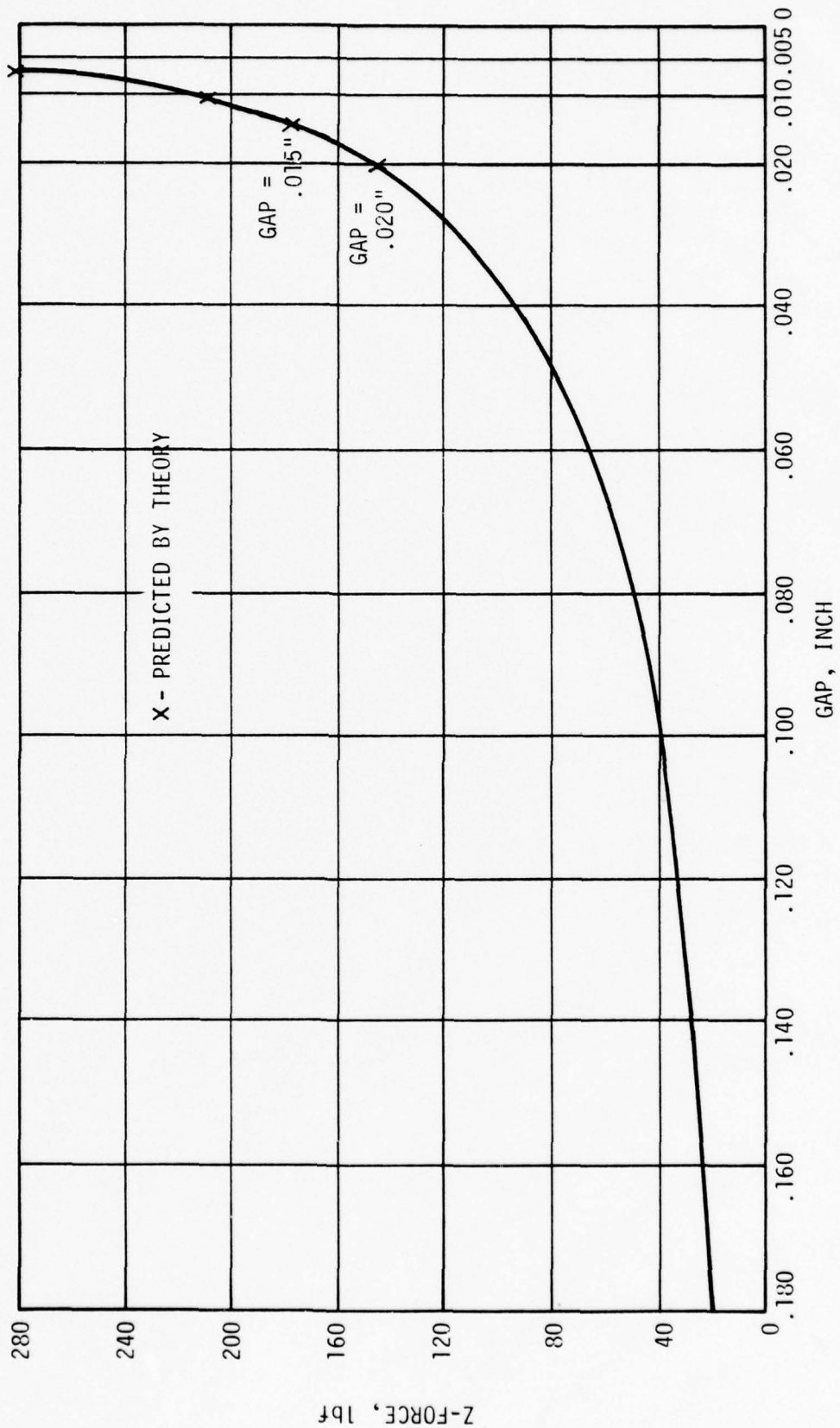


Fig. 6-6 Z-Force Versus Gap - One Magnet

6.3.1.3 Flux Versus Displacement. The flux linkages through the magnetic circuit vary with transverse displacement because of the change in magnetic circuit reluctance with displacement.

Figure 6-7 shows the changes in flux linkages at gaps of .005 inch and .010 inch as the core pieces are displaced from the aligned position. The drop in flux linkages at large displacements appears to reduce significantly with increase in gap. Although measurement of normal forces was not made in the misaligned position, one can expect a similar drop in normal forces at large displacements.

6.3.1.4 X-Force Versus Displacement. The transverse forces, which are stabilizing in nature, are plotted versus transverse displacement for various values of gap ranging from .005 inch to .060 inch in Figure 6-8. The total transverse displacement traversed was .030 inch, corresponding to one-half the pitch of the teeth. The zero displacement in Figure 6-8 corresponds to a perfectly aligned position of the teeth.

As the core pieces are transversely displaced, the X-Force increases indicating stability in the transverse direction, the X-Force reaches a maximum and then decreases with further increase in displacement. The maximum positive stiffness occurs at zero displacement. The transverse forces reduce in magnitude at increased gaps. It can, however, be noted that the flux linkages also decrease at increasing values of gap. A comparison between these experimental results and theoretical predictions will be made in a later section.

6.3.2 Two Magnets in the Circuit

This section contains results for the case when two magnets of the same size as used before (and magnetized in the same direction) are used to energize the circuit. Figures 6-9, 6-10, and 6-11 show curves of flux versus gap, Z-Force versus gap, and X-Forces versus displacement for the higher level of magnetization realized through two magnets energizing the circuit; these curves are very similar to those shown in Figures 6-5, 6-6, and 6-8.

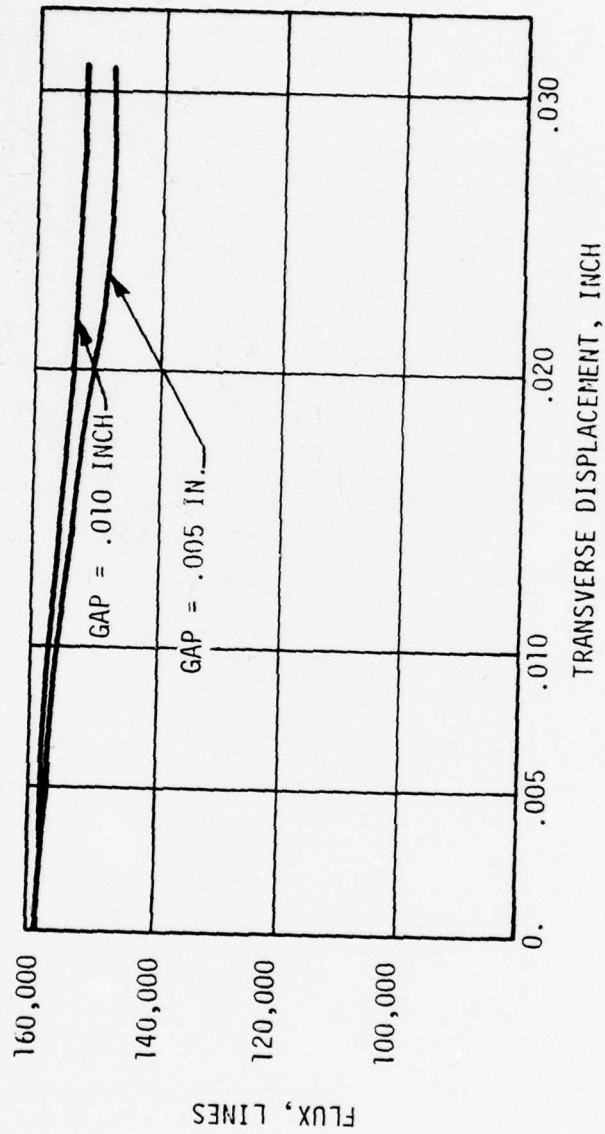


Fig. 6-7 Flux Versus Displacement

79P17

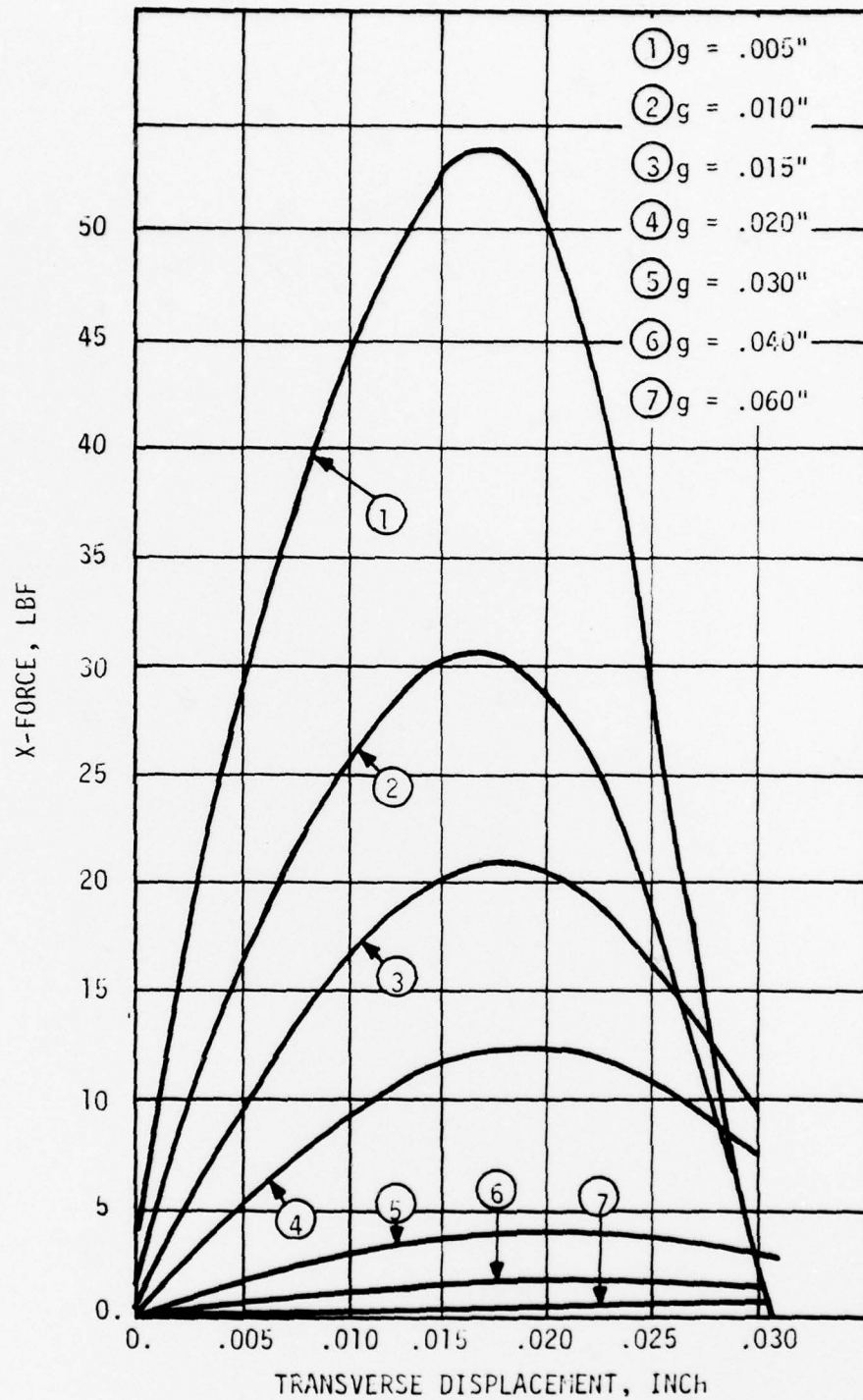
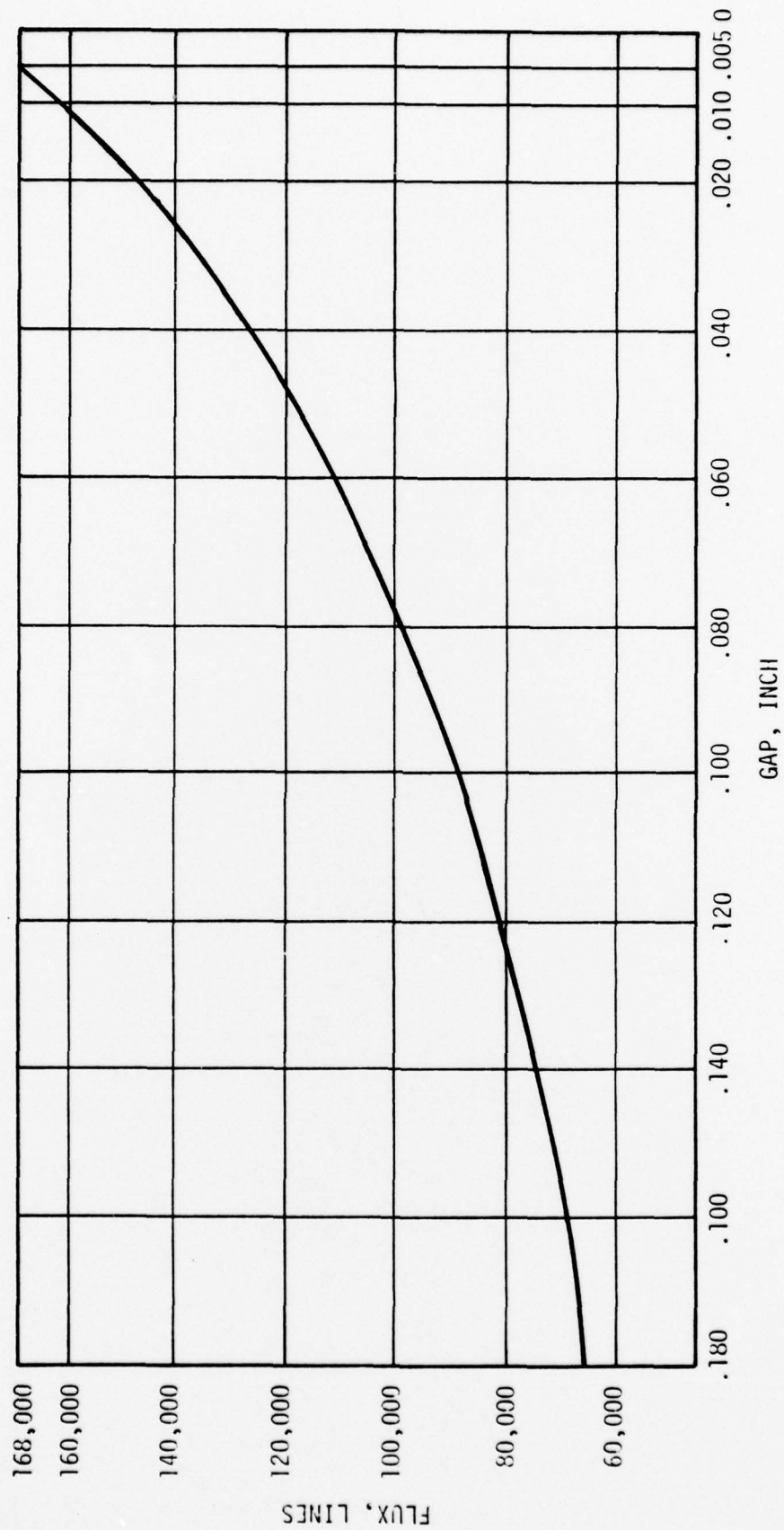


Fig. 6-8 X-Force Versus Displacement - One Magnet

79P17



79P17

Fig. 6-9 Flux Versus Gap - Two Magnets



79P17

Fig. 6-10 Z-Force Versus Gap - Two Magnets

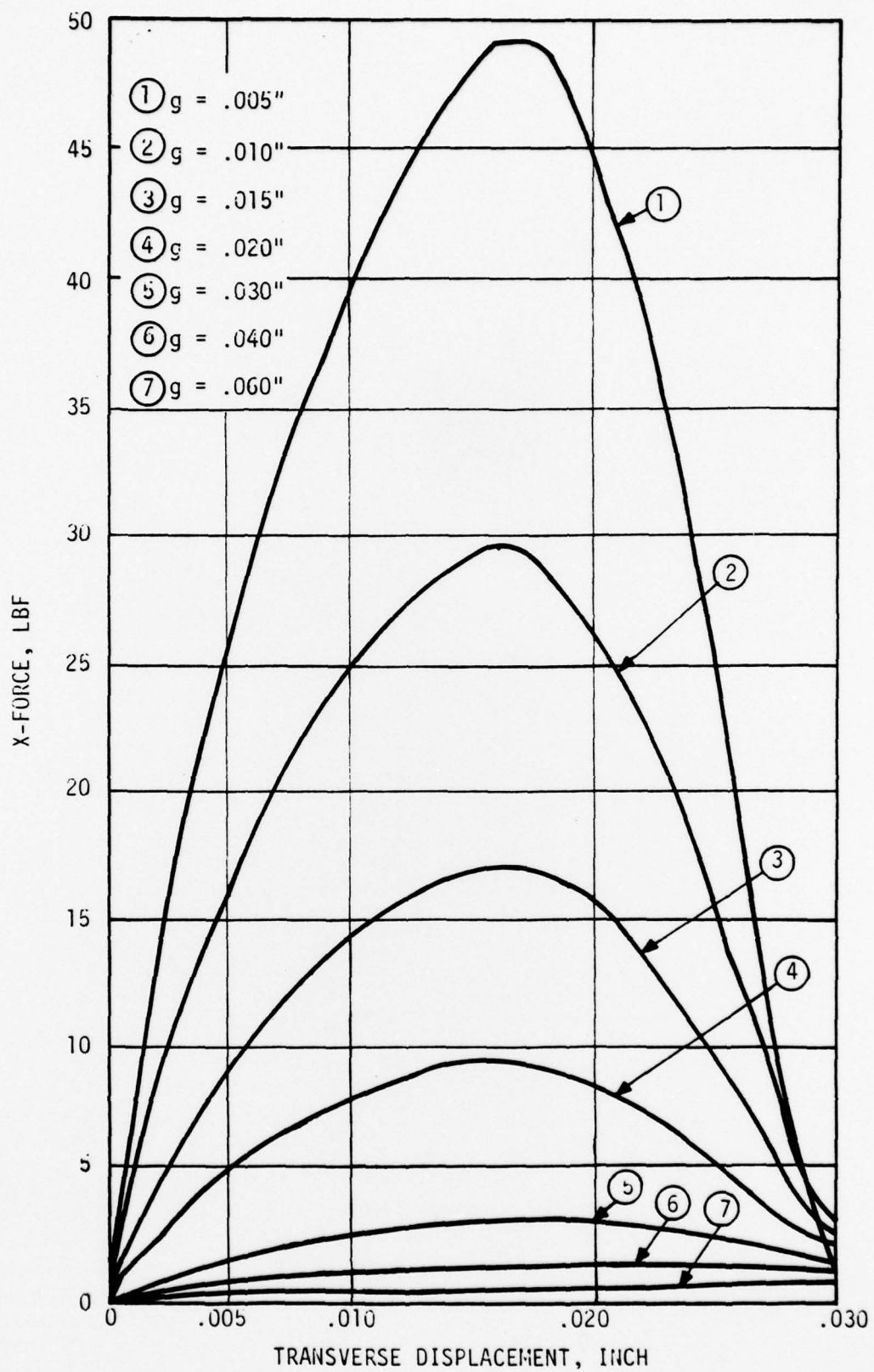


Fig. 6-11 X-Force Versus Displacement - Two Magnets

79P17

The values of fluxes and forces for the two-magnets case do not appear to differ much from the corresponding values for the one-magnet case. At a measured flux level of 168,000 lines for the one-magnet case, the actual flux density in the teeth (considering the cross-sectional area of the teeth only) is 1.84 Wb/m^2 . The material of the pole pieces in the neighborhood of the teeth is, therefore, very nearly saturated. Under these circumstances, an addition of one more magnet to double the ampere-turns in the circuit does not bring about any noticeable change in the flux level. Since the flux level does not change for the two-magnets case, both the normal and the transverse forces remain approximately the same.

6.3.3 Comparison with Theoretical Predictions

The results reported above will be compared with the analytical prediction of forces described in Section 2.0.

6.3.3.1 Force Calculation and Comparison. Table 6-1 shows the values of calculated normal and transverse forces corresponding to the experimental results described in Section 3.1. The flux variation with respect to gap was known from experimental results described in Section 3.1.1. Knowing the flux, the normal and transverse forces were calculated using the theoretical results described in Section 2.0. The numerical values of various quantities calculated are shown in Table 6-1. The change in air-gap permeance and the corresponding change in mmf with lateral displacement of the teeth have been considered. Also, for cases when the flux changes were measured with lateral displacement, the corresponding changes in mmf have been taken into account. Gaps larger than .020 inch ($\frac{t}{h} = 1.0$) have not been reported in Table 6-1 because of the small values of transverse forces and the limitations placed by the theory ($\frac{t}{h} > .5$).

The above theoretical calculations are compared with experimental results in Figures 6-6 and 6-12 through 6-15. An excellent agreement between theoretical predictions and experimental results can be seen in Figure 6-6, which shows the variation of normal force with gap.

TABLE 6-1

NORMAL AND TRANSVERSE FORCE CALCULATION

h Inch	$\frac{h}{s}$	e Inch	$\frac{t-e}{h}$	$\frac{e}{h}$	ϕ Lines	ϕ Non-Dimen.	ΔF Amp. Turns	\bar{F} Non-Dimen.	F Lbf	\bar{F}_t Non-Dimen.	F _t Lbf
.005	.125	0.	4.0	0.	168,000	3.030	124.08	4.6335	282.14	0.	0.
		.005	3.0	1.0	166,000	2.910	127.66			.420	27.07
		.010	2.0	2.0	164,700	2.655	138.83			.575	43.83
.010	.25	0.	2.0		160,000	1.778	201.38	2.6327	211.14	0.	0.
		.005	1.5	0.5	159,300	1.725	206.66			.193	16.52
		.010	1.0	1.0	158,200	1.694	208.99			.317	27.75
		.015	0.5	1.5	156,800	1.622	216.33			.373	34.99
		.020	0.	2.0	155,400	1.523	228.34			.380	39.72
.015	.375	0.	1.33	0.	153,000	1.3045	262.47	1.9416	176.34	0.	0.
		.005	1.00	0.33	153,000	1.2945	264.50			.105	9.69
		.010	0.67	0.67	153,000	1.2715	269.28			.184	17.59
		.015	0.33	1.0	153,000	1.2375	276.68			.235	23.71
		.020	0.	1.33	153,000	1.2005	285.21			.247	26.48
		.025	-0.33	1.67	153,000	1.1645	294.03			.232	26.44
		.030	-0.67	2.0	153,000	1.1295	303.14			.205	24.84
.020	.5	0.	1.00	0.	144,500	1.020	307.39	1.5900	148.55	0.	0.
		.005	0.75	0.25	144,500	1.015	308.90			.057	5.38
		.010	0.5	0.50	144,500	1.005	311.98			.102	9.82
		.015	0.25	0.75	144,500	0.990	316.70			.130	12.90
		.020	0.	1.0	144,500	0.974	321.91			.140	14.34
		.025	-0.25	1.25	144,500	0.956	327.97			.134	14.25
		.030	-0.50	1.5	144,500	0.940	333.55			.112	12.32

NOTE: Teeth geometry assumed: $t = .020''$, $s = .040''$, $l = 2.5''$ with 28 teeth in each limb.

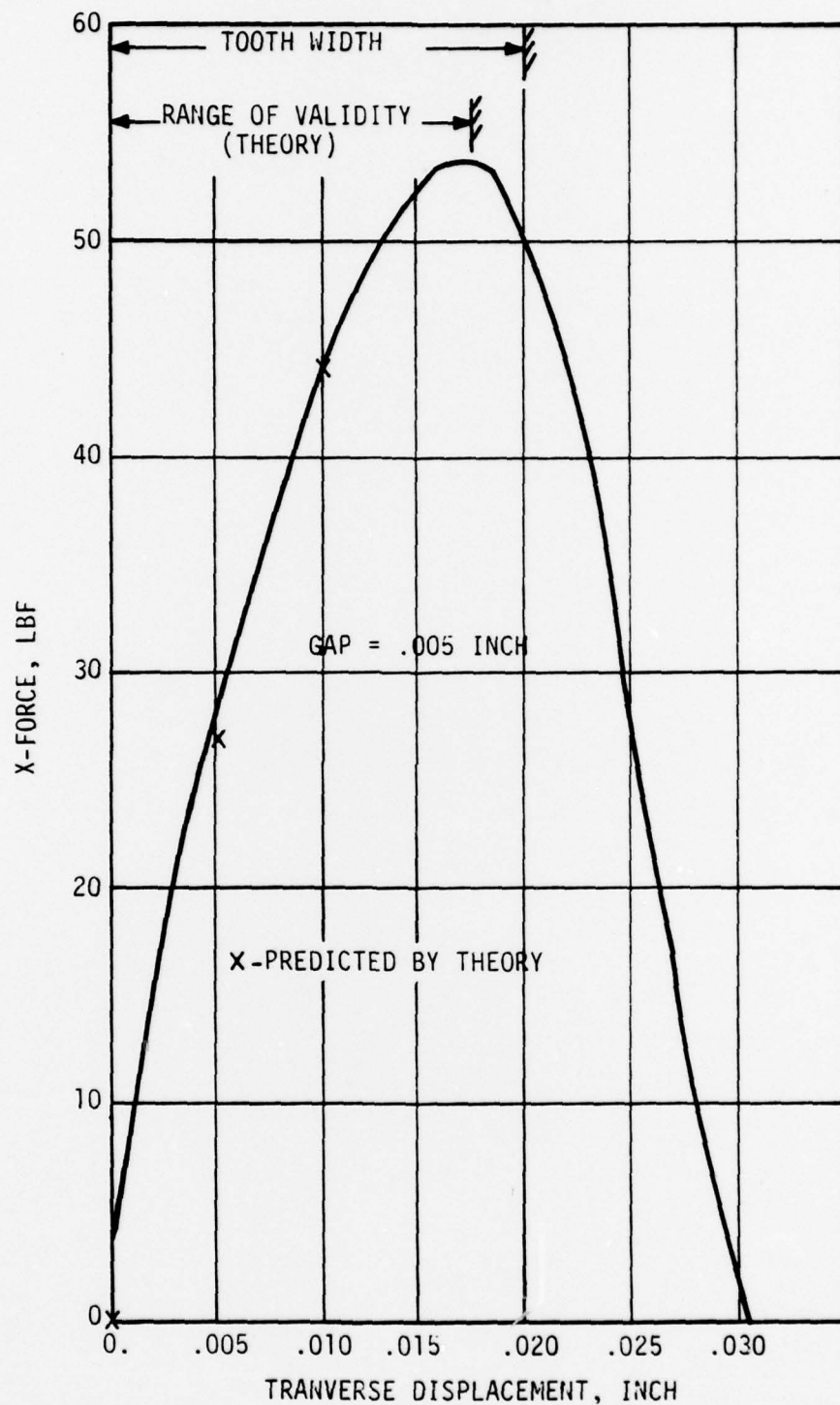


Fig. 6-12 X-Force Versus Displacement - Comparison with Theory (Gap = .005 Inch)

79P17

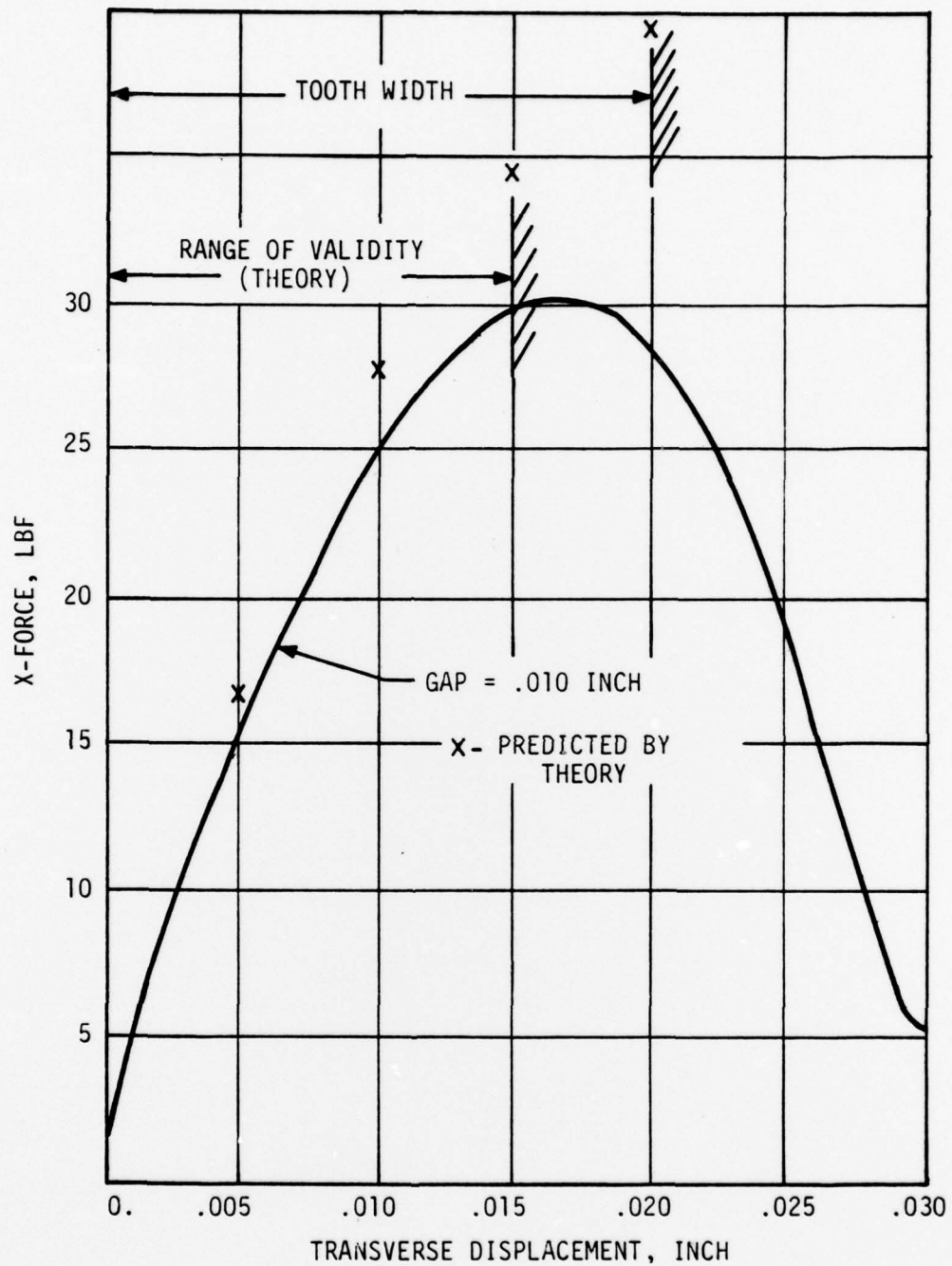


Fig. 6-13 X-Force Versus Displacement - Comparison with Theory (Gap = .010 Inch)

79P17

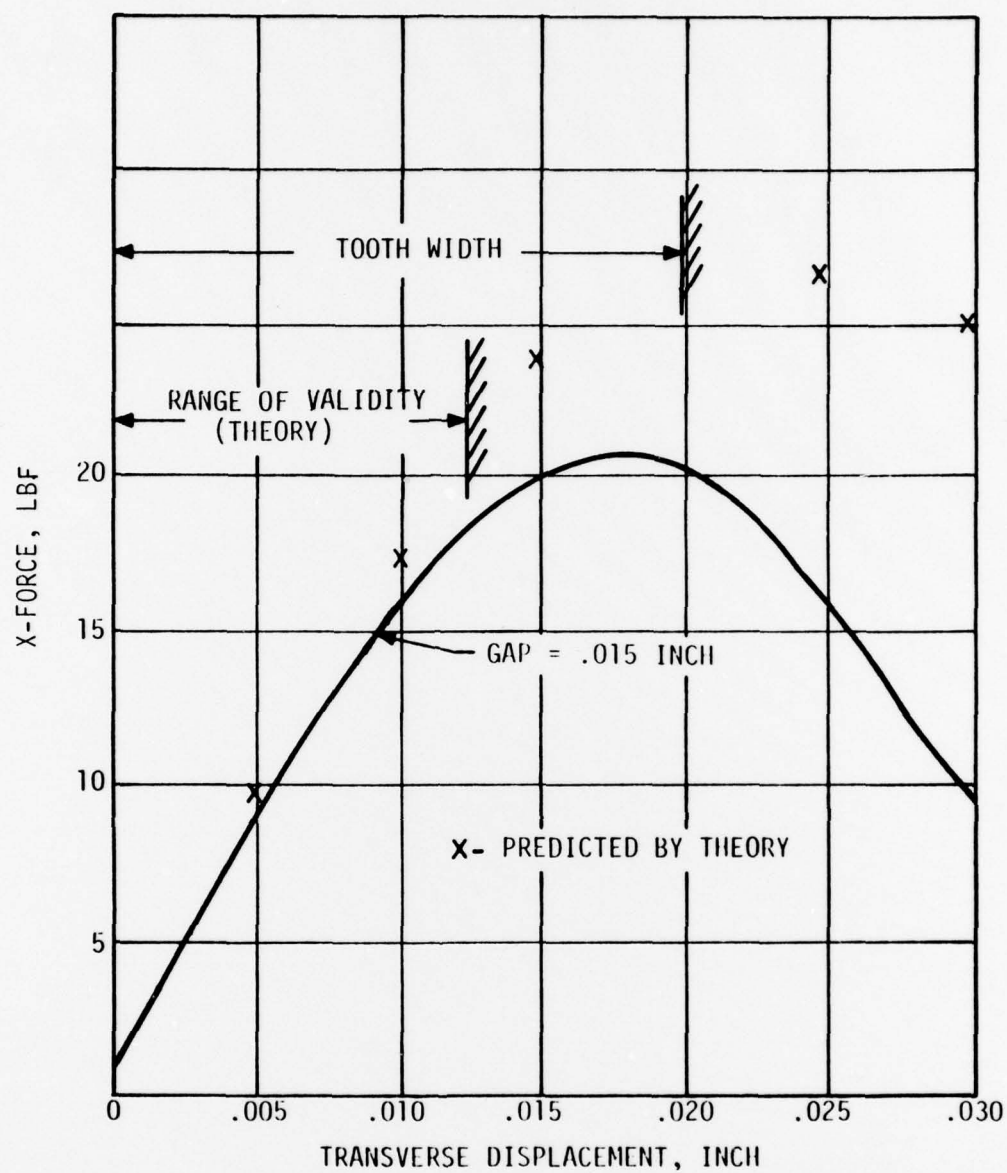


Fig. 6-14 X-Force Versus Displacement - Comparison with Theory (Gap = .015 Inch)

79P17

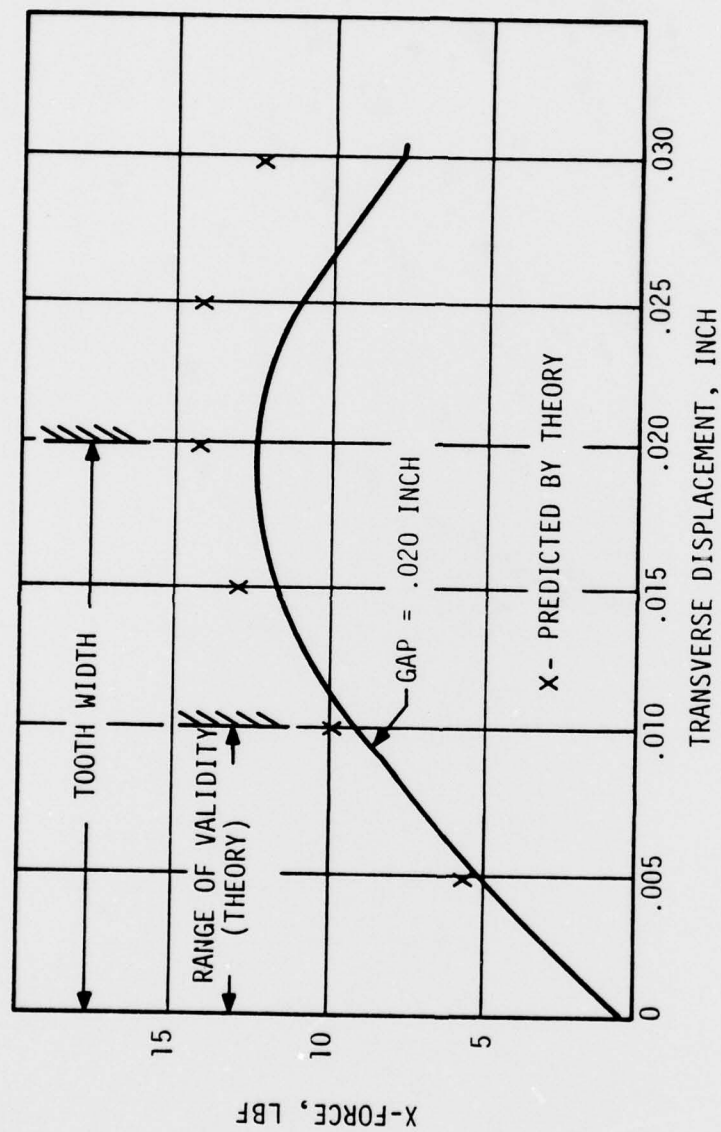


Fig. 6-15 X-Force Versus Displacement - Comparison with Theory
(Gap = .020 Inch)

79P17

Figures 6-12 through 6-15 show measured values of transverse force at various values of gap versus transverse displacement compared with theoretical predictions (marked X). The range of expected validity of the theory ($\frac{t-e}{h} > .5$) has been clearly marked in these figures. Excellent agreement between theory and experiments can be seen in the above figure within the range of validity shown. At large values of transverse displacement, the theory deviates from experiments significantly. Keeping in mind the assumption of uniform flux under the teeth made in the theory, this deviation is not surprising. Also, since in practical bearings the lateral displacements are small, the above fact does not severely limit the applicability of the theory.

6.3.3.2 Flux Calculation. In the previous section, forces were calculated based on measured values of flux, and good agreement between experiments and theory for predicting forces was witnessed.

Attempts were made using elementary analogies for the magnetic circuit to predict flux as a function of gap. The simple computations of the reluctances of the material of the pole pieces, the air gap, and the magnet (as a function of the gap and the flux level) were inadequate in predicting the flux-gap characteristics. It was concluded that, without accounting for the leakage fluxes, accurate prediction of flux-gap characteristics is not possible. However, leakage fluxes can be computed using existing, sophisticated finite-difference schemes. It was not the intent of the present research to include such a computation.

7.0 CONCLUSIONS

Subsequent to the magnetic bearing research described in an earlier report [4], several aspects of both closed and open magnetic circuits were studied, and these have been reported here.

The theory that was developed for predicting forces in closed-circuit-type magnetic suspension and reported earlier [4] had been validated under static conditions only. Dynamic measurements of forces and fluxes were made for the same magnetic circuit to determine any effects of transverse vibration. Although the measurements discovered some degradation of transverse forces with frequency, the phase angle measured between the force and the displacement indicated very little damping in the system. Based on these findings, it appears that any damping required in such magnetic suspensions may have to be provided by external means only.

Towards the study of open-circuit-type magnetic suspensions, a theory was developed for predicting repulsive forces (normal and transverse) between permanent magnets. This theory was based on the mathematical modeling of permanent magnets by their equivalent current densities. The repulsive force between two rectangular parallelepiped-shaped magnets were also measured. An excellent agreement was found between measured forces and theoretical predictions.

Furthermore, the theory that was developed for the analysis of closed-circuit suspensions referred to earlier was verified experimentally for the case when permanent magnets were used as a battery to energize the magnetic circuit.

Based on the research performed thus far, validated theories for predicting forces at the magnetic interface for both open- and closed-circuit systems appear to be at hand. However, the validation has been performed only for plane geometry. It is therefore necessary to validate the above theories for a rotating system with circular teeth.

8.0 REFERENCES

1. Smythe, W. R., "Static and Dynamic Electricity", McGraw-Hill, New York, 1950.
2. Cambridge Thermionic Corporation, "A Survey of Magnetic Bearings", Cambridge, Mass., 1972.
3. Bearns, J. W., "Magnetic Bearings", S.A.E. Automotive Engineering Congress, Detroit, Michigan, paper 810A, January 13-17, 1964.
4. Albrecht, P., and Walowit, J. A., "A Theoretical and Experimental Investigation of the Magnetic Fields and Forces Arising in Magnetic Suspension Systems", Mechanical Technology Incorporated, Report No. 75TR21, Jan. 1975.
5. Polgreen, G. R., "New Applications of Modern Magnets", McDonald, London, 1966.
6. Tsui, James B. Y., et. al., "The Effect of Intrinsic Magnetic Properties on Permanent Magnetic Repulsion", IEEE Trans. on Magnetism, Vol. MAG-8, No. 2, June 1972, pp. 188-194.
7. Senno, Harufumi, and Tawara, Yoshio, "Permanent Magnetic Properties of Sm-Ce-Co-Fe-Cu Alloys with Compositions Between 1-5 and 2-17", IEEE Trans. on Magnetism, Vol. MAG-10, No. 2, June 1974, pp. 313-317.
8. Borcherts, Robert H., "Mathematical Analysis of 'Permanent' Magnetic Suspension Systems", Journal of Applied Physics, Vol. 12, No. 4, March 15, 1971, pp. 1528-1529.
9. Cooper, Richard A., Neil, Kelvin V., and Woodruff, Wayne R., "Optimum Permanent-Magnet Dimensions for Repulsion Applications", IEEE Trans. on Magnetism, Vol. MAG-9, No. 2, June 1973, pp. 125-127.

DISTRIBUTION LIST FOR UNCLASSIFIED TECHNICAL REPORTS ISSUED UNDER

CONTRACT N00014-78-C-0098

All addresses receive one copy unless otherwise specified

Office of Naval Research (6) 800 N. Quincy Street Arlington, Virginia 22217 Attn: M. Keith Ellingsworth, Code 473	Naval Air Systems Command Department of the Navy Washington, D.C. 20360 Attn: H.J. Mueller, NAVAIR 310	Robert H. Tuffias Senior Technical Staff Litton Systems Inc. 5500 Canoga Avenue Woodland Hills, California 91364
Office of Naval Research (6) 800 N. Quincy Street Arlington, Virginia 22217 Attn: Code 102IP	Naval Air Systems Command Department of the Navy Washington, D.C. 20360 Attn: E.B. Beggs, NAVAIR 360	Paul A. Simpson Magnetic Suspension Dept. CAMBION Cambridge Thermionic Corp. 445 Concord Avenue Cambridge, Massachusetts 02138
Naval Research Laboratory Washington, D.C. 20390 Attn: G.T. Rado, Code 6450	Headquarters Naval Material Command Washington, D.C. 20360 Attn: R.V. Vittucci, NAVMAT 0333	AVCO Corp. Lowell Industrial Park Lowell, Massachusetts 01851 Attn: Paul Hoffman
U.S. Naval Postgraduate School Monterey, California 93940 Attn: Library	Defense Documentation Center (12) Building #5 Cameron Station Alexandria, Virginia 22314	Magnetic Corporation of America 67 Rogers Street Cambridge, Massachusetts 02142
Naval Ships Systems Command Washington, D.C. 20360 Attn: A.R. Paladino, NAVSHIPS 0372	Commander Defense Contract Administration Services District 96 Murphy Road Hartford, Connecticut 06114	Cornell University College of Engineering Ithaca, New York 14850 Attn: E.L. Resler, Jr.
Naval Ships Systems Command Washington, D.C. 20360 Attn: S. Leimonas, NAVSHIPS 0372	NASA Langley Research Center Langley, Virginia 23365 Attn: W. Anderson	Ernest Schliben Astro Electronics Division RCA Box 800 Princeton, New Jersey 08540
Naval Ships Engineering Center Hyattsville, Maryland 20743 Attn: Library	Richard J. Janowiecki Research Group Leader Monsanto Research Corp. 1515 Nicholas Road Dayton, Ohio 45407	The Aerospace Corporation Charles C. Launitsen Library P.O. Box 92957 Los Angeles, California 90009
Naval Ships Research and Development Center Annapolis Maryland 21402 Attn: H.V. Smith, Code A822	John E. Joyce Ferrofluidics Corp. 144 Middlesex Turnpike Burlington, Massachusetts 01803	Sperry Rand Corporation Sperry Flight Systems Division 2111 N. 19th Avenue Phoenix, Arizona 85027 Attn: Dr. R. Andeen
Naval Ships Research and Development Center Annapolis, Maryland 21402 Attn: E.R. Quandt, Code A730	General Electric Company P.O. Box 5000 Mail Drop 230 Binghamton, New York 13902 Attn: Robert Wells	General Electric R&D Center 1 River Road Niskayuna, New York 12309 Attn: Mr. J. Fox
Office of Naval Research 800 N. Quincy Street Arlington, Virginia 22217 Attn: Stan Doroff, Code 438	Naval Ordnance Systems Command Washington, D.C. 20360 Attn: J.F. Dibrell, NAVORD 034	Aerojet Electric Systems Co. 100 W. Hollyvale Street Azusa, California 91702 Attn: Mr. Thomas C. Richmond
Director (6) Naval Research Laboratory Washington, D.C. 20375 Attn: Code 2627	Headquarters Naval Material Command Washington, D.C. 20360 Attn: V.J. Argiro, NSP 24	Colorado State University Dept. of Electrical Engineering Fort Collins, Colorado 80521 Attn: T.B. Jones
U.S. Naval Academy Annapolis, Maryland 21402 Attn: Library	Office of Naval Research 495 Summer Street Boston, Massachusetts 02210	Deposits and Composites Inc. 1821 Michael Faraday Drive Reston, Virginia 22090
Naval Ships Systems Command Washington, D.C. 20360 Attn: L. Benen, NAVSHIPS 03411	NASA Goddard Space Flight Center Greenbelt, Maryland 20770 Attn: P.A. Studer	Dr. E.A. Erdelyi Dept. of Electrical Engineering University of Colorado Boulder, Colorado 80303
Naval Ships Systems Command Washington, D.C. 20360 Attn: M. Wapner, NAVSHIPS 03523	NASA Goddard Space Flight Center Greenbelt, Maryland 20770 Attn: L.J. Veillette	NASA-Lewis Research Center 21000 Brookpark Road Cleveland, Ohio 44135 Attn: Mr. William J. Anderson
Naval Ships Engineering Center Hyattsville, Maryland 20743 Attn: R. Graham, Code 6148D	Carl Henrikson Manager, Advanced Control Systems Ball Brothers Research Corp. Boulder Industrial Park Boulder, Colorado 80302	Consolidated Natural Gas Service Co. Inc. 110001 Cedar Avenue Cleveland, Ohio 44106 Attn: Mr. Paul F. Swenson
Naval Ships Research and Development Center Annapolis, Maryland 21402 Attn: A.A. Wolf, Code A120		
Naval Ships Research and Development Center Annapolis, Maryland 21402 Attn: L.J. Argiro, Code A710		